THE DYNAMICS OF ACCRETION DISKS AROUND COMPACT STARS WITH COMPLEX MAGNETIC FIELDS

By

Anno Kare

A DISSERTATION SUBMITTED IN PARTIAL FULFILLMENT OF
THE REQUIREMENTS FOR THE DEGREE OF
DOCTOR OF PHILOSOPHY IN ASTROPHYSICS
AT
ADDIS ABABA UNIVERSITY
APRIL 2014

ADDIS ABABA UNIVERSITY
DEPARTMENT OF
PHYSICS

The undersigned hereby certify that they have read and recommend to the Faculty of Graduate Studies for acceptance a thesis entitled “**The Dynamics of Accretion Disks around Compact Stars with Complex Magnetic Fields**” by **Anno Kare** in partial fulfillment of the requirements for the degree of **Doctor of Philosophy in Astrophysics**.

Dated: April 2014

External Examiner: ____________________
Prof. Włodek Kluz̄niak

Research Supervisor: ____________________
Dr. Legesse Wetro, Dr. Ulf Torkelsson

Research Supervisor: ____________________
Dr. Legesse Wetro, Dr. Ulf Torkelsson

Examing Committee: ____________________
Internal Examiner: Prof. A. V., Gholap

____
Dept. Chairman: Dr. Belayneh, M.

ADDIS ABABA UNIVERSITY

Date: **April 2014**

Author: **Anno Kare**

Title: **The Dynamics of Accretion Disks around Compact Stars with Complex Magnetic Fields**

Department: **Physics**

Degree: **Ph.D. in Astrophysics** Convocation: **August** Year: **2014**

Signature of Author

To the Lord of Lords

Table of Contents

Abstract

Strongly magnetized stellar objects have magnetospheres characterized by such activities that define the geometry of the inner edge of the disk as well as control the inflow of matter to the NS surface itself. Of all possible components of the surface magnetic field of the central object (neutron star-NS), we have only considered the quadrupole term to investigate what ever is going on nearer to the surface of the NS. There is a highly important difference of the accretion flow in a quadrupolar and dipolar magnetic fields. The dipolar magnetic field will in the end always present a barrier to the accretion flow since the field lines are perpendicular to the plane of the disk, but the quadrupolar magnetic field will in the simplest case lie in the plane of the disk, and thus it will rather channel the accretion flow all the way down to the stellar equator. This work involves a mathematical treatment of an accretion disk around a magnetized star. In order to define the disk structure magnetohydrodynamic (MHD) equations are solved in cylindrical coordinates. For the detailed results an ordinary differential equation (ODE) derived from the angular momentum equation is numerically solved. So, both Keplerian and non-Keplerian cases of thin accretion disk are solved. Further, introductory work on slim disk is included as a part of this work. The results of our analysis indicate the existence of two different regions: a super-Keplerian innermost region and a broader sub-Keplerian outer region. The effects of stellar and toroidal magnetic fields on the variations of viscosity, temperature and density have also been studied. We have identified the nature of the inner portion of an accretion disk. The velocity of the transition varies from corotating magnetospheric boundary to super-Keplerian for low density inner most portion of accretion disk, that extends from $0.5R_M$ to the peak and then to sub-Keplerian. Our results are applicable to accreting astrophysical systems such

as neutron stars (NSs) and white dwarfs (WDs). It can also explain observational results not yet fully backed with theories.

Acknowledgements

First of all I would like to thank almighty God, who foretold and accomplished everything accordingly. If God were not on my side, I could not have accomplished the work.

I would like to thank Ministry of Education, AAU and Ethiopian government for their joint effort to make true the PhD program in Ethiopia. I want to say really thank you for all services, such as dormitory at Akaki Campus, transport service, financial support to do our research, and specially sponsorship to conduct my research at Gothenburg, Sweden. I would like to extend my gratitude to AAU President's Office, Office of the Graduate Studies and Research. I would like to thank Dr. Melaku Wakuma, for his cooperation and encouragement to settle the visa facilitation and make my trip to Sweden true.

I would like to express my appreciation and Heart felt gratitude to Dr. Legesse Wetro and Dr. Ulf Torkelsson, my research advisors (supervisors) for their invaluable professional advice by giving me intellectual guidance, unreserved suggestions and constructive comments. With out their great dedication and assistance, the completion of this work has been impossible.

I would like also to thank Department of Physics, AAU for this research opportunity it has provided me. I extend my thanks to the Physics department Heads Dr. Tilahun Tesfaye, Dr. Gizaw Mengistu, Dr. Lemmi Demeyu and Dr. Belayneh Mesfin, DGC members and other staff members in facilitating academic and administrative affairs for my work. Many thanks to Mrs. Tselat, secretary of the Physics department, for kindness and cooperativeness.

My special thanks also goes to my wife Chaltu Alemayehu and my children Tigist Anno, Amanuel Anno and Bontu Anno whose eagerness to see my success and their unreserved support were engines to my educational endeavors. I also appreciate their patience & long endurance specially during my study years.

More over my thanks also goes to Wollega University for their cooperation & financial support till the end my study years. Finally, I would like to acknowledge, all the department members of physics (WU) for their cooperation throughout my study years. I would like also to express my being indebted to all my friends who assisted me directly or indirectly during my stay in PhD program.

Anno, Anno Kare
Addis Ababa University
Department of Physics
Addis Ababa, Ethiopia

General Introduction

The interaction between an accretion disk and a magnetic central object lies at the heart of the physics of a variety of astrophysical systems, including accreting neutron stars [21], magnetic white dwarfs in cataclysmic variables [6], and T Tauri stars [8]. Compact objects consist of white dwarfs (WD), neutron stars (NS) and black holes (BH). As the endpoint states of stellar evolution, they form fundamental constituents of galaxies. WDs are held up against gravitational collapse by the degeneracy pressure of the electrons [23]. Immediately following the idea formulated by Fowler, existence of a large core degenerate neutrons was predicted- the NS. NSs are rapidly spinning, extremely dense astronomical object, composed primarily of neutrons. It is created when the core of a supergiant star has evolved so that it burns heavy elements instead of hydrogenhas converted all of the material in its core to iron. Black holes (BHs) have been proposed as the ultimate energy source for quasars in 1963. The existence of black holes has been established in a huge mass range, from about three solar masses to 10 billion solar masses in the centers of huge elliptical galaxies.

Ghosh and Lamb (1979) proposed a model for disk accretion by a rotating magnetic neutron star. The magnetic field of the star is penetrating the accretion disk, and is producing an electric current in the disk, such that there is a Lorentz force on the disk resulting in a torque between the disk and the star. The part of the accretion disk that is located inside the co-rotation radius produces a torque that spins up the neutron star, while the part of the disk that is located outside the co-rotation radius produces a spin down torque on the neutron star. Consequently, the net torque on the neutron star is determined by the position of the inner edge of the accretion disk, which depends on the accretion rate, the higher the accretion rate the closer to the neutron star is the inner edge of the disk. The model is therefore making a definite prediction that the spin up torque on the neutron star is correlated with the accretion rate, and the accretion rate can be estimated from the X-ray luminosity [19].

The Ghosh and Lamb (1979) model has been confirmed to some extent through the observations of the outbursts in Be/X-ray transients. However, there are some X-ray pulsars with permanent accretion disks, whose behaviours appear to contradict the model [13]. These systems are switching between states of essentially constant spin up and constant spin down with no apparent correlation with the X-ray flux. The time scale over which the torque remains constant varies from system to system. In some systems it is as short as some tens of days, while in some other systems it can remain constant for ten years.

Several models have been advanced to explain this phenomenon. Torkelsson [29] noted that the Ghosh & Lamb model ignores the possibility of an intrinsic magnetic field in the accretion disk, but it is currently thought that the accretion disk becomes turbulent due to the magnetorotational instability [25], [26]. Numerical simulations show that the turbulence produces a dynamo effect in the accretion disk [12]. The magnetic field due to the dynamo can increase the torque between the neutron star and the accretion disk by an order of magnitude (e.g. Tessema & Torkelsson [28],[27]), and it has been inferred that the torque reversals can be interpreted as magnetic field reversals in the dynamo similar to the magnetic field reversals that we observe on the Sun.

It is believed that magnetic fields are important in accretion disks. If the angular velocity decreases outward like Keplerian disks, then the presence of a weak magnetic field leads to magneto-rotational instability. This has been shown to produce turbulence and, together with the strong radial shear, can result in self sustaining dynamo action [26]. Such dynamos can generate and maintain magnetic fields in accretion disks. The resulting turbulent viscosity and large scale magnetic stresses provide a means of angular momentum transport which can drive the inflow through the disk. Quadrupolar and dipolar symmetry magnetic fields transport angular momentum in different ways. Quadrupolar magnetic fields have horizontal components which are symmetric about the disk mid plane, and antisymmetric vertical component. Taking cylindrical coordinate centered on accretor, the B_rB_ϕ magnetic stress advects angular momentum outwards through the disk and hence plays a part in driving the inflow.

Many accreting stars have a strong magnetic field which disrupts the accretion disk and channels accreting matter to the stars surface. For such stars many spectral and photometric properties are determined by the magnetic field. On the one hand the magnetic field modifies the structure of the disk and on the other hand it produces an exchange of angular momentum between the NS and the disk, leading to observable variations in the spin rate of the NS. Examples include young solar type stars (classical T Tauri stars, hereafter CTTSs, and millisecond pulsars, white dwarfs in the binary systems (cataclysmic variables). The properties of such accretion will depend on the structure of the magnetic field of the star[15].

In early models, it was assumed that the stars intrinsic magnetic field was a pure dipole (Ghosh & Lamb 1979) [19] However, the actual configuration of the magnetic field of strongly magnetized stars may depart from the dipole one. For example, Safier (1998) presented a number of arguments pointing to a non dipolar magnetic fields in some CTTSs

[22]. The Zeeman measurements of the magnetic field of a number of CTTSs based on the photospheric lines show that the magnetic field at the surface of CTTSs is strong ($1-3$ kG) but not ordered, which means that close to the star the magnetic field is non-dipole [7]

The measurements of the magnetic fields of rapidly rotating low-mass stars with the ZeemanDoppler imaging technique have shown that in a number of stars the magnetic field has a complicated multipolar topology close to the star. If the multipolar component dominates in the disk-accreting binary systems, then the matter flow to the star and the hot spots will be different from those in the case of a pure dipole field [11].

The dipole magnetic field may, of course, dominate in some stars, and it will dominate at larger distances from stars with complex surface magnetic fields. There are observational signs that the dipole component possibly disrupts the disk. In many cases, there is evidence that the dipole field dominates at all distances, giving periodic light curves in X-ray binaries, intermediate polars, and some CTTSs. The magnetic field configuration is likely to be different in stars with varying levels of importance of the dipole component. Bouvier et al. (2006) argued that there are many signs of magnetospheric accretion in CTTSs and that the field is probably dipolar at larger distances from the star, but may have a strong multipolar component close to the star [10].

Early research on quadrupole magnetic fields near the surface of neutron stars was done by Shakura, Postnov & Prokhorov (1991) and Panchenko & Postnov (1994) [18], [9]. Recently, Jardine et al. (2006) [14] investigated the possible paths of the accreting matter in the case of a multipolar field derived from observations. Von Rekowski & Brandenburg (2006) performed axisymmetric simulations of the diskmagnetosphere interaction in case when magnetic field is generated by the dynamo processes both in the star and in the disk. They obtained a time-variable magnetic field of the star with a complicated multipolar configuration which shows that the dynamo may be responsible for a complex magnetic field structure [5]. Analytical analysis of accretion to a non-rotating star with a pure quadrupole magnetic field was done by Lipunov (1978) [30]. A combination of dipole and multipole fields was discussed by Lovelace, Romanova & Bisnovatyi-Kogan (2005) [24]. However, no numerical simulations of such accretion have been performed so far. Full three-dimensional MHD simulations of accretion to a star with a non-dipole magnetic field frozen to the stellar surface, was done by [15]

While previous studies have considered disks in a dipole field, we will consider an axisymmetric thin disk threaded by the magnetic quadrupole field of an aligned rotator, which might be the dominant magnetic field component close to the star.

In this work, we study hydrodynamical models of thin accretion disks -optically thick disks which generalize the standard models of radiatively efficient thin disks to all accretion rates. We start with theoretical background on accretion compact objects. It is followed by a general introduction to the theory of accretion onto compact objects. In the following sections we will introduce the necessary equations describing thin disk. A semi-analytical method is presented for solving for the radial and vertical structure of accretion disks within a large-scale quadrupole magnetic field. For this we will use two approaches: Keplerian for the first and non-Keplerian for the second part. Based on this we will finally discuss the obtained results and show their applications.

Chapter 1

Accretion disks and Compact objects

1.1 Introduction

Supernova is a violent explosion that occurs due to gravitation collapse. It can be brighter than all the stars in an entire galaxy combined and can shine for weeks or months. The extreme conditions in supernova explosions forge atomic particles into chemical elements heavier than iron. The explosions also spread gas and dust into space where the chemically enriched interstellar material can form new stars and planets. The spectrum of the light from supernovas is an important source of information that can be used to help classify supernova explosions. Spectral lines indicate what chemical elements are present and what temperatures occur in the explosion. Astronomers use the term Type I for supernovas that do not show spectral lines of hydrogen and Type II to describe supernovas that do. The subtypes for Type I supernovas, known as Type Ia, Type Ib, and Type Ic, lack hydrogen lines in their spectra. They result from different explosion mechanism from Type Ia - core collapse of a giant star rather than from the thermonuclear explosion of a white dwarf star. Different types of supernovas also have distinct light curves or patterns of brightness over time. Type Ia supernovas are typically brighter than other supernovas, while Type Ib and Type Ic are generally dimmer.

Stars end their lives as compact objects (COs) depending on the initial mass of the collapsed star, as neutron star (NS), white dwarf (WD) or black hole (BH). A neutron star is a type of remnant that can result from the gravitational collapse of a massive star ($M \gtrsim 8M_{\odot}$) during a Type II, Type Ib or Type Ic supernova event, which occurs when a massive star runs out of nuclear fuel in its core at the end of its life.

Neutron stars (NSs), Black holes (BHs) and White dwarfs (WDs) are associated with extreme states of matter. The diversity of the extreme phenomena related to COs such as the supernuclear density in the interior, the strong magnetic field on the surface, and the intense radiation field in the magnetosphere, strong gravity etc. make this area of research attractive. They are good laboratories that can reveal a lot of secrets about the origin and evolution of the universe.

The compact object is not necessarily close to the companion star at the time of its formation. Most of the known pulsars are isolated objects which emit radio-waves at frequencies $10^8 - 10^{10}$ Hz, which are pulsed at the rotation frequency of the star. The radio observations of pulsars stretch back to 1967 when the first pulsar was discovered. Rotation powered Pulsars (RPPs), Millisecond Pulsars (MPs) and Magnetars fall in the category of isolated pulsars.

When a CO such as a neutron star (NS) or a black hole (BH) is formed very close to its companion star in a binary system, it has a strong gravitational influence on the surface layers of the companion star, and can tear out matter from the companion. Because these matter carry angular momentum it forms an accretion disc around the CO. Neutron stars in the binaries, (LMXBs and HMXBs) are powered by the energy of matter accreted from companion star.

1.2 Pulsars and Neutron Stars

After the discovery of the neutron by James Chadwick in 1932 scientists speculated on the possible existence of a star composed entirely of neutrons, which would have radius of the order of $R \sim (\hbar/m_n c)(\hbar c/G m_n^2)^{1/2} \sim 3 \times 10^5$cm. First models for the structure of the neutron stars were worked out in 1939 by Oppenheimer and Volkoff (Oppenheimer-Volkoff limit). Unfortunately their pioneering work didnot predict anything astronomers could actually observe, and the idea of NSs was not taken serious by the astronomical community. NSs therefore had remained in the realm of imagination for nearly a quarter of a century, until in the 1960s a series of epochal discoveries were made in high-energy and astronomy.

Neutron stars are fascinating celestial objects both in their observational and their physical properties. Walter Baade and Fritz Zwicky were the first who proposed the idea that neutron stars could be formed in supernovae. When the degeneracy pressure of neutrons balances the gravitational forces of the matter the core radius is about 10 km ($R \approx 10-14$ km) and with a mass $\sim 1.4 M_{\odot}$ ($M \sim 1-2 M_{\odot}$). The mass density $\rho \sim 10^{15}$ g cm^{-3}-roughly 3 times normal nuclear density ($\rho_0 = 2.8 \times 10^{14}$ g cm^{-3}). Conservation of both the angular momentum and the magnetic flux of the progenitor star during the collapse gives the neutron star an extremely high spin rate and magnetic field [3]. Of course their magnetic field evolution and interior composition (exotic interior) remain a mystery.

Neutron star types are classified according to the primary power source for their emission and spin evolution. They prefer to radiate most of their energy at X-ray and gamma-ray wavelengths. Their emission is powered by rotation, accretion, magnetic fields. Rotation-powered pulsars (RPP) derive their energy primarily from the rotation of the NS, magnetars from magnetic field energy. APPs, AMXPs and LMXBs are binary systems where a NS accretes matter from its companion, and conversion of the gravitational binding energy of the accreted matter powers X-ray emission.

Among the classes of neutron-star sources, RPPs and APPs are universally believed to have the ”standard” surface field-strengths of 10^{12} G canonical for neutron stars, with a rough spread of about one order of magnitude around this value. Magnetars are thought to have superstrong fields $\sim 10^{14}-10^{15}$ G by this standard, whence the name. By contrast, LMXBs and AMXPs are thought to have fields $\sim 10^{8}-10^{9}$ G, low by the above standards. Such low fields are believed to have been produced by a reduction of the standard neutron-star field strengths in the process of recycling which occurs during the long accretion phases in LMXBs.

1.2.1 Rotation Powered Pulsars (RPPs)

Rotation-powered pulsars are rapidly spinning, strongly magnetized NSs radiating at the expense of their rotational energy. Using this concept we can get information on NS/Pulsar parameters, from period and period derivatives. A NS with canonical radius of R = 10 km and mass of M=1.4 $M_{\odot}$ has a moment of inertia I $\approx$ (2/5)MR^2. The rotational energy of such star E_{rot} = $2\pi^2 IP^{-2}$. The period derivative implies a decrease in star’s rotation energy according to the relation [32]

$$\frac{dE_{rot}}{dt} = \dot{E_{rot}} = -I\Omega\dot{\Omega} = 4\pi^2 I\dot{P}P^{-3}. \tag{1.2.1}$$

More than 1700 rotation-powered pulsars are known. Each pulsar is identified by its position on the sky in terms of two angles, right ascension and declination, where the sequence of numbers is preceded by the letters PSR. The first pulsar discovered is PSR 1919+21, the Crab pulsar is PSR 0531+21, the (Hulse-Taylor) binary pulsar is PSR 1913+16, the first millisecond pulsar discovered is PSR 1937+21, and so on [31]. A young neutron star starts operating as a rotation-powered pulsar if it is rotating fast enough, and if its magnetic field is large enough. If such a pulsar is single, then either (a) it was born in the supernova of a massive, single star, or, (b) it was born in a binary, but the supernova that created it disrupted the binary. A large majority of the known rotation-powered pulsars is single.

Young rotation-powered pulsars in binaries, can have a ”normal” star as a companion. The majority of RPPs are single, relatively young NS, but there is a population of RPPs in binaries, consisting mostly of old, recycled NSs with low mass companions, and also a small number of young NSs with massive companions. In the mid-life of such neutron-star binaries, during the accretion phase from the companion to the neutron star, the latter becomes an accretion-powered pulsar.

1.2.2 Accretion Powered Pulsars (APPs)

Accretion powered pulsars (APPs) are binary X-ray pulsars rotating, accreting neutron stars. About 110 APPs are known with their periods ranging from 1.7 milliseconds to

9860 seconds. Cen X-3 (in constellation Centaurus) is the first accretion-powered pulsar discovered by Uhuru with period of 4.84 seconds in 1971. Her X-1 is the second discovered in the constellation of Hercules by the end of 1971 with a period of 1.24 seconds. The standard model of compact X-ray sources and accretion-powered pulsars (APPs), contains a binary system of a neutron star or a black hole and a normal companion star. When the companion transfers mass to the compact object by one or more of several possible mechanisms, its gravitational energy is converted into electromagnetic radiation, primarily X-rays.

The source of power for the X-ray emission from binary X-ray pulsars could not be the rotational energy ($E_{rot} = \frac{1}{2}I\Omega^2$) as it is low to account for the observed luminosities ($\sim 10^{37}$ erg s^{-1}). Accretion is the only source of power for such class of X-ray binary pulsars [4].

1.2.3 Accretion Powered Millisecond X-ray Pulsars (AMXPs)

Millisecond pulsars (MSPs) are believed to have been produced by the recycling of neutron stars in low-mass X-ray binaries (LMXBs), where accretion had both (a) spun up the neutron stars to millisecond periods and (b) reduced their magnetic fields to the order $10^8 - 10^9$ G [3]When compared to the canonical radio pulsar population, they are distinguished by short spin periods, P$\lesssim$25 ms, small spin-down rates, $\dot{P} \gtrsim 10^{-20}$, and thus low inferred dipole magnetic field strengths, $B_{dipole} \propto (P\dot{P})^{1/2} \sim 10^8$-$10^{10}$ G, with large characteristic ages, $\tau \equiv P/2\dot{P} \gtrsim 1$ Gyr. Studies of the ≈150 known MSPs are difficult at wave bands outside of the radio due to their intrinsic faintness. The vast majority (≈80%) of MSPs have binary companions that dominate at optical wavelengths; thus, X-rays are an important avenue for studying MSPs [20].Such systems of accreting neutron stars have low magnetic fields of the order $10^8 - 10^9$ G. They are believed to have been produced by the recycling of neutron stars in low-mass X-ray binaries (LMXBs), where accretion had both (a) spun up the neutron stars to millisecond periods and (b) reduced their magnetic fields to the above levels. [32]

1.2.4 Magnetars

Magnetars are believed to generate X-rays by conversion of the magnetic energy stored in the twisted magnetospheres of neutron stars with superstrong magnetic fields. This energy release near the stellar surface is thought to produce hot spots, which emit thermal X-rays through the very thin (typically 1 - 10 cm thick) neutron-star atmosphere. There are two sub-classes of magnetars, Anomalous X-Ray Pulsars (AXPs) and Soft Gamma-Ray Repeaters (SGRs), that were thought for many years to be separate and unrelated objects. Today, we know that SGRs and AXPs are both NSs possessing magnetic fields of unprecedented strength of $10^{14} - 10^{16}$ G, and that show both steady X-ray pulsations as well as soft γ-ray bursts. They are two varieties of the same type of object, isolated NSs possibly powered by magnetic field decay. In both sources, the high-state quiescent luminosities of $L_x \sim 10^{35}$ erg s^{-1} are much higher than their magnetic dipole spin-down luminosities of $\dot{E}_x \sim 2-6\times10^{33}$ erg s^{-1}, demanding an alternative power source [4].

1.3 X-ray Emission from Pulsars and Neutron Stars

X-rays and gamma-rays can only be observed from above the earth's atmosphere, which requires detectors to operate from high flying balloons, rockets or satellites. One of the first X-ray detectors brought to space was launched by Herbert Friedman and his team at the Naval Research Laboratory in order to investigate the influence of the solar activity on the propagation of radio signals in the earth's atmosphere. Results from high-energy cosmic ray experiments suggested that there exist celestial objects (e.g., supernova remnants) which produce high energy cosmic rays in processes which, in turn may also produce X-rays and gamma-rays. These predictions were confirmed in 1962, when the team led by Bruno Rossi and Riccardo Giacconi accidentally detected X-rays from Sco X-1.

On July 4, 1054 AD, Chinese Astronomers noted a guest star in the constellation Taurus. This event marked the arrival of light from the death of a massive main sequence star which underwent a core collapse when its internal thermal energy produced by the nuclear fusion processes was not sufficient any more to counteract the gravitational force against the star’s collapse. The cloud of gas which we observe today at the position of this guest star is the Crab Supernova remnant. In the optical band the nebula has an extent of 4×6 arcmin, corresponding to $\sim 7 \times 10$ light years for a distance of 2kpc [32].

1.3.1 The Magnetosphere

An enormous electric field is induced by the rotation of a magnetised NS. This field tears particles from the stellar surface and accelerates them up to high energies. As a result, these ”primary” particles initiate an electron-positron cascade, which according to conventional wisdom, populates the entire magnetosphere with plasma. In the aligned case, solutions have been found for the region well within the light cylinder in which this plasma is confined to domes above the poles and a differentially rotating equatorial disk. If on the other hand, the magnetosphere is filled with plasma, the strength of the magnetic field is sufficient to ensure that the plasma co-rotates. At some point near the light cylinder, co-rotation must cease, and the particles escape, carrying away magnetic flux and energy in the form of an ultra relativistic, magnetic wind [32].

1.3.2 The Electromagnetic radiations at NS Magnetospheres

The rotation powered pulsar (RPP) radiates at the expense of its rotational energy (pulsars spins down as rotational energy is radiated away) and that rotational energy is lost via electromagnetic radiation of the rotating magnetic dipole/quadrupole and emission of relativistic particles. The particles are accelerated in the pulsar magnetosphere along the curved magnetic field lines and emit the observed intense curvature and synchrotron radiation. This curvature radiation is closely related to synchrotron radiation caused by gyration of particles around the magnetic field lines.

1.4 Black Holes

Quasars and microquasars are among the most intriguing astrophysical objects ever discovered.BH accretion disks might reveal some of the unique signatures of strong gravity: the event horizon, the innermost stable circular orbit, and the ergosphere.

1.4.1 Event Horizon

This is a sphere of radius $\sim GM/c^2$ surrounding the black hole singularity, from within which nothing may emerge. This means that black holes have no rigid surfaces. This is a unique signature of black holes; other relativistic features may be observable around non-black hole objects, specifically sufficiently compact neutron stars, but the event horizon is a defining property of black holes.

1.4.2 Ergosphere

This is a region around a rotating black hole where spacetime itself is dragged along in the direction of rotation at a speed greater than the local speed of light in relation to the rest of the universe. In this region, negative energy states are possible, which means that the rotational energy of the black hole can be tapped through various manifestations of the ”Penrose process”.

1.4.3 Marginally stable orbit

This is the smallest circle ($R = R_{ms}$) along which free particles may stably orbit around a black hole. No stable circular motion is possible for $R < R_{ms}$. This is a unique feature of relativity, as in Newtonian theory, orbits at all radii are possible.

1.5 X-ray Binaries (XRBs)

X-ray binaries are systems that consist of a compact object orbiting an optical companion. They are ”close” binary systems because there exists a transfer of mass from the optical component to the compact object. ”Optical companion” denotes nuclear burning is still taking place in its interior. X-ray binaries divide up into blackhole systems, neutron star X-ray binaries or cataclysmic variables (if the compact object is a white dwarf). In massive X-ray binaries, the most massive star is normally termed primary whereas the less massive one is called secondary. In lowmass systems, the term primary refers to the neutron star while the word secondary is reserved for the latetype companion. The term ”X-ray binaries” is normally reserved for binaries with neutron stars. Neutron-star X-ray binaries divide into high-mass and low-mass systems according to whether the mass of the donor star is above ~ 8 or below $\sim 2M_{\odot}$, respectively.

1.5.1 Low-Mass X-ray Binaries (LMXBs)

Bright, accretion-powered galactic-bulge LMXBs are among the brightest X-ray binaries known, and are widely believed to be the nurseries producing AMXPs by recycling. Their persistent X-ray emission does not show periodicity at any possible rotation period relevant for neutron stars, although they are thought to harbor fast-rotating neutron stars with millisecond periods. Various explanations have been offered for this, e.g., (a) that the emitted pulses are washed out by the dense plasma surrounding the neutron star, or (b) that their rotation and magnetic axes have become aligned by accretion torques, so that they actually do not pulse.

Many LMXBs undergo X-ray bursts, and coherent pulsations at millisecond periods have been detected during these bursts in about twenty of them so far. Identifying this periodicity with that of the neutron stars rotation, we can again use the above ideas of pulse phase polarimetry as a diagnostic probe of the emission geometry in these systems. These bursts are thought to be due to the ignition of thermonuclear reactions in the accreted material upon reaching a critical temperature and density, deep in the atmosphere of the neutron star where the optical depth is extremely large.

1.5.2 High-Mass X-ray Binaries (HMXBs)

Neutron-star X-ray binaries are divided up into highmass (HMXBs) and low-mass (LMXBs) X-ray binaries depending on the spectral type of the mass donor, as this feature determines the mode of transferring mass to the compact object and the environment surrounding the X-ray source. HMXBs contain early-type (O or B) companions, while the spectral type of the optical star in LMXBs is later than A. HMXBs are strong emitters of X-ray radiation. Sometimes they appear as the brightest objects of the X-ray sky. The high-energy radiation is produced as the result of accretion of matter from the optical companion onto the neutron star during accretion. Based on evolutionary status of the optical companion, HMXBs is subdivided in to two as, low-luminosity or wind-fed systems - supergiant X-ray binaries (SGXBs) and high-luminosity or disc-fed systems - Be/X-ray binaries (BeXB), when the optical star is a dwarf. In SGXBs, the optical star emits a substantial stellar wind, removing between 10^{-6}-10^{-8} $M_{\odot}$ yr^{-1} with a terminal velocity up to 2000 km s^{-1}. A neutron star in a relatively close orbit will capture some fraction of this wind, sufficient to power a bright X-ray source. If mass transfer occurs via Roche lobe overflow, then the X-ray emission is highly enhanced and an accretion disc is formed around the neutron star. At present, there is known only one disc-fed SGXB in the Galaxy (Cen X-3) and three in total (SMC X-1 and LMC X-4), while there are about a few tens of wind-fed SGXBs. In BeXB, the optical companion is a Be star. Be stars are non-supergiant fast-rotating B-type and luminosity class III-V stars. Virtually all Be/X-ray binaries show X-ray pulsations.

Table 1.1: Statistics on HMXBs in the Milky Way

Number of Neutron-star X-ray binaries	327
Number of suspected HMXB	131
Number of suspected BeXB	63
Number of confirmed BeXB	28

Other newly discovered systems may not fit in these categories. Since its launch in October 2002, INTEGRAL has unveiled a population of highly obscured HMXBs with supergiant companions and a new type of source displaying outbursts which are significantly shorter than typical for BeXB and which are characterized by bright flares with a duration of a few hours and peak luminosities of 10^{36} - 10^{37} $ergs^{-1}$. These new systems have been termed as Supergiant fast X-ray Transients (SFXTs). Both obscured HMXBs and SFXTs display X-ray and IR spectra typical of SGXBs. SFXTs differ from SGXBs because they are only detected sporadically, during very brief outbursts.

Table 1.1 shows the number of various types of X-ray binaries. Neutron stars in binaries evolve with time as the binary systems themselves evolve, so that the pulsars pass from a young, rotation-powered phase to a middle-aged, accretion-powered phase, and, finally, to an old, recycled phase, in which they are powered by rotation once again. The first mass transfer in the binary evolution always starts from the primary, i.e., the more massive star, to the less massive one, so that, at first, the orbit always shrinks and the orbital period decreases. The black hole binaries are massexchange binaries that contain an accreting black hole primary and a nondegenerate secondary star. They comprise about 10 % of all bright Xray binaries. The BHBs range in size from tiny XTE J1118+480 with P_{orb} = 0.17 days and a separation between the BH and its companion of a ≈ 2.8 $R_{\odot}$ to GRS 1915+105 with P_{orb} = 33.5 days and a ≈ 95 $R_{\odot}$. Low-mass X-ray binaries (LMXBs) contain a secondary with a mass of roughly 1 $M_{\odot}$ or less. The BHBs 4U1543-47 and SAX J1819.3-2525 have relatively massive secondaries: 2.7±1.0 $M_{\odot}$ and 2.9 ±0.2 $M_{\odot}$, respectively We classify them as LMXBs because their secondary masses are comparable to the mass of the secondary of Her X-1 (2.3 ± 0.3 $M_{\odot}$), which is a well-known LMXB. Furthermore, a 2-3 $M_{\odot}$ secondary is much less massive than the O/B secondaries (≈10 $M_{\odot}$) found in HMXB systems.

Black holes are among the most striking predictions of Einstein's theory of General Relativity: So much mass is compressed into such a small volume that gravity overwhelms all other forces, and nothing - not even light can escape. Instead of a normal surface, a black hole has an event horizon, a virtual surface that separates the outside world from the region of the black hole from which nothing escapes. Remarkably, General Relativity predicts that macroscopic black holes such as those that are studied in astrophysics are extremely simple objects; they can be completely described by just two parameters: their mass and spin.

The Black hole masses may vary from a few solar mass to supermassive BHs with masses between 10^6 and 10^9 $M_\odot$. It is not clear so far whether there are intermediate mass BHs between these two extremes. Black holes with masses of $\sim$10 $M_\odot$ form when stars in the range $\sim$30 to 100 $M_\odot$ exhaust their nuclear fuel and collapse under their own weight there are perhaps 10 million such black holes in a galaxy like the Milky Way. Most are dark and invisible, but some become powerful sources of X-rays when they accrete matter from a companion star; these are called X-ray binaries (XRBs). More speculatively, the accretion of matter onto a newly formed black hole at the center of a collapsing star may give rise to gamma-ray bursts, the most energetic explosions in the universe. Nearly every Galaxy contains massive BHs, in the range 10^6 and 10^9 $M_\odot$ at its center. The most direct evidence comes from elliptical orbit stars around the BH at the center of our Galaxy with mass of $\sim 3.7 \times 10^6$ $\mathrm{M}_\odot$.

1.6 Accretion disk models

Accretion disks are associated to different astrophysical objects in the universe like: young stars (T Tauri)-probably sites of planetary formation; close binary systems like β-Lyra, cataclysmic variables, novae, X-ray binaries, and active galactic nuclei (AGN) etc.The most spectacular accretion disks found in nature are those of active galactic nuclei and of quasars, which are believed to be massive black holes at the center of galaxies. Quasars and other similar supermassiveobjects, are collectively called ”active galactic nuclei”(or AGN), have masses in the range $10^6 M_\odot < M < 10^9 M_\odot$.As matter follows the tendex line into a black hole, the intense gravitational gradient gives rise to intense frictional heating; the accretion disk of a black hole is hot enough to emit X-rays just outside of the event horizon. The large luminosity of quasars is believed to be a result of gas being accreted by supermassive black holes. This process can convert about 10 percent (high efficiency, $\eta \equiv L/\dot{M}c^2 > 0.1$) of the mass of an object into energy as compared to around 0.5 percent for nuclear fusion processes.

The accretion disk model grew in popularity and began to be recognized as the theory capable to describe important energetic emissions observed in the Universe. After the confirmation of quasars, in 1973 that Shakura & Sunyaev proposed a fundamental theory of accretion disks known as the standard accretion disk model or simply the α-disk model. Very soon, in the same year, it was generalized to the relativistic version by Novikov & Thorne (1973) [16].

In close binary systems the more massive primary component evolves faster and has already become a white dwarf, a neutron star, or a black hole, when the less massive companion reaches the giant state and exceeds its Roche lobe. A gas flow then develops from the companion star to the primary. Angular momentum conservation prevents a straight flow from one star to the other and an accretion disk forms instead.

Accretion disks surrounding T Tauri stars or Herbig stars are called protoplanetary disks because they are thought to be the progenitors of planetary systems. The accreted gas in this case comes from the molecular cloud out of which the star has formed rather than a companion star.

In the 1940s, models were first derived from basic physical principles. In order to agree with observations, those models had to invoke a yet unknown mechanism for angular momentum redistribution. If matter is to fall inwards it must lose not only gravitational energy but also lose angular momentum. Since the total angular momentum of the disk is conserved, the angular momentum loss of the mass falling into the center has to be compensated by an angular momentum gain of the mass far from the center. In other words, angular momentum should be transported outwards for matter to accrete.

On one hand, it was clear that viscous stresses would eventually cause the matter towards the center to heat up and radiate away some of its gravitational energy. On the other hand, viscosity itself was not enough to explain the transport of angular momentum to the exterior parts of the disk. Turbulence-enhanced viscosity was the mechanism thought to be responsible for such angular-momentum redistribution, although the origin of the turbulence itself was not well understood. The conventional phenomenological approach introduces an adjustable parameter describing the effective increase of viscosity due to turbulent eddies within the disk.

The standard disk model (Shakura & Sunyaev 1973) has been widely and successfully used to account for the blackbody component. However, optically thin, hot accretion disks have been studied to account for hard X-rays from BHCs. The Shakura & Sunyaev model, described a relatively cold disk (in range $\sim 10^2 - 10^5$ K for typical case of quasars) due an efficient process of conversion and evacuation of gravitational energy into radiation. The disk was also assumed geometrically thin and optically thick. They introduced a clever parameterization for the turbulent viscosity, needed to guarantee the transfer of angular momentum and the process of accretion flow.

Based on disk physical structure (geometry): Thin disks, Thick and Slim disk models are considered. On the other hand, based on its different features: hot disks, radiatively inefficient disk, advective disk model etc. In this work we are concerned with thin disk model.

The key assumption of the standard model, that the dissipated energy is radiated away locally, is relaxed in the presently popular models of advection-dominated accretion flows (ADAFs). There are two types of ADAFs: super-critical and two temperature. In both models, a large fraction of the released energy is stored in the gas and advected into the black hole instead of being radiated away. Advective disks are geometrically thick, and a two-dimensional (2D) approach would be more adequate to the problem. Most of the models are, however, based on the vertically integrated (1D) equations due to their simplicity. The α-parametrization of viscosity is used in the same manner as in the standard model.

In 1991, with the rediscovery of the magnetorotational instability (MRI), Balbus & Hawley established that a weakly magnetized disk accreting around a heavy, compact central object would be highly unstable, providing a direct mechanism for angular-momentum transport. The differential character of disk rotation, which is quasi-Keplerian produces MHD turbulence. The turbulent pulsations in turn force each gas element to diffuse from one orbit to another, and a ring of gas spreads out to form an extended disk. At the inner edge of the disk gas is channeled by MF so that it is accreted by central star (NS). The orbiting mass elements being coupled magnetically, pull on each other as the shear attempts to separate them as if connected by a weak spring.The inner fluid element of the disk would orbit more rapidly than the outer, causing the spring to stretch. The inner fluid element is then forced by the spring to slow down, reduce correspondingly its angular momentum causing it to move to a lower orbit. The outer fluid element being pulled forward will speed up, increasing its angular momentum and move to a larger radius orbit. The spring tension will increase as the two fluid elements move further apart and the process runs away, thus removing angular momentum.The redistribution of angular momentum is accompanied by a viscous heating. As a result, the binding energy of spiraling gas is dissipated into heat and can be radiated.

The most important scale in accretion disk theory is the Eddington accretion rate, $\dot{M}_E = L_E/c^2 = 1.7 \times 10^{17}(M/M_\odot)$ g/s. Based on this accretion rate we can divide ADs into two as sub-Eddington and super-Eddington disks.

1.6.1 Sub-Eddington accretion disks

These include thin disks and ADAFs. The Shakura-Sunyaev α-Disk model is both thermally and viscously unstable. An alternative model, known as the β-disk, which is stable in both sense assumes that the viscosity is proportional to the gas pressure. In the standard Shakura-Sunyaev model, viscosity is proportional to the total pressure. This model assumes that the disk is in local thermal equilibrium, and can radiate its heat efficiently. In this case, the disk radiates away the viscous heat, cools, and becomes geometrically thin. However, this assumption may break down. In the radiatively inefficient case, the disk may ”puff up” into a torus or some other three dimensional solution like an Advection Dominated Accretion Flow (ADAF). The ADAF solutions usually require that the accretion rate is smaller than a few percent of the Eddington limit.

When the accretion rate is sub-Eddington and the opacity very high, the standard thin accretion disc is formed. It is geometrically thin in the vertical direction (has a disk-like shape), and is made of a relatively cold gas, with a negligible radiation pressure. The gas goes down on very tight spirals, resembling almost circular, almost free (Keplerian) orbits. Thin disks are relatively luminous and they have thermal electromagnetic spectra, i.e. not much different from that of a sum of black bodies. Radiative cooling is very efficient in thin disks.

When the accretion rate is sub-Eddington and the opacity very low, an ADAF is formed. ADAFs started to be intensely studied by many authors only after their rediscovery in the mid-1990 by Narayan and Yi, and independently by Abramowicz, Chen, Kato, Lasota (who coined the name ADAF), and Regev. Most important contributions to astrophysical applications of ADAFs have been made by Narayan and his collaborators. ADAFs are cooled by advection (heat captured in matter) rather than by radiation. They are very radiatively inefficient, geometrically extended, similar in shape to a sphere (or a ”corona”) rather than a disk, and very hot (close to the virial temperature). Because of their low efficiency, ADAFs are much less luminous than the Shakura-Sunyaev thin disks. ADAFs emit a power-law, non-thermal radiation, often with a strong Compton component. Thin accretion disks are consistent with accretion rates $\dot{M} << \dot{M}_E$, and thick accretion disks with $\dot{M} >> \dot{M}_E$. Whereas Slim disks are those with accretion rates $\dot{M} \approx \dot{M}_E$. They are different from both thin and thick accretion disks in several astrophysically important respects.

For an alternate description we can define critical accretion rate as $\dot{M}_c = \frac{L_E}{\eta c^2} = 10\dot{M}_E = 1.7 \times 10^{17}(M/M_\odot)$ g/s, where $L_E \approx 10^{38}(M/M_\odot)$g/s, is the Eddington luminosity and $\eta \approx 0.1$, is the efficiency of accretion. Slim accretion - disk models can very roughly be characterized by $0.1 \leq \dot{M}/\dot{M}_c$.

1.6.2 Super-Eddington accretion disks

These include slim disks and Polish doughnuts. The theory of highly super-Eddington black hole accretion, $\dot{M} >> \dot{M}_{Edd}$, was developed in the 1980s by Abramowicz, Jaroszynski, Paczynski, Sikora and others in terms of ”Polish doughnuts” (the name was coined by Rees). Polish doughnuts are low viscosity, optically thick, radiation pressure supported accretion diks cooled by advection. They are radiatively very inefficient. Polish doughnuts resemble in shape a fat torus (a doughnut) with two narrow funnels along the rotation axis. The funnels collimate the radiation into beams with highly super-Eddington luminosities.

Slim discs have only moderately super-Eddington accretion rates, $M = M_{Edd}$, rather disk-like shapes, and almost thermal spectra. They are cooled by advection, and are radiatively ineffective. They were introduced by Abramowicz et al. in 1988 [1].

All these models showed a good agreement with observations. Accretion disk is now the accepted paradigm in order to describe several energetic phenomena either on small scales, like disks around Young stellar object (YSO), or Cataclysmic variable stars (CV) or on large scales, like AGNs or quasars. The central idea of accretion disks lies in the fact that the accreting masses possess a considerable amount of angular momentum per mass unit which has to be removed in order to be accreted into the central object. What causes the loss of angular momentum is the friction caused by turbulent viscosity working between adjacent gas layers in the disk. The faster inner layer loses angular momentum and infalls slightly, while the next (slower) outer layer gains angular momentum, which is given away to the next outer layer, and so on, resulting in a continuous flow toward the centre whereas angular momentum is transported to the outer region The friction of the disk heats up the gas, resulting in a continuous radiation emission, which is believed to be the source of AGNs, quasars, X-ray binaries, luminosities (among other phenomena) as mentioned above [17].

1.6.3 Quasiperiodic Oscillations (QPOs)

As with any finite distribution of fluid, accretion disks have natural oscillation modes associated with them. If these modes can be excited at appreciable amplitudes, they may be able to modify the observed light curve of the disk in measurable ways. Even when analytic disk solutions are stable against finite perturbations, it is often the case that these perturbations will, nevertheless, excite oscillatory behavior. Oscillations are a common dynamical response in many fluid (and solid) bodies. There are a number of local restoring forces available in accretion disks to drive oscillations. Local pressure gradients can drive oscillations via sound waves. Buoyancy forces can act through gravity waves. The Coriolis force can operate through inertial waves. Surface waves can also exist, with the restoring force given by the local effective gravity. Of particular interest are families of low order modes that may exist in various accretion geometries. Such modes will tend to have the largest amplitudes and produce more easily observed changes than their higher-order counterparts [16]. All of the above classes of NS X-ray sources exhibit periodic pulses at the rotation

Table 1.2: Accretion Powered Pulsars-Spin frequencies are assumed to lie within the range of observed QPO peak separations

Source	Frequency ratio
GX 340+0	251/435 = 0.577
GX 5-1	219/357 = 0.613
4U 1820-30	220/350 = 0.628
Sco X-1	232/312 = 0.74
GX 17+2	222/322 = 0.689
XTE J2123-058 5-1	222/322 = 0.689

period of the NS, except for LMXBs, for which these pulses are believed to be unobservable or absent,although the neutron stars in these sources are thought to be rotating fast as a result of the recycling process which they are undergoing. However, many LMXBs undergo X-ray bursts, and during the bursts from some of them, periodic oscillations have been observed at high frequencies, which are believed to be the spin frequencies (or simple multiples/submultiples) of the underlying neutron stars. Some examples are shown in Table 1.2.

Also in several microquasars the detected high-frequency QPOs come not as single oscillations, but as part of a pair. Furthermore, Abramowicz and Kluźniak noticed that they are commensurable, being most often in a 2/3 ratio, as shown in Table 1.3. This suggests that a resonance may be at work. Twin peak QPOs in the kilohertz range have been also detected from binaries containing accreting neutron stars. These neutron star QPOs show a similar, though less obvious, 2/3 ratio.

Table 1.3: Frequency ratio of the twin peak QPOs in all four microquasars where they have been detected

Microquasar	Frequency ratio
GRO J1655-40	300/450 = 0.66
XTE 1550-564	184/276 = 0.66
H 1743-322	166/240 = 0.69
GRS 1915+105	113/168 = 0.67

A major property of bright LMXBs in the time or frequency domain is the quasiperiodic oscillation (QPO) exhibited by them. QPOs appear as relatively wide, but clearly discernible, peaks in the power spectra of LMXBs, as opposed to the extremely sharp peaks corresponding to periodic pulses that appear in the power spectra of APPs. QPOs occur at both low frequencies ($\nu_{QPO} \sim 6-50Hz$) and high kilohertz frequencies ($\nu_{QPO} \sim 400-1000Hz$), and they have also been detected recently at intermediate hectohertzfrequencies. The study of QPOs and their relations with LMXB spectral states has become a most valuable diagnostic tool for probing the dynamics of inner accretion disks and the interactions between neutron stars and accretion disks.

Chapter 2

Accretion Disk around Magnetized Stars I - Keplerian Thin Disk

2.1 Introduction

In this chapter we consider thin Keplerian disk - geometrically thin and optically thick magnetohydrodynamical model to generalize the standard radiatively efficient disk around compact objects. In Sect. 1 we introduce the relevant MHD equations to derive a dimensionless function to solve the equation of angular momentum conservation. We employ the kinematic viscosity and solve the equation of angular momentum conservation for the rotation profile of a disk around a neutron star. In Sect. 2.2 we describe the inner part of an accretion disk in a quadrupolar field. In Sect. 2.3 we discuss the significance of the results obtained in this work. Finally we summarize our results in Sect. 2.4.

2.2 The Mathematical Description of Keplerian Thin Disk

Accretion discs are often assumed to be geometrically thin. This means that the typical length scale in the vertical direction, the disc half thickness H, is much smaller than the radial distance from the central object, R. The structure of an accretion disk is determined by the basic equations of viscous fluid dynamics: the continuity equation, Navier-Stoke's equation and the equation of conservation of energy, to which we add the effect of the magnetic field through the Lorentz force.

2.2.1 Conservation of Mass

The condition of mass conservation of fluid in a flow directly leads to continuity equation

$$\frac{\partial \rho}{\partial t} + \nabla \cdot (\rho \mathbf{v}) = 0 \tag{2.2.1}$$

where ρ is density and $\mathbf{v}$ is the fluid velocity. In cylindrical symmetry the steady continuity equation becomes

$$\frac{1}{R}\frac{\partial}{\partial R}(\rho R v_R) + \frac{\partial}{\partial z}(\rho v_z) = 0 \tag{2.2.2}$$

and following the thin disc approximation we ignore the vertical velocity and integrate in the vertical direction across the disc, which gives us that the mass accretion rate is

$$\dot{M} = -2\pi R \Sigma(R) v_R, \tag{2.2.3}$$

where Σ is the surface density defined by

$$\Sigma(R) = \int_{-H}^{H} \rho(R,z)dz = 2\rho(R)H, \tag{2.2.4}$$

where $\rho(R)$ denotes the vertically averaged density and H is the half-thickness of the disc.

2.2.2 Conservation of momentum (Navier - Stoke's equation)

The general form of the Navier-Stoke's equation for fluid motion is:

$$\rho\frac{d\mathbf{V}}{dt} = -\nabla p + \nabla\cdot\tau + \mathbf{f} \tag{2.2.5}$$

or

$$\rho\frac{\partial\mathbf{v}}{\partial t} + \rho(\mathbf{v}\cdot\nabla)\mathbf{v} = -\nabla p + \nabla\cdot\tau + \mathbf{f} \tag{2.2.6}$$

where p is the pressure, τ is the stress tensor, and **f** represents body forces per unit volume acting on the fluid. Assuming a steady state the Navier-Stokes equation can be written in the form

$$\rho(\mathbf{v}\cdot\nabla)\mathbf{v} = -\nabla p - \nabla\psi + J\times B + \nabla\cdot(\rho\nu(\nabla\mathbf{v} - \frac{2}{3}\nabla\cdot\mathbf{v})) \tag{2.2.7}$$

where ψ is gravitational potential. Each of the three components of the Navier-Stokes equation defines some important properties of accretion discs as shown below.

2.2.3 Vertical structure: hydrostatic equilibrium

For steady, axisymmetric disk the vertical component of Eq. (2.2.5) is given by:

$$\rho\left(V_R\frac{\partial V_z}{\partial R}+V_z\frac{\partial V_z}{\partial z}\right)=-\left(\frac{\partial p}{\partial z}\right)-\rho\left(\frac{\partial\psi}{\partial z}\right)+\left(\frac{B_\phi}{\mu_0}\left(\frac{\partial B_\phi}{\partial z}\right)-\frac{B_R}{\mu_0}\left(\frac{\partial B_R}{\partial z}\right)+\frac{B_R}{\mu_0}\left(\frac{\partial B_z}{\partial R}\right)\right) \tag{2.2.8}$$

Then since it is equally possible to choose R or z directions, taking components with B_R instead of B_z as a new alternative we can write as

$$\rho\left(V_R\frac{\partial V_z}{\partial R}+V_z\frac{\partial V_z}{\partial z}\right)=-\left(\frac{\partial p}{\partial z}\right)-\rho\left(\frac{\partial\psi}{\partial z}\right)+\left(\frac{B_\phi}{\mu_0}\left(\frac{\partial B_\phi}{\partial z}\right)-\frac{B_R}{\mu_0}\left(\frac{\partial B_R}{\partial z}\right)\right) \tag{2.2.9}$$

Neglecting the time-dependence and vertical outflows, i.e. assuming vertical hydrostatic equilibrium, we can then write the equation as

$$\rho\left(\frac{\partial\psi}{\partial z}\right)=-\frac{\partial}{\partial z}\left(p+\frac{B_R^2+B_\phi^2}{2\mu_0}\right) \tag{2.2.10}$$

Here are gravitational force and pressure force in the vertical direction and such a situation, where gravity is balanced by pressure, is called ”hydrostatic balance”. For a weak magnetic field this reduces to

$$\frac{1}{\rho}\left(\frac{\partial p}{\partial z}\right)=-\frac{\partial\psi}{\partial z}=-\frac{GM}{R^2}\frac{z}{R}. \tag{2.2.11}$$

The pressure p is the sum of gas and radiation pressure

$$p=\frac{\rho k_B T_c}{\bar{\mu} m_p}+\frac{4\sigma T_c^4}{3c}, \tag{2.2.12}$$

where T_c is temperature in the central plane, σ the Stefan-Boltzmann constant and c the speed of light.With $p = c_s^2\rho$ we can then rewrite Eq. (2.2.11) as

$$\frac{c_s^2}{\rho}\frac{d\rho}{dz} = -\frac{GMz}{R^3}, \tag{2.2.13}$$

for which the solution is a Gaussian:

$$\rho = \rho_0 \exp[-z^2/H^2], \tag{2.2.14}$$

where ρ_0 is the midplane density and we have introduced a vertical scale height

$$H = \frac{c_s}{\Omega_K}. \tag{2.2.15}$$

The equation of hydrostatic equilibrium gives us a simple relation between the thickness, the sound speed and the Keplerian rotational velocity, $V_K = R\Omega_K$

$$\frac{H}{R} = \frac{c_s}{V_K}. \tag{2.2.16}$$

This demonstrates that the requirement that the disc is thin is equivalent to that the disc rotation is highly supersonic (i.e. that $V_K \ll c_s$). From vertical integration, we can also re write the radial equilibrium of the disk given by Eq. (2.2.10) as

$$\frac{1}{2}\Omega_K^2\Sigma H = \frac{B_\phi^2}{2\mu_0} + \frac{\rho K_B T_c}{\bar{\mu} m_p} + \frac{4\sigma T_c^4}{3c} \tag{2.2.17}$$

The right hand side of Eq. (2.2.17), is the total pressure and can be also written as

$$P_{tot} = \rho\frac{GM}{r^3}H^2 = \frac{1}{2}H\Sigma\frac{GM}{r^3}, \tag{2.2.18}$$

where P_{tot} is the pressure at the midplane. Solving for H then gives

$$H = \frac{c_s}{\Omega_K} = \frac{1}{\Omega_K}\left(\frac{K_B T_c}{\bar{\mu} m_p} + \frac{4\sigma T_c^4}{3c\rho} + \frac{B_\phi^2}{2\mu_0\rho}\right)^{\frac{1}{2}}, \tag{2.2.19}$$

2.2.4 The Radial equilibrium: centrifugal balance

Radial equilibrium: centrifugal balance.

The radial component of Eq. (2.2.5) takes the form:

$$\rho\left(\frac{\partial V_R}{\partial t} + (V\cdot\nabla)V_R - \frac{V_\phi^2}{R}\right) = -\left(\frac{\partial p}{\partial R}\right) - \rho\left(\frac{\partial\psi}{\partial R}\right) + \left(\frac{B_z}{\mu_0}\left(\frac{\partial B_R}{\partial z} - \frac{B_z}{\partial R}\right) - \frac{B_\phi}{R\mu_0}\left(\frac{\partial(RB_\phi)}{\partial R} - \frac{\partial B_R}{\partial\phi}\right)\right) \text{(2.2.2}$$

$$\rho\left(\frac{\partial v_R}{\partial t} + V\cdot\nabla)V_R - \frac{V_\phi^2}{R}\right) = -\left(\frac{\partial p}{\partial R}\right) - \rho\left(\frac{\partial\psi}{\partial R}\right) + B_z J_\phi - \frac{B_\phi}{R\mu_0}\left(\frac{\partial(RB_\phi)}{\partial R}\right) \tag{2.2.21}$$

Ignoring the time dependence and with the assumption that the disk is axisymmetric this equation can be rewritten as

$$\frac{\partial}{\partial R}\left(\frac{V_R^2}{2}\right) + \left(\frac{\partial\psi}{\partial R}\right) - \frac{V_\phi^2}{R} + \frac{1}{\rho}\frac{\partial}{\partial R}\left(P + \frac{B_\phi^2}{\mu_0}\right) - \frac{1}{\rho}B_z J_\phi = 0 \tag{2.2.22}$$

where the toroidal current density, $J_\phi = \frac{1}{\mu_0}(\frac{\partial B_R}{\partial z} - \frac{\partial B_z}{\partial R})$. For convenience we used the magnetic pressure to include the Lorentz force component in the radial forces. An accretion disc kept in equilibrium by the balance between the gravitational acceleration, centrifugal acceleration and the pressure gradient fulfills the equation

$$\frac{V_\phi^2}{R} - \frac{1}{\rho}\frac{\partial}{\partial R}\left(P + \frac{B_\phi^2}{\mu_0}\right) - \left(\frac{\partial\psi}{\partial R}\right) = 0 \tag{2.2.23}$$

For non-magnetic disk or weak magnetic field cases this reduces to:

$$\frac{V_\phi^2}{R} = \frac{1}{\rho}\left(\frac{\partial p}{\partial R}\right) + \left(\frac{\partial \psi}{\partial R}\right), \tag{2.2.24}$$

Since for thin disks $c_s \ll V_\phi$,this gives

$$\frac{V_\phi^2}{R} \simeq \frac{\partial \psi}{\partial R}, \tag{2.2.25}$$

The gravitational potential of the central star, $\psi = -\frac{GM}{R}$ yields Keplerian rotation, that the angular velocity is $\Omega_K = (GM/R^3)^{1/2}$.

2.2.5 Angular momentum conservation

The last component of Navier-Stokes equation, in which the viscous term plays an important role describes the angular momentum conservation along r, given by:

$$\begin{aligned}\rho\left(\frac{V_R}{R}\frac{\partial}{\partial R}(RV_\phi) + V_z\frac{\partial V_\phi}{\partial z}\right) = \frac{B_R}{\mu_0 R}\left(\frac{\partial(RB_\phi)}{\partial R}\right) + \frac{B_z}{\mu_0}\left(\frac{\partial B_\phi}{\partial z}\right) \\ + \frac{1}{R^2}\frac{\partial}{\partial R}\left(R^3\rho\nu\frac{\partial}{\partial R}\left(\frac{V_\phi}{R}\right)\right)\end{aligned} \tag{2.2.26}$$

or

$$\rho\left(\frac{V_R}{R}\frac{\partial}{\partial R}(RV_\phi) + V_z\frac{\partial V_\phi}{\partial z}\right) = \frac{B_R}{\mu_0 R}\left(\frac{\partial(RB_\phi)}{\partial R}\right) + \frac{B_z}{\mu_0}\left(\frac{\partial B_\phi}{\partial z}\right) + \frac{1}{R^2}\frac{\partial}{\partial R}\left(R^3\rho\nu\frac{\partial}{\partial R}\left(\frac{V_\phi}{R}\right)\right) \tag{2.2.27}$$

The vertically integrated form of the Eq. (2.2.26) becomes

$$\Sigma V_R\frac{\partial \ell}{\partial R} = 2H(R)\frac{\partial}{\partial R}\left(R^2\frac{B_R B_\phi}{\mu_0}\right) + \frac{1}{R}\frac{\partial}{\partial R}\left(R^3\nu\Sigma\frac{\partial}{\partial R}\left(\frac{\ell}{R^2}\right)\right), \tag{2.2.28}$$

2.2.6 Viscosity

Viscosity is the least understood physics in the theory of disk accretion. The molecular viscosity is too small to drive the accretion flow, rather the source of the viscosity is likely to be small scale turbulence in the disk, which is probably caused by the magneto-rotational instability (MRI) (Balbus & Hawley, 1991). Based on mixing length theory the turbulent viscosity can be written as,

$$\nu = \ell V, \tag{2.2.29}$$

where ℓ is a typical turbulent length scale and V a typical turbulent velocity. The length scale of the turbulence cannot be larger than the scale height of the disk, H, and the velocity of the turbulence should be subsonic. Using the Shakura Sunyaev α_{SS} - prescription the kinematic viscosity can be written as

$$\nu = \alpha_{ss} c_s H, \tag{2.2.30}$$

where α_{SS} is a parameter that is ≤ 1. But since the non negligible component of stress tensor is $t_{r\phi}$, the viscous stress tensor can be written for Keplerian case as

$$t_{R\phi} = -\rho \nu R \Omega' = -\frac{3}{2}\eta\Omega, \tag{2.2.31}$$

where ν is the kinematic viscosity and η is dynamic viscosity. Making substitution using Eq. (2.2.18) & (2.2.15) the shear stress in a thin disk is

$$f_{R\phi} = \alpha_{ss} P, \tag{2.2.32}$$

From stress tensor Eq. (2.2.31) and (2.2.32) solving for P we then have

$$P(R) = -\frac{3\Sigma\nu}{4H\alpha_{ss}}\Omega_K, \tag{2.2.33}$$

2.2.7 The Magnetic Field

We investigate the accretion disk formed around magnetic star (NS) with a quadrupolar magnetic field. The stellar quadrupole field in the equatorial plane is given by

$$B_R = B_0\left(\frac{R_s}{R}\right)^4 = \frac{\mu_q}{R^4}, \tag{2.2.34}$$

where B_0 is the field strength at the surface of the star, R_s is radius of the star, R is the cylindrical radius and μ_q is the quadrupole moment. The disk is formed around such magnetic star (NS) in the equatorial plane (z = 0) and it is threaded by quadrupolar magnetic field, that lies in the plane of the accretion disk. The MF structure within the disk is simply determined by the Faraday's induction equation

$$\frac{\partial B}{\partial t} = \nabla \times (V \times B - \eta \nabla \times B), \tag{2.2.35}$$

where η is the magnetic diffusivity of the plasma. The dominant terms are the shear between the disk and the star, the shear due to the differential rotation of the disk, and the vertical diffusion through the disk. The azimuthal component of Eq. (2.2.35)

$$\frac{\partial B_\phi}{\partial t} = \frac{\partial}{\partial z}\left(\eta \frac{\partial B_\phi}{\partial z}\right) + \frac{\partial}{\partial R}\left(V_\phi B_R\right). \tag{2.2.36}$$

Since we look for a stationary solution we ignore the time derivative

$$\frac{\partial}{\partial z}\left(\eta \frac{\partial B_\phi}{\partial z}\right) = -\frac{\partial}{\partial R}(V_\phi B_R). \tag{2.2.37}$$

Assuming that the star is rotating at the angular velocity Ω_S and that the angular velocity of the disk is $\Omega(R)$ we can write

$$V_\phi = R(\Omega - \Omega_S), \tag{2.2.38}$$

Finally solving Eq. (2.2.37) we get the vertical distribution of the toroidal magnetic field

$$B_{\phi,shear}(R,z) = \frac{H^2}{2\eta}\frac{\partial}{\partial R}[(\Omega - \Omega_S)RB_R]. \tag{2.2.39}$$

the toroidal field given by The magnetic diffusivity, like the viscosity, is due to turbulence. In Eq. (2.2.35) the turbulent diffusivity is much stronger than the ohmic one. For simplicity we will assume that $\eta \sim \eta_t \approx \nu$. (e.g. Campbell 1992; Cameron & Campbell 1993; Yi 1995). Using Eq. (2.2.30), we can then rewrite Eq. (2.2.39) as

$$B_{\phi,shear} = -\frac{1}{\alpha_{SS}\Omega_K}\frac{\partial}{\partial R}[(\Omega - \Omega_S)RB_R] \tag{2.2.40}$$

Using the earlier definitions for Ω & B_R, as given in Eqs. (2.2.25) & (2.2.34), and the fact that Ω, Ω_K, β_K & B_R are all R dependent, we arrive at

$$B_{\phi,shear} = \frac{3B_R}{\alpha_{ss}}\left(\frac{3}{2}\beta_K - \frac{\Omega_s}{\Omega_K}\right) . \tag{2.2.41}$$

where $\beta_K = 1$ for Keplerian case. This is the toroidal field generated by the shear between the disk and stellar magnetosphere.

The Rϕ-component of the magnetic stress density inside the disk is

$$f_{R\phi} = \frac{B_R B_\phi}{\mu_0} = \alpha_{ss} P, \tag{2.2.42}$$

Based on the results of numerical simulations of magnetohydrodynamic turbulence in accretion disks there are those who argue (Brandenburg et al.,1995 & Torkelsson, 1998) that

$$\gamma_{dyn} = \frac{B_\phi}{B_R} . \tag{2.2.43}$$

A second toroidal field component, $B_{\phi,dyn}$ is generated by magnetohydrodynamic turbulence in the accretion disk. Using the α -prescription this field, can be estimated as (Tessema & Torkelsson 2010)

$$B_{\phi,dyn} = \varepsilon(\mu_0 \alpha_{ss} \gamma_{dyn} P)^{1/2}, \tag{2.2.44}$$

where $\varepsilon \leq 1$.

From the radial and toroidal field components, ignoring the contribution of the radial dynamo component, we get

$$B_R B_\phi = B_R \left(B_{\phi,shear} + B_{\phi,dyn}\right). \tag{2.2.45}$$

2.2.8 Conservation of energy

The conservation of thermal energy in the disk relating the divergence of the radiative flux to the viscous and magnetic dissipation is given by (e.g. Campbell 2003)

$$\frac{\partial F_R}{\partial z} = \rho\nu(R\Omega')^2 + \frac{\eta}{\mu_0}\left(\frac{\partial B_\phi}{\partial z}\right)^2, \tag{2.2.46}$$

Then vertical integration of the thermal equilibrium equation gives the surface energy flux as the sum of viscous and magnetic dissipations per unit surface area as

$$F_s = \frac{9}{8}\nu\Sigma\Omega^2 + \frac{\eta}{\mu_0}\frac{B_{\phi s}^2}{H}, \tag{2.2.47}$$

The energy flux at height z from the vertical integration is

$$F(z) = \int \frac{\partial F_z}{\partial z} dz = -\frac{4\sigma_B T^4}{3\tau_c}, \tag{2.2.48}$$

In the limit that the optical depth is large, the radiative conduction approximation for the temperature gradient implies that $T_c^4 \approx \frac{3}{4}\tau_c T_e^4$.The emitted surface flux is given in terms of the effective temperature of the disk, T_e, and the Stefan-Boltzmann constant, σ_B by

$$F_s = -\frac{4\sigma_B T_c^4}{3\tau_c} \cong -\sigma_B T_e^4, \tag{2.2.49}$$

Here τ_c, the optical depth at the mid-plane of the disk given by

$$\tau_c = \rho_c H \kappa_c = \rho_c H(\kappa_K + \kappa_{es}), \tag{2.2.50}$$

where ρ_c is the density at the central plane, κ_c is the opacity in the central plane, κ_K is the Kramer's opacity $\kappa_K = \rho_c H \kappa_0 T_c^{-7/2}$, $\kappa_0 = 5 \times 10^{20}\,\mathrm{m^5\,kg^{-2}\,K^{-7/2}}$ and the electron scattering opacity, $\kappa_{es} = 0.04\,\mathrm{m^2\,kg^{-1}}$.

Finally since the energy balance requires that the energy deposited by viscous and magnetic dissipation in each active layer is equal to the energy radiated away at each surface of the disk equating Eq. (2.2.47) and (2.2.49) gives

$$\sigma_B T_{eff}^4 = \frac{9}{8} \nu \Sigma \Omega^2 + \frac{\eta}{\mu_0} \frac{B_{\phi s}^2}{H}, \tag{2.2.51}$$

For an optically thick disk when the local viscous dissipation is balanced by the radiative losses we can solve for central temperature, T_c from Eq. (2.2.51) introducing Eq. (2.2.50) as

$$T_c^4 = \frac{27}{32\sigma_B} \rho H \kappa_c \nu \Sigma \Omega^2. \tag{2.2.52}$$

2.3 The Governing Equations

If we define a function y related to the viscosity by

$$y = \nu \Sigma, \tag{2.3.1}$$

we can, using this definition, rewrite Eq. (2.2.28) as

$$y' = \frac{\dot{M}}{6\pi R} - \frac{y}{2R} + \frac{4H}{\Omega}\left(\frac{B_R B_\phi}{\mu_0}\right) \tag{2.3.2}$$

Inserting Eq. (2.2.33) into Eq. (2.2.44) will give

$$B_{\phi,dyn} = \varepsilon\left(\frac{3\mu_0\gamma_{dyn}\Omega}{4H}\right)^{1/2} y^{1/2}, \tag{2.3.3}$$

or Inserting Eq. (2.2.46) into Eq. (2.2.44) will give

$$B_{\phi,dyn} = \varepsilon(\mu_0 C_p)^{1/2}\gamma_{dyn}^{1/2}\alpha_{ss}^{1/20}M^{7/16}R^{-21/16}(\Sigma\nu)^{17/40}, \tag{2.3.4}$$

where

$$C_p = \frac{3}{4}G^{7/8}\left(\frac{243\kappa_0}{512\sigma}\right)^{-1/20}\left(\frac{\bar{\mu}m_p}{K_B}\right)^{3/8}, \tag{2.3.5}$$

On the other hand Eq. (2.2.41), can be rewritten as

$$B_{\phi,shear} = \frac{3B_R}{\alpha_{ss}}\left(\frac{3}{2} - \left(\frac{R}{R_c}\right)^{3/2}\right), \tag{2.3.6}$$

and R_c is the corotation radius at which the disk angular velocity equals the stellar angular velocity. It is defined by

$$R_c = \left(\frac{GM}{\Omega_s^2}\right)^{1/3} = 1.5\times10^6 M_1 P_{spin}^{2/3} m \tag{2.3.7}$$

where P_{spin} is the spin period and $M_1 = \frac{M}{M_\odot}$.

Substituting Eq. (3.3.3) and Eq. (2.3.6) into Eq. (2.2.45) gives

$$B_R B_\phi = B_R \varepsilon \left(\frac{3\mu_0 \gamma_{dyn} \Omega}{4H}\right)^{1/2} y^{1/2} + \frac{3B_R^2}{\alpha_{ss}} \left(\frac{3}{2} - \left(\frac{R}{R_c}\right)^{3/2}\right), \tag{2.3.8}$$

which when inserted in to Eq. (2.3.2) delivers

$$\begin{aligned} y' = \frac{\dot{M}}{6\pi R} - \frac{y}{2R} + 2\varepsilon B_R \left(\frac{3\gamma_{dyn}}{\mu_0 \Omega_K}\right)^{1/2} (Hy)^{1/2} \\ + \frac{12HB_R^2}{\alpha_{ss}\mu_0\Omega_K} \left(\frac{3}{2} - \left(\frac{R}{R_c}\right)^{3/2}\right) . \end{aligned} \tag{2.3.9}$$

or

substituting Eq. (2.3.4) and Eq. (2.3.6) into Eq. (2.2.45) gives

$$\begin{aligned} B_R B_\phi = \varepsilon(\mu_0 C_p)^{1/2} \gamma_{dyn}^{1/2} \alpha_{ss}^{1/20} M^{7/16} R^{-21/16} (\Sigma\nu)^{17/40} B_R \\ + \frac{3B_R^2}{\alpha_{ss}} \left(\frac{3}{2} - \left(\frac{R}{R_c}\right)^{3/2}\right) \end{aligned} \tag{2.3.10}$$

which when inserted in to Eq. (2.3.2) delivers

$$\begin{aligned} y' = \frac{\dot{M}}{6\pi R} - \frac{y}{2R} \\ + \frac{4H}{\mu_0\Omega_K} \varepsilon \mu_q (\mu_0 C_p)^{1/2} \gamma_{dyn}^{1/2} \alpha_{ss}^{1/20} M^{7/16} R^{-85/16} (\Sigma\nu)^{17/40} \\ + \frac{12HB_R^2}{\alpha_{ss}\mu_0\Omega_K} \left(\frac{3}{2} - \left(\frac{R}{R_c}\right)^{3/2}\right) \end{aligned} \tag{2.3.11}$$

Further introducing the necessary relations we can re write this as

$$y' = \frac{\dot{M}}{6\pi R} - \frac{y}{2R} + 2\varepsilon\mu_q \left(\frac{3\gamma_{dyn}}{\mu_0\sqrt{GM}}\right)^{1/2} (Hy)^{1/2} R^{-13/4}$$
$$+\frac{12\mu_q^2}{\alpha_{ss}\mu_0\sqrt{GM}} \left(\frac{3}{2} - \left(\frac{R}{R_c}\right)^{3/2}\right) HR^{-13/2}\,. \qquad (2.3.12)$$

or

$$y' = \frac{\dot{M}}{6\pi R} - \frac{y}{2R}$$
$$+4\varepsilon\mu_q \left(\frac{\gamma_{dyn}C_p}{\mu_0 G}\right)^{1/2} \alpha_{ss}^{1/20} M^{-1/16} HR^{-61/16} (\Sigma\nu)^{17/40}$$
$$+\frac{12\mu_q^2}{\alpha_{ss}\mu_0\sqrt{GM}} \left(\frac{3}{2} - \left(\frac{R}{R_c}\right)^{3/2}\right) HR^{-13/2} \qquad (2.3.13)$$

If we introduce a dimensionless variable Λ through $y = \Lambda\dot{M}$, and another dimensionless radial coordinate r through $R = rR_M$, where R_M is the Magnetospheric radius, the ODE takes the form:

$$\frac{d\Lambda}{dr} = \frac{1}{6\pi r} - \frac{\Lambda}{2r} + 2\varepsilon\mu_q \left(\frac{3\gamma_{dyn}}{\mu_0\sqrt{GM}\dot{M}}\right)^{1/2} R_{in}^{-9/4} (H\Lambda)^{1/2} r^{-13/4}$$
$$+\frac{12\mu_q^2}{\alpha_{ss}\mu_0\sqrt{GM}\dot{M}} R_M^{-11/2} Hr^{-13/2} \left(\frac{3}{2} - \omega_s r^{3/2}\right), \qquad (2.3.14)$$

or

$$\begin{aligned}\frac{d\Lambda}{dr} &= \frac{1}{6\pi r} - \frac{\Lambda}{2r} \\ &+4\varepsilon\mu_q \left(\frac{\gamma_{dyn} C_p}{\mu_0 G}\right)^{1/2} \alpha_{ss}^{1/20} M^{-1/16} R_M^{-45/16} \dot{M}^{-23/40} H r^{-61/16} \Lambda^{17/40} \\ &+\frac{12\mu_q^2 R_M^{-11/2}}{\alpha_{ss}\mu_0\sqrt{GM}\dot{M}} H r^{-13/2} \left(\frac{3}{2} - \omega_s r^{3/2}\right). \end{aligned} \tag{2.3.15}$$

respectively. ω_s is the fastness parameter defined by

$$\omega_s = \left(\frac{R_{in}}{R_{co}}\right)^{3/2}, \tag{2.3.16}$$

and

$$R_M = \left(\frac{2\pi^2\mu_q^2}{GM\dot{M}^2\mu_0^2}\right)^{1/11} = 5.3\times 10^5 \dot{M}_{13}^{-2/11} M_1^{-1/11} \mu_{q24}^{4/11}. \tag{2.3.17}$$

We can now rewrite the ODE in its final form as The final version of our ODE can be of the form

$$\frac{d\Lambda}{dr} = \frac{1}{6\pi r} - \frac{\Lambda}{2r} + C_1 (H\Lambda)^{1/2} r^{-13/4} + C_2 H r^{-13/2} \left(\frac{3}{2} - \omega_s r^{3/2}\right), \tag{2.3.18}$$

where $C_1 = 2\varepsilon\mu_q \left(\frac{3\gamma_{dyn}}{\mu_0\sqrt{GM}\dot{M}}\right)^{1/2} R_{in}^{-9/4}$ and $C_2 = \frac{12\mu_q^2}{\alpha_{ss}\mu_0\sqrt{GM}\dot{M}} R_{in}^{-11/2}$ or

$$\frac{d\Lambda}{dr} = \frac{1}{6\pi r} - \frac{\Lambda}{2r} + C_1 H r^{-61/16} \Lambda^{17/40} + C_2 \left(\frac{3}{2} - \omega_s r^{3/2}\right) H r^{-13/2}. \tag{2.3.19}$$

where $C_1 = 2\varepsilon\mu_q \left(\frac{\gamma_{dyn} C_p}{\mu_0 G}\right)^{1/2} \alpha_{ss}^{1/20} M^{-1/16} R_M^{-45/16} \dot{M}^{-23/40}$ and $C_2 = \frac{12\mu_q^2 R_M^{-11/2}}{\alpha_{ss}\mu_0\sqrt{GM}\dot{M}}$

We can further transform our equation by defining the unit less parameter ξ as $r = 1/\xi$, and rewrite respectively as

$$\frac{d\Lambda}{d\xi} = -\frac{1}{6\pi\xi} - \frac{\Lambda}{2\xi} - C_1 H^{1/2} \Lambda^{1/2} \xi^{5/4} - C_2 H \left(\frac{3}{2} - \omega_s \xi^{-3/2} \right) \xi^{9/2}, \tag{2.3.20}$$

where $C_1 = 2\varepsilon\mu_q \left(\frac{3\gamma_{dyn}}{\mu_0 \sqrt{GM}\dot{M}} \right)^{1/2} R_{in}^{-9/4}$ and $C_2 = \frac{12\mu_q^2}{\alpha_{ss}\mu_0\sqrt{GM}\dot{M}} R_M^{-11/2}$ or

$$\frac{d\Lambda}{d\xi} = -\frac{1}{6\pi\xi} + \frac{\Lambda}{2\xi} - C_1 H \Lambda^{17/40} \xi^{19/16} - C_2 H \left(\frac{3}{2} - \omega_s \xi^{-3/2} \right) \xi^{9/2}, \tag{2.3.21}$$

where $C_1 = 2\varepsilon\mu_q \left(\frac{\gamma_{dyn} C_p}{\mu_0 G} \right)^{1/2} \alpha_{ss}^{1/20} M^{-1/16} R_M^{-45/16} \dot{M}^{-23/40}$ and $C_2 = \frac{12\mu_q^2 R_M^{-11/2}}{\alpha_{ss}\mu_0\sqrt{GM}\dot{M}}$

2.4 Result and Discussion

2.4.1 The Quadrupolar Magnetospheric Region

There can be accretion when the corotation radius is greater than the inner radius of the disk. Figure 2.1 shows the relation between inner radius, assumed to coincide approximately with magnetospheric radius although there is deviation in real cases. As a particular case of interest we take NS of mass 1.4 solar mass ($M_{\odot}$), stellar radius of about 10 km and surface magnetic field of 10^8 T. To determine the Magnetospheric radius we can consider total energy as a limit so that we take the double of kinetic energy. Therefore we can calculate a lower limit for the truncation radius equating the ram pressure to the magnetic

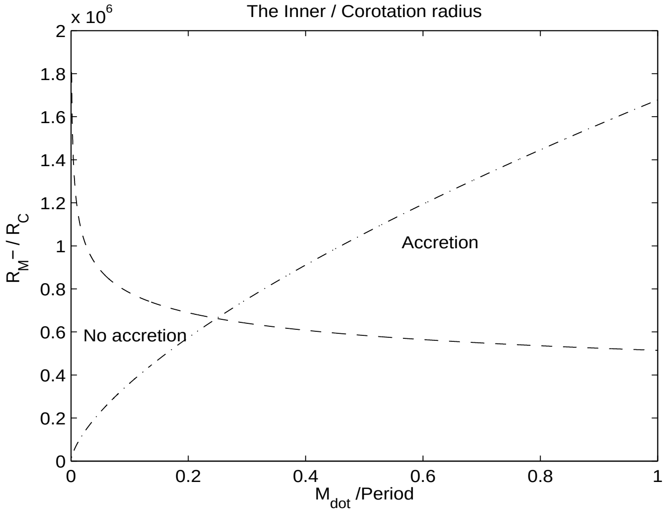

Figure 2.1: The Variation of Magnetospheric radius of an accretion disk around magnetic star with accretion rate in units of $\dot{M}_{13}$ shown by dash dot line and (Corotation radius of an accretion disk around magnetic star with period in units of seconds shown in dashed line)

pressure as (see Frank, King, and Raine 2002)

$$R_M = \left(\frac{2\pi^2 \mu^2}{GM\dot{M}^2 \mu_0^2} \right)^{1/11} = 5.3 \times 10^5 \dot{M}_{13}^{-2/11} M_1^{-1/11} \mu_{q24}^{4/11}, \tag{2.4.1}$$

We can also calculate an upper limit for the truncation radius equating the ram pressure to the magnetic pressure - Alfvén radius- as (see Shapiro & Teukolsy 1983)

$$R_A = \left(\frac{16\pi^2 \mu^2}{2GM\dot{M}^2 \mu_0^2} \right)^{1/11} = 6.01 \times 10^5 \dot{M}_{13}^{-2/11} M_1^{-1/11} \mu_{q24}^{4/11} m, \tag{2.4.2}$$

Based on this we can assume that, the inner radius of an accretion disk to be at the magnetospheric radius (MR) as a lower limit and Alfvén radius (AR) as its upper limit. The

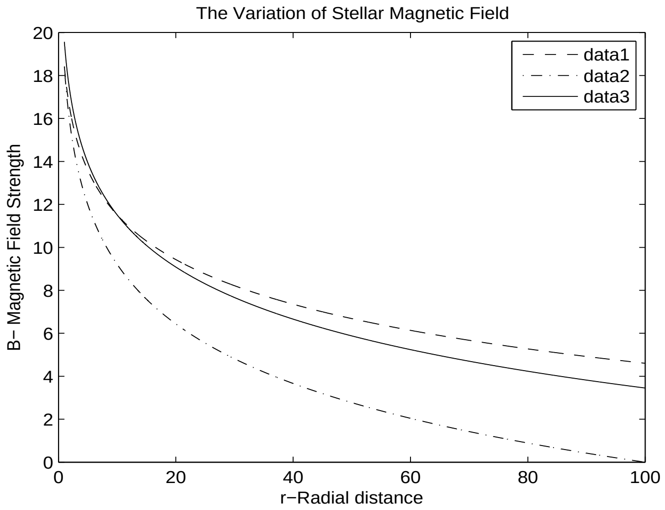

Figure 2.2: The Variation of Stellar Magnetic field components B with r. Data1 indicates the dipole field, data2 the quadrupole field and data3 the combined field.

structure of thin accretion disk in dipolar field was calculated by Tessema and Torkelsson (2010). Their results also agree with the fact that the lower limit for inner radius is Magnetospheric radius. It is expected that stellar magnetic field has a combined multipolar nature, where the dominant components are dipole and quadrupole components. Figure 2.2 shows that there is slight deviation from the combined field in both cases when the field is treated as only dipolar or quadrupolar. It is clear that the real field of the star is combined field. However, quadrupole field gives us an opportunity to see the effects magnetic field of comparable magnitude on an accretion disk at relatively nearer distance to the central star.

In our case the MR for quadrupole and dipole fields, we calculated that it is about 510 km and 5,600 km respectively. Also we have calculated the respective values of AR to be 580 km and 6,800 km. We assume this region of an accretion disk, between MR and AR to be the most probable region of truncation if magnetic effects on accretion are taken into account. Based on the results obtained we make final comments on this in section 4.4.

2.4.2 Analytic Solution - disk structure equations

The physical structure of an accretion disk can be found analytically by solving the magnetohydrodaynamic equations derived in the above sections. For convenience we divide the disk into an outer region with gas pressure and freefree opacity, a middle region with gas pressure and electron scattering opacity, and an inner region with radiation pressure and electron scattering. The total pressure is the sum of gas pressure, radiation pressure and magnetic pressure. We assume the gas pressure is dominant in most cases (see Shapiro 1983), and thus we can find structure equations describing thin Keplerian- disk based on this in the following section/as given below.

Height of an Accretion Disk

$$H = \frac{1}{\Omega_K}\left(\frac{K_B T_c}{\bar{\mu} m_p}\right)^{\frac{1}{2}} = \left(\frac{K_B}{m_p G}\right)^{\frac{1}{2}} \bar{\mu}^{-1/2} M^{-1/2} T_c^{1/2} R^{3/2} \,. \qquad (2.4.3)$$

or

$$H=\left(\frac{K_B}{m_pG}\right)^{\frac{1}{2}}\bar{\mu}^{-1/2}M^{-1/2}T_c^{1/2}R^{3/2}\,. \tag{2.4.4}$$

Solving for density we get

$$\rho=\frac{1}{\Omega_K}\frac{3\Sigma\nu}{4H^3\alpha_{ss}}=\frac{3}{4}\left(\frac{m_p}{K_B}\right)^{3/2}G\alpha_{ss}^{-1}\Sigma\nu\bar{\mu}^{3/2}MR^{-3}T_c^{-3/2}, \tag{2.4.5}$$

$$\rho=\frac{3}{4}\left(\frac{m_p}{K_B}\right)^{3/2}G\alpha_{ss}^{-1}\Sigma\nu\bar{\mu}^{3/2}MR^{-3}T_c^{-3/2}\,. \tag{2.4.6}$$

The gas pressure is then similarly given by

$$P_g=\left(\frac{K_B}{m_p}\right)\bar{\mu}^{-1}\rho T_c=\frac{3}{4}\alpha_{ss}^{-1}\left(\frac{m_p\bar{\mu}}{K_B}\right)^{1/2}\Sigma\nu GMR^{-3}T_c^{-1/2}, \tag{2.4.7}$$

$$P_g=\frac{3}{4}\alpha_{ss}^{-1}\left(\frac{m_p\bar{\mu}}{K_B}\right)^{1/2}\Sigma\nu GMR^{-3}T_c^{-1/2}, \tag{2.4.8}$$

Since

$$\rho H=\frac{3}{4}G^{1/2}\left(\frac{m_p}{K_B}\right)\alpha_{ss}^{-1}\Sigma\nu\bar{\mu}T_c^{-1}M^{1/2}R^{-3/2}, \tag{2.4.9}$$

the optical depth of the disk (central opacity) is given by

$$\begin{aligned}\tau_c&=\rho_cH(\kappa_K+\kappa_{es})\\&=\frac{3}{4}G^{1/2}\left(\frac{m_p}{K_B}\right)(\kappa_K+\kappa_{es})\alpha_{ss}^{-1}\Sigma\nu\bar{\mu}T_c^{-1}M^{1/2}R^{-3/2},\end{aligned} \tag{2.4.10}$$

Temperature of the disk (for combined opacity approach) is

$$T_c=\left[\frac{27}{32\sigma}\Sigma\nu\tau_c\Omega_K^2\right]^{1/4}=\left[\frac{27}{32\sigma}\Sigma\nu\rho_cH(\kappa_K+\kappa_{es})\Omega_K^2\right]^{1/4}, \tag{2.4.11}$$

$$T_c^5 = \left[\frac{81}{128\sigma} G^{3/2} \left(\frac{m_p}{K_B} \right) (\kappa_K + \kappa_{es}) (\Sigma\nu)^2 \alpha_{ss}^{-1} \bar{\mu} M^{3/2} R^{-9/2} \right], \tag{2.4.12}$$

$$T_c = C_1 (\kappa_K + \kappa_{es})^{1/5} \alpha_{ss}^{-1/5} (\Sigma\nu)^{2/5} \bar{\mu}^{1/5} R^{-9/10} M^{3/10}, \tag{2.4.13}$$

where

$$C_1 = \left(\frac{81 m_p}{128\sigma K_B} \right)^{1/5} G^{3/10} \tag{2.4.14}$$

Then the plasma density for combined opacity is

$$\rho = C_{c1} (\kappa_K + \kappa_{es})^{-3/10} \alpha_{ss}^{-7/10} (\Sigma\nu)^{2/5} \bar{\mu}^{6/5} M^{11/20} R^{-33/10}, \tag{2.4.15}$$

where

$$C_{c1} = G^{11/20} \frac{3}{4} \left(\frac{81}{128\sigma} \right)^{-3/10} \left(\frac{m_p}{K_B} \right)^{6/5}, \tag{2.4.16}$$

The part of the disk inside the radius at which electron scattering opacity is dominant includes, the region in which the magnetic perturbation of the disk becomes strong. Then the plasma density for electron scattering opacity is

$$\rho = C_{e1} \alpha_{ss}^{-7/10} (\Sigma\nu)^{2/5} \bar{\mu}^{6/5} M^{11/20} R^{-33/10}, \tag{2.4.17}$$

where

$$C_{c1} = G^{11/20}\frac{3}{4}\left(\frac{81\kappa_{es}}{128\sigma}\right)^{-3/10}\left(\frac{m_p}{K_B}\right)^{6/5}, \tag{2.4.18}$$

$$\tau_{c,es} = \rho_c H\kappa_{es} = \frac{3}{4}G^{1/2}\left(\frac{m_p}{K_B}\right)\kappa_{es}\alpha_{ss}^{-1}\Sigma\nu\bar{\mu}T_c^{-1}M^{1/2}R^{-3/2}, \tag{2.4.19}$$

$$T_c^5 = \left[G^{3/2}\frac{81\kappa_{es}}{128\sigma}\left(\frac{m_p}{K_B}\right)(\Sigma\nu)^2\alpha_{ss}^{-1}\bar{\mu}M^{3/2}R^{-9/2}\right], \tag{2.4.20}$$

$$T_c = C_{e2}\alpha_{ss}^{-1/5}(\Sigma\nu)^{2/5}\bar{\mu}^{1/5}R^{-9/10}M^{3/10}, \tag{2.4.21}$$

where

$$C_{e2} = G^{3/10}\left(\frac{81\kappa_{es}m_p}{128\sigma K_B}\right)^{1/5}, \tag{2.4.22}$$

The scale height for this case is

$$H = C_{e3}\alpha_{ss}^{-1/10}(\Sigma\nu)^{1/5}\bar{\mu}^{-2/5}M^{-7/20}R^{21/20}, \tag{2.4.23}$$

where

$$C_{e3} = G^{-7/20}\left(\frac{81\kappa_{es}}{128\sigma}\right)^{1/10}\left(\frac{K_B}{m_p}\right)^{\frac{2}{5}}, \tag{2.4.24}$$

and

$$P_g = C_{e4}\alpha_{ss}^{-9/10} G^{17/20} M^{17/20} (\Sigma\nu)^{4/5} R^{-51/20}, \tag{2.4.25}$$

$$C_{e4} = \frac{3}{4}\left(\frac{81\kappa_{es}}{128\sigma}\right)^{-1/10}\left(\frac{m_p\bar{\mu}}{K_B}\right)^{2/5}, \tag{2.4.26}$$

For gas pressure and electron scattering opacity, when electron scattering is dominant the scale height is

$$H = \left(\frac{81\kappa_{es}}{128\sigma\alpha_{ss}}\right)^{1/10}\left(\frac{K_B}{m_p\bar{\mu}}\right)^{\frac{2}{5}}\left(\frac{GM}{R^3}\right)^{\frac{-7}{20}}(\Sigma\nu)^{1/5} \tag{2.4.27}$$

$$B_{\phi,dyn} = C_{d1}\varepsilon(\mu_0\gamma_{dyn})^{1/2}(GM)^{17/40}R^{-51/40},, \tag{2.4.28}$$

where

$$C_{d1} = \left(\frac{3}{4}\right)^{1/2}\left(\frac{81\kappa_{es}}{128\sigma\alpha_{ss}}\right)^{-1/20}\left(\frac{K_B}{m_p\bar{\mu}}\right)^{-1/5}, \tag{2.4.29}$$

When the Kramer’s opacity is greater than electron scattering ($\kappa_K >> \kappa_{es}$):

The optical depth for Kramer’s opacity is

$$\tau_{c,K} = \frac{9}{16}G^{3/2}\left(\frac{m_p}{K_B}\right)^{5/2}\kappa_0\alpha_{ss}^{-2}(\Sigma\nu)^2\bar{\mu}^{5/2}T_c^{-6}M^{3/2}R^{-9/2}, \tag{2.4.30}$$

and

$$\tau_c = 2.28 \times 10^4 \alpha_{SS}^{-4/5} \bar{\mu} \dot{M}_{13}^{1/5} \Lambda^{1/5}, \tag{2.4.31}$$

(i.e., The optical depth of quadrupolar accretion is independent of radial distance R, mass of the NS, and the magnetic moment of the NS).

Temperature of an Accretion Disk

$$T_c = C_{t2} \alpha_{ss}^{-1/5} \bar{\mu}^{1/4} M^{1/4} (\Sigma\nu)^{3/10} R^{-3/4}, \tag{2.4.32}$$

where

$$C_{t2} = \left(\frac{243\kappa_0}{512\sigma}\right)^{1/10} \left(\frac{Gm_p}{K_B}\right)^{1/4} \tag{2.4.33}$$

and

$$T_c = 2.63 \times 10^6 \alpha_{SS}^{-1/5} \bar{\mu}^{-1/4} \dot{M}_{13}^{24/55} M_1^{14/44} \mu_{q24}^{-3/11} \Lambda^{3/10} r^{-3/4}, \tag{2.4.34}$$

Density of an Accretion Disk

$$\rho = C_{d2} \alpha_{ss}^{-7/10} (\Sigma\nu)^{11/20} \bar{\mu}^{9/8} M^{5/8} R^{-15/8}, \tag{2.4.35}$$

where

$$C_{d2} = \frac{3}{4} \left(\frac{243\kappa_0}{512\sigma}\right)^{-3/20} G^{5/8} \left(\frac{m_p}{K_B}\right)^{9/8}, \tag{2.4.36}$$

and

$$\rho = 1.570843 \alpha_{SS}^{-7/10} \bar{\mu}^{9/8} \dot{M}_{13}^{49/55} M_1^{35/44} \mu_{q24}^{-15/22} \Lambda^{11/20} r^{-15/8}, \tag{2.4.37}$$

Height of an Accretion Disk

$$H = C_{h2}\alpha_{ss}^{-1/10}\bar{\mu}^{-3/8}(\Sigma\nu)^{3/20}M^{-3/8}R^{9/8}, \tag{2.4.38}$$

where

$$C_{h2} = \left(\frac{243\kappa_0}{512\sigma}\right)^{1/20}\left(\frac{K_B}{m_p G}\right)^{\frac{3}{8}}, \tag{2.4.39}$$

and

$$H = 4.73993\times 10^3\alpha_{SS}^{-1/10}\bar{\mu}^{-3/8}\dot{M}_{13}^{-3/55}M_1^{-21/44}\mu_{q24}^{9/22}\Lambda^{3/20}r^{9/8}, \tag{2.4.40}$$

Aspect ratio of an Accretion Disk

$$\frac{H}{R} = 0.008934\alpha_{SS}^{-1/10}\bar{\mu}^{-3/8}\dot{M}_{13}^{7/55}M_1^{-17/44}\mu_{q24}^{1/22}\Lambda^{3/20}r^{1/8}, \tag{2.4.41}$$

This also shows that the disk proposed here is thinner than the standard disks of $H/R \sim 0.05$(see e.g. Frank, King & Raine 2002)

Surface Density of the Accretion Disk

$$\Sigma = C_{\Sigma 1}\alpha_{ss}^{-4/5}(\Sigma\nu)^{7/10}\bar{\mu}^{3/4}M^{1/4}R^{-3/4}, \tag{2.4.42}$$

where

$$C_{\Sigma 1} = \frac{3}{2}G^{1/4}\left(\frac{243\kappa_0}{512\sigma}\right)^{-1/10}\left(\frac{m_p}{K_B}\right)^{3/4}, \tag{2.4.43}$$

and

$$\Sigma = 1.4891373\times 10^4\alpha_{SS}^{-7/10}\bar{\mu}^{9/8}\dot{M}_{13}^{46/55}M_1^{7/22}\mu_{q24}^{-3/11}\Lambda^{7/10}r^{-3/4}, \tag{2.4.44}$$

This result shows that the surface density increases as the disk comes closer to the NS due to increased gravitational effect.

pressure of an accretion disk

$$P_g = C_{p4}\left(\frac{GM}{R^3}\right)^{7/8}\alpha_{ss}^{-9/10}(\Sigma\nu)^{17/20}, \tag{2.4.45}$$

where

$$C_{p4} = \frac{3}{4}\left(\frac{243\kappa_0}{512\sigma}\right)^{-1/20}\left(\frac{\bar{\mu}m_p}{K_B}\right)^{3/8}, \tag{2.4.46}$$

and

$$P = 0.003153\alpha_{ss}^{-9/10}\bar{\mu}^{-1/2}\dot{M}_{13}^{73/55}M_1^{49/44}\mu_{q24}^{-21/22}\Lambda^{17/20}r^{-21/8}, \tag{2.4.47}$$

The radial velocity of accretion

$$V_R = C_{\Sigma 2}\alpha_{ss}^{4/5}(\Sigma\nu)^{-7/10}\bar{\mu}^{-3/4}M^{-1/4}\dot{M}R^{-1/4}, \tag{2.4.48}$$

where

$$C_{\Sigma 2} = \frac{1}{3\pi}G^{-1/4}\left(\frac{243\kappa_0}{512\sigma}\right)^{1/10}\left(\frac{m_p}{K_B}\right)^{-3/4}, \tag{2.4.49}$$

and

$$V_R = 201.558\alpha_{SS}^{4/5}\bar{\mu}^{-3/4}\dot{M}_{13}^{19/55}M_1^{-5/22}\mu_{q24}^{1/11}\Lambda^{-7/10}r^{-1/4}, \tag{2.4.50}$$

For gas pressure and Kramer’s opacity, when Kramer’s opacity is dominant the scale height is

$$H = \left(\frac{243\kappa_0}{512\sigma}\right)^{1/20}\left(\frac{K_B R^3}{m_p\bar{\mu}GM}\right)^{\frac{3}{8}}\alpha_{ss}^{-1/10}(\Sigma\nu)^{3/20}, \tag{2.4.51}$$

The Dynamo component Magnetic Field

$$B_{\phi,dyn} = C_{m4}\varepsilon(\mu_0\gamma_{dyn})^{1/2}\left(\frac{GM}{R^3}\right)^{7/16}\alpha_{ss}^{1/20}(\Sigma\nu)^{17/40}, \tag{2.4.52}$$

where

$$C_{m4} = \left(\frac{3}{4}\right)^{1/2}\left(\frac{243\kappa_0}{512\sigma}\right)^{-1/40}\left(\frac{\bar{\mu}m_p}{K_B}\right)^{3/16}, \tag{2.4.53}$$

and

$$B_{\phi,dyn} = 0.05615\varepsilon\mu_0^{1/2}\bar{\mu}^{3/16}\alpha_{SS}^{1/20}\gamma_{dyn}^{1/2}\dot{M}_{13}^{73/110}M_1^{49/88}\mu_{q24}^{-21/44}\Lambda^{17/40}r^{-21/16} \tag{2.4.54}$$

The shear magnetic field component

$$B_{\phi,shear} = -3\alpha_{SS}^{-1}\mu_q R_{in}^{-4}r^{-4}\left(\frac{3}{2}-\omega_s r^{3/2}\right) \tag{2.4.55}$$

$$B_{\phi,shear} = -12.6515\alpha_{SS}^{-1}\bar{\mu}^{-1/4}\dot{M}_{13}^{8/11}M_1^{4/11}\mu_{q24}^{-5/11}\left(\frac{9}{2}-\omega_s r^{3/2}\right)r^{-4}, \tag{2.4.56}$$

Both dynamo and shear components of toroidal magnetic fields are relatively higher as compared to dipolar field. This may be due to the very nature of quadrupole field short range activity and the very position of quadrupolar disk to central star.

When the radiation pressure is dominant

$$H = \left(\frac{9\kappa_{es}}{8c}\right)(\Sigma\nu), \tag{2.4.57}$$

which is independent of R. In the region where the radiation pressure is dominant and this is due due to the electron scattering, the depth of the layer is very thin.

$$\rho = \frac{3}{4}\left(\frac{8c}{9\kappa_{es}}\right)^3\left(\frac{R^3}{GM}\right)^{1/2}\alpha_{ss}^{-1}(\Sigma\nu)^{-2}\,. \tag{2.4.58}$$

Temperature of an Accretion DisK

$$T_c = \left(\frac{81\kappa_{es}}{128\sigma}\right)^{1/4}\left(\frac{8c}{9\kappa_{es}}\right)^{1/2}\alpha_{ss}^{-1/4}(GM)^{1/8}R^{-3/8}, \tag{2.4.59}$$

and

$$T_c = 2.43\times 10^6\alpha_{SS}^{-1/5}\overline{\mu}^{-1/4}\dot{M}_{13}^{24/55}M_1^{14/44}\mu_{q24}^{-3/11}\Lambda^{3/10}r^{-3/4}, \tag{2.4.60}$$

The optical depth of Accretion Disk

$$\tau_c = 261.832\alpha_{SS}^{-4/5}\overline{\mu}\dot{M}_{13}^{1/5}\Lambda^{1/5}, \tag{2.4.61}$$

(i.e., The optical depth of quadrupolar (also dipolar) accretion is independent of radial distance, mass of the NS, and the magnetic moment of the NS).

2.4.3 Numerical Solutions

For our thin disk model, we take a neutron star of M = 1.4 $M_\odot$ and a magnetic moment of 10^{24} Tm^4, which is accreting at the rate 10^{13} kg s^{-1}. The dimensionless parameters γ and γ_{dyn} are, respectively, 1 and 10 in our model, while $\alpha_{ss} = 0.01$. We vary a parameter ε to find the solutions following the same approach as in Tessema & Torkelsson (2010).

For a thin Keplerian disk we get the solution of the density of an accretion disk shown in Figures 2.3 - 2.7, in which the density variation is clearly shown. In Figure 2.3 results corresponding to ε = 0.1, 0.05, and 0, from top to the bottom respectively are given. To get a good picture of this we can consider the point of maxima (peak) as a reference and take the left and right side of this plot for discussion.

The effect of the internal dynamo is to redistribute the central density according to $\rho_{\varepsilon=0.1} < \rho_{\varepsilon=0.05} < \rho_{\varepsilon=0}$ for the left side and $\rho_{\varepsilon=0} < \rho_{\varepsilon=0.05} < \rho_{\varepsilon=0.1}$ to the right of the peaks.

The disk inner radius seems to be located at the magnetospheric ($\sim R_M$) radius. Density assumes its lowest value near this boundary. On the other hand on the right panel of density plot (Fig. 2.3) it rather decreases outwards from the peak.

The solution of the disk central temperature is shown in Figures 2.8 - 2.10. In Figure 2.8 the temperature variation corresponding to ε = 0.1, 0.05, and 0, is shown from top to the

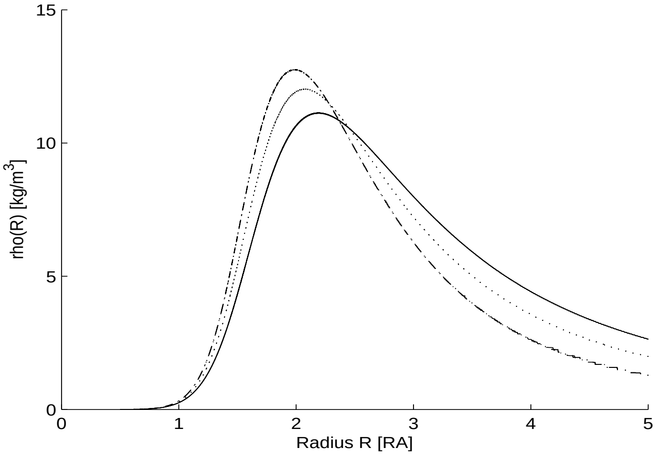

Figure 2.3: The Variation of density of an accretion disk around magnetic star with r, where the curves correspond to $\varepsilon = 0$,the dash dot line $\varepsilon = 0.05$,the solid line, and $\varepsilon = 0.1$,dashed line from top to the bottom respectively (i. e. taking peaks).

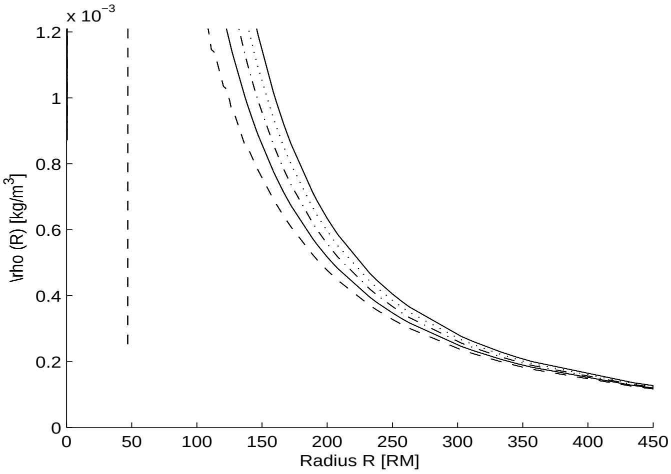

Figure 2.4: The Variation of density of an accretion disk around magnetic star with r, where the curves correspond to $\varepsilon = 0$,the dash dot line $\varepsilon = 0.05$,the solid line, and $\varepsilon = 0.1$,dashed line from top to the bottom respectively (i. e. taking peaks).

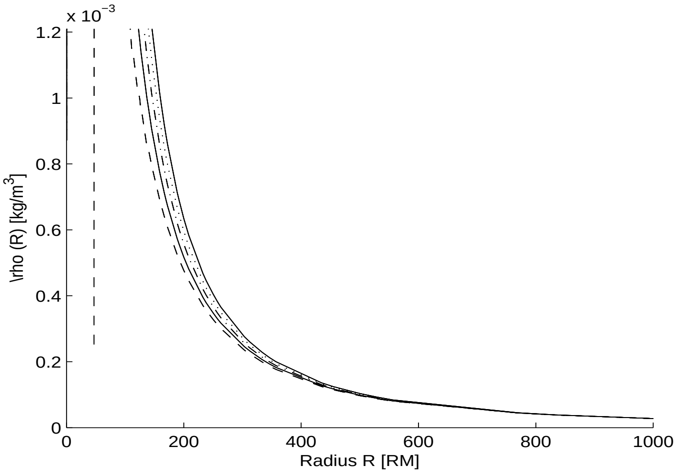

Figure 2.5: The Variation of density of an accretion disk around magnetic star with r, where the curves correspond to $\varepsilon = 0$,the dash dot line $\varepsilon = 0.05$,the solid line, and $\varepsilon = 0.1$,dashed line from top to the bottom respectively (i. e. taking peaks).

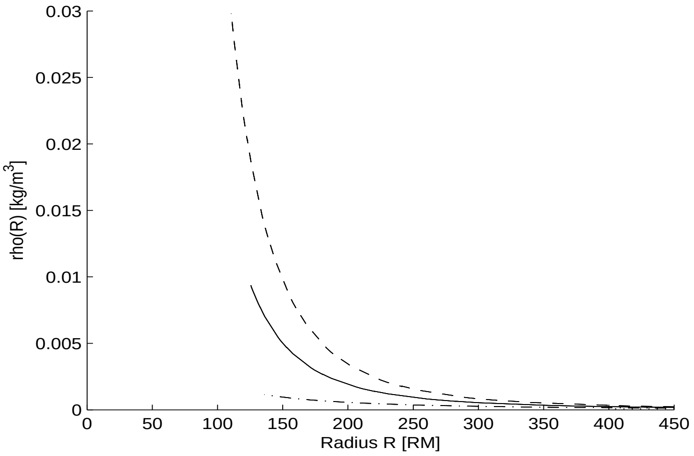

Figure 2.6: The Variation of density of an accretion disk around magnetic star with r, in the mid region of the disk where the curves correspond to $\varepsilon = 0.1$,dashed line, to $\varepsilon = 0.05$,the solid line,to $\varepsilon = 0$,the dash dot line.

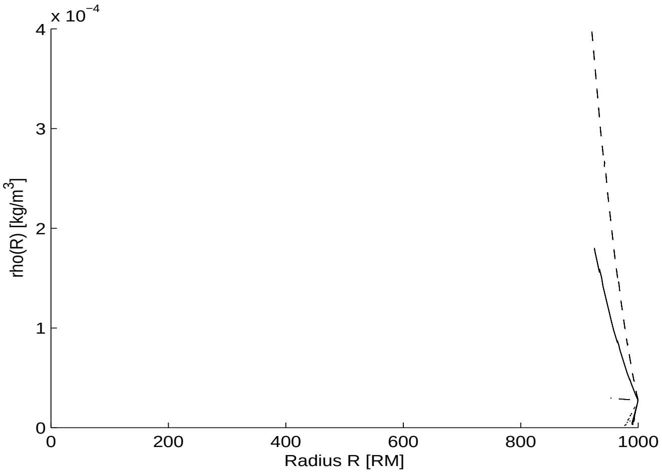

Figure 2.7: The Variation of density of an accretion disk around magnetic star with r, in the outer region where gas pressure and Kramer’s opacity is dominant - where the curves correspond to $\varepsilon = 0.1$,dashed line, to $\varepsilon = 0.05$,the solid line,to $\varepsilon = 0$,the dash dot line.

bottom respectively. At the inner boundary the value of temperature is of the order of 10^7 K (2.1×10^7 K). Here no significant effect of dynamo component is observed for r$\leq$ R_A. This continues to be the case for r>> R_A. However, the dynamo effect is clearly observed in the middle region beyond R_A. On the other hand the radiation pressure near the inner radius is high, corresponding to the maximum value of temperature as shown in Fig. 2.8. However, the magnetic pressure can increase and support the disk in the vertical direction, since magnetic heating can balance such radiative cooling.(e.g. Oda et al. (2012))

The solution showing the variation of Lambda of an accretion disk, is shown in successive Figures 2.11 - 2.20. In Figure 2.11, the left side plot corresponds to the region

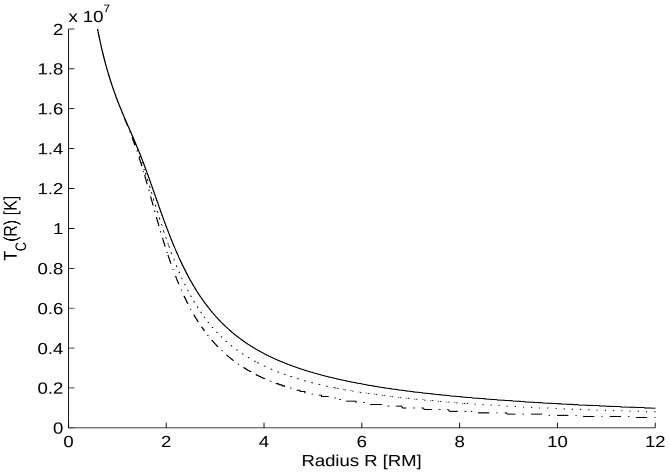

Figure 2.8: The Variation of central temperature of an accretion disk around magnetic star with r, in the mid region of the disk where the curves correspond to $\varepsilon = 0.1$,dashed line, to $\varepsilon = 0.05$,the solid line,to $\varepsilon = 0$,the dash dot line.

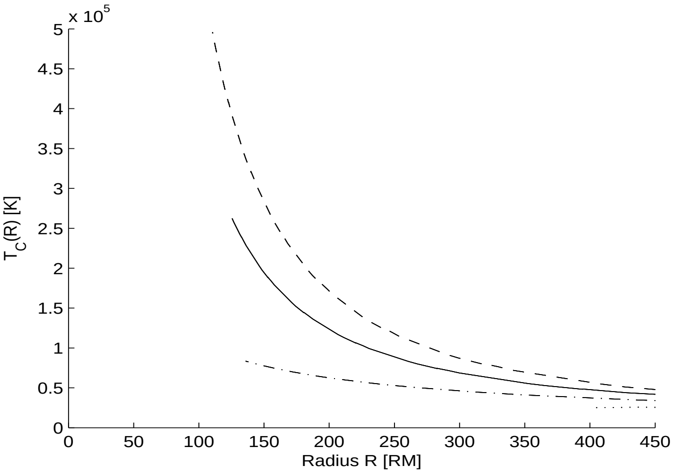

Figure 2.9: The Variation of central temperature of an accretion disk around magnetic star with r, in the mid region of the disk where the curves correspond to $\varepsilon = 0.1$,dashed line, to $\varepsilon = 0.05$,the solid line,to $\varepsilon = 0$,the dash dot line.

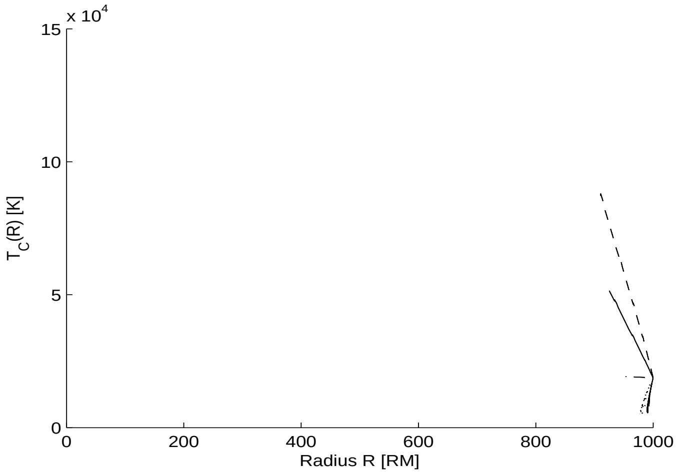

Figure 2.10: The Variation of central temperature of an accretion disk around magnetic star with r, in the outer region where gas pressure and Kramer's opacity is dominant - where the curves correspond to $\varepsilon = 0.1$,dashed line, to $\varepsilon = 0.05$,the solid line,to $\varepsilon = 0$,the dash dot line.

around the inner radius for positive values of ε = 0.1, 0.05, and 0, from top to the bottom respectively. The value of Lambda at the inner radius is the maximum possible and it is of the order of$\sim$ 1600 as shown in Figure 2.12. This may be basically due to the MRI that is expected to be a source of effective viscosity, since molecular viscosity is almost the same everywhere.

In absence of the internal dynamo the value of Lambda approaches the Shakura-Sunyaev value very rapidly. The contribution of the internal dynamo at the inner boundary is not significant. Rather the interaction of magnetosphere with the shear component field is responsible for this as it is dominant here. The fact that density is low at the boundary is also

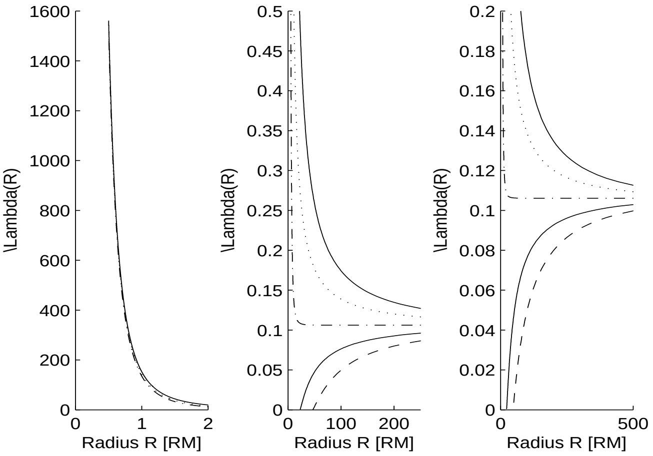

Figure 2.11: The combined plot for Variation of Lambda of an accretion disk around magnetic star with r,where the top, dashed curve corresponds to ε = 0.1, 0.05 and 0,the middle, solid curve corresponds to ε = 0.05 and the lower, dashdot curve corresponds to ε = 0,the dotted curve corresponds to ε = - 0.05 and the solid curve corresponds to ε = - 0.1

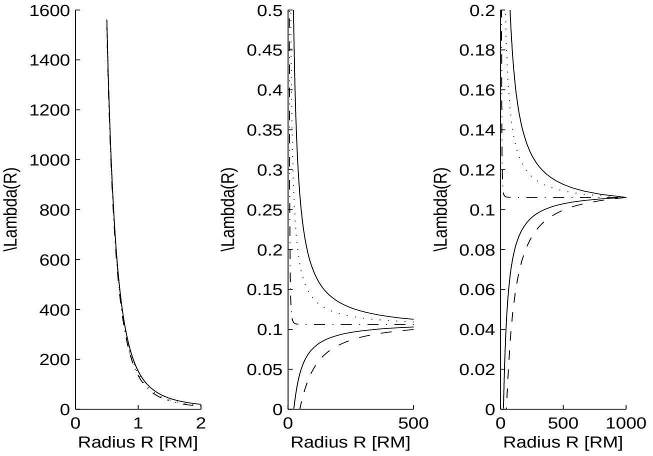

Figure 2.12: The combined plot for Variation of Lambda of an accretion disk around magnetic star with r,where the top, dashed curve corresponds to ε = 0.1, 0.05 and 0,the middle, solid curve corresponds to ε = 0.05 and the lower, dashdot curve corresponds to ε = 0,the dotted curve corresponds to ε = - 0.05 and the solid curve corresponds to ε = - 0.1

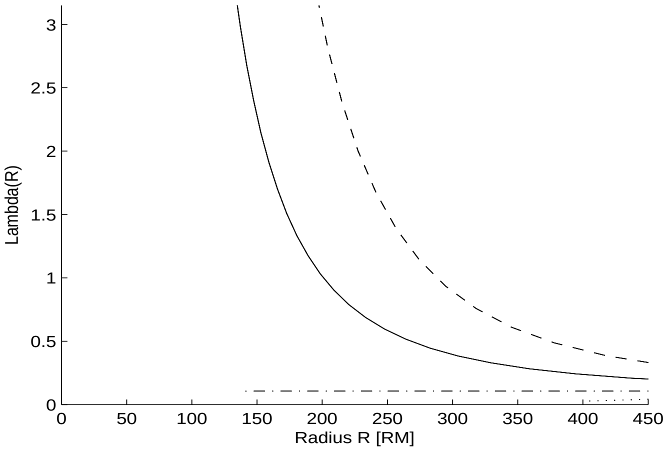

Figure 2.13: The Variation of Lambda of an accretion disk around magnetic star with r, in the mid region of the disk where the curves correspond to $\varepsilon = 0.1$,dashed line, to $\varepsilon = 0.05$,the solid line,to $\varepsilon = 0$,the dash dot line.

due to the the interaction we have between star magnetosphere rotating with star's spin to Keplerian disk. From the middle plot it can be clearly seen that it is enough to consider the positive values of ε due to the symmetric nature of dynamo contribution results. The effect of the internal dynamo is clearly observed for the middle part of the disk as shown in Fig. 2.19 & 2.20. However, near the outer radius the value of Lambda deviation due to the internal dynamo becomes negligible so that Lambda approaches the Shakura-Sunyaev value. This is in a good agreement with the results obtained by Gosh and Lamb (Gosh & Lamb) for thin accretion disks.

The results from density, temperature and Lambda plots also show that the inner radius

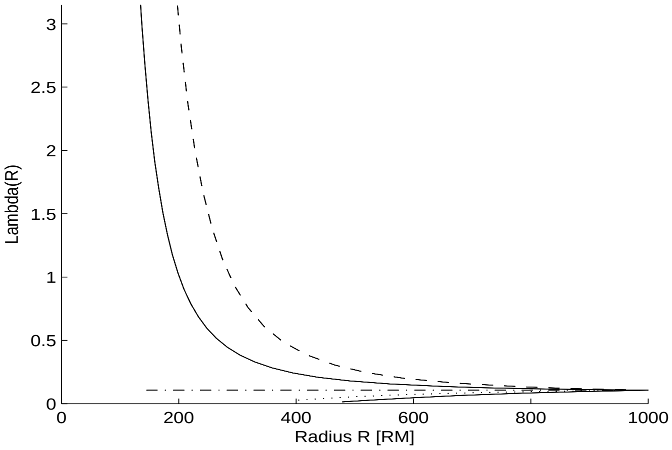

Figure 2.14: The Variation of Lambda of an accretion disk around magnetic star with r, in the mid region of the disk where the curves correspond to $\varepsilon = 0.1$,dashed line, to $\varepsilon = 0.05$,the solid line,to $\varepsilon = 0$,the dash dot line.

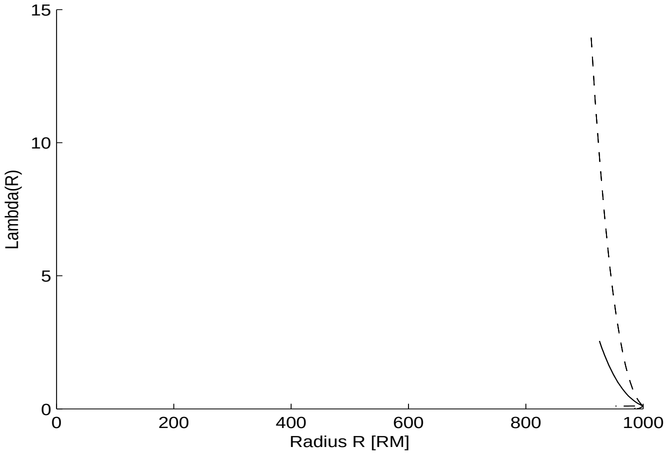

Figure 2.15: The Variation of Lambda of an accretion disk around magnetic star with r, in the outer region where gas pressure and Kramer's opacity is dominant - where the curves correspond to $\varepsilon = 0.1$,dashed line, to $\varepsilon = 0.05$,the solid line,to $\varepsilon = 0$,the dash dot line.

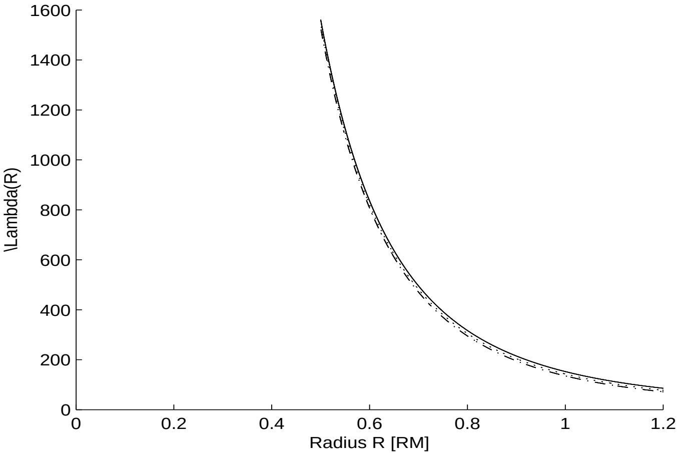

Figure 2.16: The Variation of Lambda of an accretion disk around magnetic star with r, in the mid region of the disk where the curves correspond to $\varepsilon = 0.1$,dashed line, to $\varepsilon = 0.05$,the solid line,to $\varepsilon = 0$,the dash dot line.

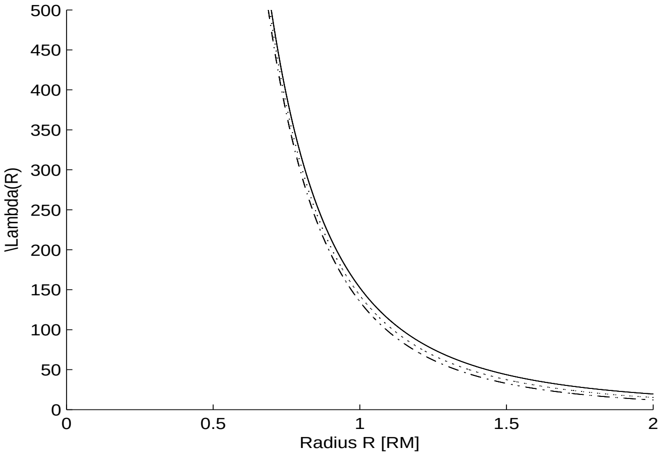

Figure 2.17: The Variation of Lambda of an accretion disk around magnetic star with r, in the mid region of the disk where the curves correspond to $\varepsilon = 0.1$,dashed line, to $\varepsilon = 0.05$,the solid line,to $\varepsilon = 0$,the dash dot line.

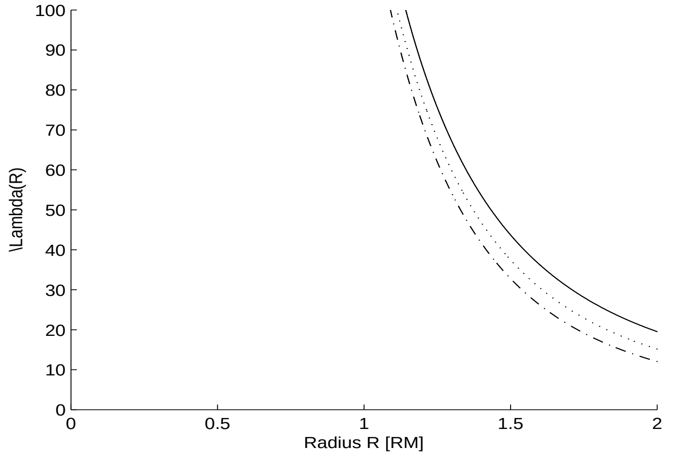

Figure 2.18: The Variation of Lambda of an accretion disk around magnetic star with r, in the mid region of the disk where the curves correspond to $\varepsilon = 0.1$,dashed line, to $\varepsilon = 0.05$,the solid line,to $\varepsilon = 0$,the dash dot line.

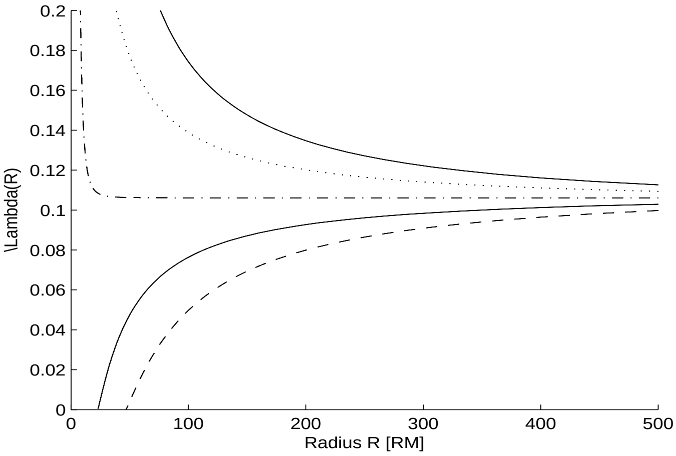

Figure 2.19: The Variation of Lambda of an accretion disk around magnetic star with r, in the mid region of the disk where the curves correspond to $\varepsilon = 0.1$,dashed line, to $\varepsilon = 0.05$,the solid line,to $\varepsilon = 0$,the dash dot line.

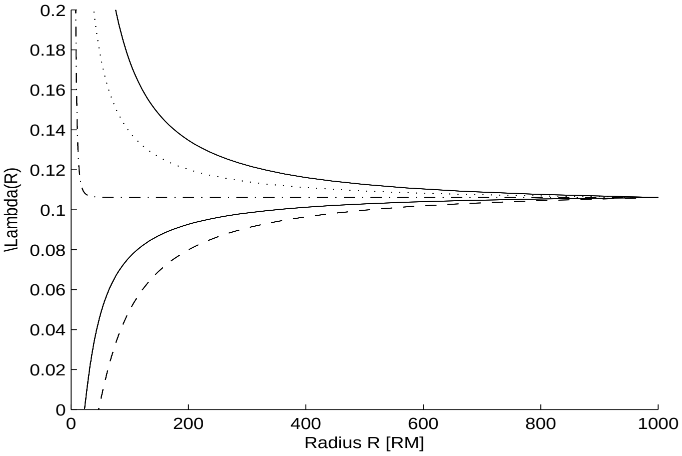

Figure 2.20: The Variation of Lambda of an accretion disk around magnetic star with r, in the mid region of the disk where the curves correspond to $\varepsilon = 0.1$,dashed line, to $\varepsilon = 0.05$,the solid line,to $\varepsilon = 0$,the dash dot line.

can extend beyond magnetospheric radius as assumed. This is true for the cases considered irrespective of the value of star's spin. At the boundary of inner radius, density of accretion disk plasma reduces to zero as can be seen from Figure 2.3.

Steady thin disk (α-disk) theory has only a fairly weak dependence on α. α is a dimensionless measure of the viscosity whose properties is still under investigation. Its size is directly proportional to the rate at which angular momentum is transported within the disk, and so is directly related to the time-scale on which the disk can evolve. To mention some figures for dwarf novae in cataclysmic variables (CVs) $\alpha \simeq$0.1-0.3 and $\alpha \simeq$0.2-0.4 soft X-ray transients (SXTs)-accreting NS binaries (King et al. (2007)).

The size of α (viscosity) is directly proportional to the rate at which angular momentum is transported within the disk, and so is directly related to the time-scale on which a disk can evolve. The approach we followed for disk solution in this model (sec. 2.3) is to magnify this weak dependence so that we can achieve better results. Magnetically Channeled Accretion onto the Central Star Since the work of Ghosh and Lamb (1978), workers in the field of X-ray binaries have concurred that if the central object is sufficiently strongly magnetized, the last stages of mass accretion from a surrounding disk may be channeled magnetically onto the central (neutron) star rather than continue to the stars surface by viscous inspiraling. Only in the case of YSOs, however, do we have direct spectroscopic evidence of this process in the shape of predicted line profiles

2.5 Conclusion

We can summarize the main results of our study on Keplerian-disk in this chapter as follows:

1. We have put the clear distinction between Magnetospheric and Alfvén radii which are commonly used in relation to the accretion process in section 2.4.1.

2. Using alpha prescription we are able to find self-similar Keplerian-disk structure solution, for different disk regions as given in sec. 2.4.2.

3. Our numerical solution in section 2.4.3 gives the variation of density, temperature and viscosity for Keplerian disk around magnetic star. The spectrum of emitted radiation is shown in TC plot (Fig. 2.8).

4. The quadrupole treatment makes this treatment special as it has enabled us to approach the central star more than dipolar field.

5. The inner disk radius is determined with better accuracy.

6. Our Lambda result shows relatively larger viscosity specially at the inner region of AD where the magnetic field is strong (e.g. Fig. 2.11).

7. Though it is difficult to determine detailed properties of α, here we have determined (its) viscosity radial dependence in AD.

Chapter 3

Accretion Disk around Magnetized Stars II - non-Keplerian Thin Disk

3.1 Introduction

In this chapter we consider thin accretion disk - geometrically thin and optically thick magnetohydrodynamical model to generalize the standard radiatively efficient disk around compact objects. If an accretion disk can be non-Keplerian, what is the possible origin? We will find out this first and then introduce non-Keplerian nature to investigate such disk throughout this chapter. In Sect. 1 we introduce the relevant MHD equations to derive a dimensionless function to solve the equation of angular momentum conservation. We employ the kinematic viscosity and solve the equation of angular momentum conservation for the rotation profile of a disk around a neutron star. In Sect. 3.2 we describe the inner part of an accretion disk in a quadrupolar field. In Sect. 3.3 we discuss the significance of the results obtained in this work. Finally we summarize our results in Sect. 3.4.

3.2 The Mathematical Description of non-Keplerian Thin disk

The structure of an accretion disk is determined by the basic equations of viscous fluid dynamics: the continuity equation, Navier-Stoke's equation and the equation of conservation of energy, to which we add the effect of the magnetic field through the Lorentz force. For a thin axisymmetric non-Keplerian accretion disk around neutron star having quadrupole fields, steady state equations in cylindrical coordinates (R, ϕ, z) can be summarized as shown below.

3.2.1 Conservation of Mass

The condition of mass conservation of fluid in a flow directly leads to continuity equation, and for steady, axisymmetric disk it is given by

$$\frac{1}{R}\frac{\partial}{\partial R}(\rho R V_R) + \frac{\partial}{\partial z}(\rho V_z) = 0 \tag{3.2.1}$$

where ρ is the density and $\mathbf{V}$ is the fluid velocity, with radial - V_R, azimuthal - V_ϕ and vertical - V_z components. Following the thin disk approximation we ignore the vertical velocity and integrate in the vertical direction across the disk, to obtain the mass accretion rate as

$$\dot{M} = -2\pi R\Sigma(R)V_R, \tag{3.2.2}$$

where Σ is the surface density defined by

$$\Sigma(R) = \int_{-H}^{H} \rho(R,z)dz = 2\rho(R)H, \tag{3.2.3}$$

where $\rho(R)$ denotes the vertically averaged density and H is the half-thickness of the disk.

3.2.2 Conservation of Momentum (Navier - Stoke's equation)

We make use of cylindrical coordinates (R,ϕ,z), and each of the three components of the Navier-Stokes equation define some important properties of accretion disk.

Vertical structure: hydrostatic equilibrium. Introducng axisymmetry and the vertical equilibrium condition, ($V_z = 0$) in the vertical component of Eq. (2.2.5) for a steady disk gives

$$\rho\left(\frac{\partial\psi}{\partial z}\right) = -\frac{\partial}{\partial z}\left(p + \frac{B_R^2 + B_\phi^2}{2\mu_0}\right) \tag{3.2.4}$$

For a weak magnetic field this further reduces to

$$\frac{1}{\rho}\left(\frac{\partial p}{\partial z}\right) = -\frac{GM}{R^2}\frac{z}{R}. \tag{3.2.5}$$

which may be rewritten as

$$\frac{c_s^2}{\rho}\frac{d\rho}{dz} = -\frac{GMz}{R^3}, \tag{3.2.6}$$

where c_s is the speed of sound, for which the density distribution is Gaussian if the disk is isothermal in the vertical direction. The pressure p is the sum of gas and radiation pressure,

$$P_g \propto T_c \quad : \quad P_{rad} \propto T_c^4 \tag{3.2.7}$$

where T_c is temperature in the central plane.

Hydrostatic equilibrium condition demands that

$$\frac{H}{R} = \frac{c_S}{V_K}, \tag{3.2.8}$$

where H is a vertical scale height. Eq. (3.2.8) demonstrates that the requirement the disk is thin is equivalent to that the disk rotation is highly supersonic.

Radial equilibrium: centrifugal balance. Ignoring the time dependence and with the previous assumption that the disk is axisymmetric, the radial component of Eq. (2.2.5) can be written as

$$\frac{\partial}{\partial R}\left(\frac{V_R^2}{2}\right) + V_z\frac{\partial V_R}{\partial z} + \left(\frac{\partial \psi}{\partial R}\right) - \frac{V_\phi^2}{R} + \frac{1}{\rho}\frac{\partial}{\partial R}\left(P + \frac{B_\phi^2}{\mu_0}\right) - \frac{1}{\rho}B_z J_\phi = 0 \tag{3.2.9}$$

where the toroidal current density, $J_\phi = \frac{1}{\mu_0}(\frac{\partial B_R}{\partial z} - \frac{\partial B_z}{\partial R})$. We used the magnetic pressure term to incorporate the Lorentz force in to the radial forces. An accretion disk kept in equilibrium by the balance between the gravitational acceleration, centrifugal acceleration and the pressure gradient fulfills the relation

$$\frac{V_\phi^2}{R} - \frac{1}{\rho}\frac{\partial}{\partial R}\left(P + \frac{B_\phi^2}{\mu_0}\right) - \left(\frac{\partial \psi}{\partial R}\right) = 0 \tag{3.2.10}$$

or

$$V_\phi^2 = R\left(\frac{\partial\psi}{\partial R}\right) + \frac{R}{\rho}\frac{\partial}{\partial R}\left(P + \frac{B_\phi^2}{\mu_0}\right) \tag{3.2.11}$$

where the first term on the right hand side (RHS) corresponds to the Keplerian velocity and the second represents the deviation from Keplerian rotation. When the deviation term is non-negligible the corresponding motion is said to be non-Keplerian. It is clear that both cases of super-Keplerian and sub-Keplerian velocity are there and this follows from the gradient term. This directly leads to the inclusion of the ± sign. We now introduce the sound speed equation,

$$\frac{1}{\rho}\left(\frac{\partial P}{\partial R}\right) = \frac{c_s^2}{\rho}\frac{\mathrm{d}\rho}{\mathrm{d}R} = \pm\frac{c_s^2}{R}, \tag{3.2.12}$$

which when used in the version of Eq. (3.2.11) for non-magnetic disk, delivers

$$V_\phi^2 = R\frac{\partial\psi}{\partial R} + c_s^2\frac{R}{\rho}\frac{\mathrm{d}\rho}{\mathrm{d}R} = V_K^2 + c_s^2\frac{R}{\rho}\frac{\mathrm{d}\rho}{\mathrm{d}R} = V_K^2 \pm c_s^2, \tag{3.2.13}$$

Since for thin disks $c_s \ll V_\phi$, this gives

$$\frac{V_\phi^2}{R} = \frac{\partial\psi}{\partial R}. \tag{3.2.14}$$

The gravitational potential of the central star, ψ in this case is expected to lead to Keplerian motion.

From a vertical integration of Eq. 3.2.4 we can get the radial equilibrium equation for the disk as

$$\frac{1}{2}\Omega_K^2 \Sigma H = \frac{B_\phi^2}{2\mu_0} + \frac{\rho K_B T_c}{\bar{\mu} m_p} + \frac{4\sigma T_c^4}{3c} \tag{3.2.15}$$

The right hand side of Eq. (3.2.15) is the total pressure (at the midplane) and we can rewrite the left hand side of the same equation as

$$P_{tot} = \rho \frac{GM}{R^3} H^2 = \frac{1}{2} H \Sigma \frac{GM}{R^3}\,. \tag{3.2.16}$$

Solving for H this gives

$$H = \frac{c_s}{\Omega_K} = \frac{1}{\Omega_R}\left(\frac{K_B T_c}{\bar{\mu} m_p} + \frac{4\sigma T_c^4}{3c\rho} + \frac{B_\phi^2}{2\mu_0 \rho}\right)^{\frac{1}{2}}\,. \tag{3.2.17}$$

So, combining the results from the vertical and radial equations, i.e. , Eqs. (3.2.13) & (3.2.6), we derive

$$\Omega^2 = \Omega_K^2 \left[1 \pm \left(\frac{H}{R}\right)^2 \frac{R}{\rho}\frac{\mathrm{d}\rho}{\mathrm{d}R}\right] = \Omega_K^2 \beta_K^2\,. \tag{3.2.18}$$

This shows that the motion is no more Keplerian.

We can include the effect of magnetic pressure by rewriting the above equation as

$$\Omega = \beta_K \Omega_K \tag{3.2.19}$$

where β_K is given by $\beta_K = \left[1 + \left(\frac{H}{R}\right)^2 \frac{R}{\rho}\frac{\mathrm{d}\rho}{\mathrm{d}R}\right]^{1/2} = \left[1 \pm \left(\frac{H}{R}\right)^2\right]^{1/2}$, is a measure of the deviation from the Keplerian motion. Since $\frac{R}{\rho}\frac{\mathrm{d}\rho}{\mathrm{d}R} \sim 1$, is of the order of unity, the positive sign represents super-Keplerian motion while the negative sign represents (i.e. being related to negative pressure gradient) sub-Keplerian rotation. Obviously this in the limit $H << R$, gives the disk rotation is Keplerian.

Angular momentum conservation: The vertically integrated form of the last component of Navier-Stokes equation, Eq. (2.2.5) becomes

$$\Sigma V_R \frac{\partial \ell}{\partial R} = 2H(R)\frac{\partial}{\partial R}\left(R^2 \frac{B_R B_\phi}{\mu_0}\right) + \frac{1}{R}\frac{\partial}{\partial R}\left(R^3 \nu \Sigma \frac{\partial}{\partial R}\left(\frac{\ell}{R^2}\right)\right), \tag{3.2.20}$$

where ℓ is an angular momentum.

3.3 The Governing Equations

If we define a function y related to the viscosity by

$$y = \nu\Sigma, \tag{3.3.1}$$

we can, using this definition, rewrite Eq. (3.2.20) as

$$y' = \frac{\dot{M}}{6\pi R} - \frac{y}{2R} + \frac{4H}{\Omega}\left(\frac{B_R B_\phi}{\mu_0}\right) \tag{3.3.2}$$

Inserting Eq. (2.2.33) into Eq. (2.2.44) will give

$$B_{\phi,dyn} = \varepsilon \left(\frac{3\mu_0 \gamma_{dyn} \Omega}{4H}\right)^{1/2} y^{1/2}, \tag{3.3.3}$$

or Inserting Eq. (3.4.35) into Eq. (2.2.44) will give

$$B_{\phi,dyn} = \varepsilon(\mu_0 C_p)^{1/2}\gamma_{dyn}^{1/2}\alpha_{ss}^{1/20}\beta_{K}^{2/5}M^{7/16}R^{-21/16}(\Sigma\nu)^{17/40}, \tag{3.3.4}$$

where

$$C_p = \frac{3}{4}G^{7/8}\left(\frac{243\kappa_0}{512\sigma}\right)^{-1/20}\left(\frac{\bar{\mu}m_p}{K_B}\right)^{3/8}, \tag{3.3.5}$$

On the other hand Eq. (2.2.41), can be rewritten as

$$B_{\phi,shear} = \frac{3B_R}{\alpha_{ss}}\left(\frac{3}{2}\beta_K - \left(\frac{R}{R_c}\right)^{3/2}\right), \tag{3.3.6}$$

and R_c is the corotation radius at which the disk angular velocity equals the stellar angular velocity. It is defined by

$$R_c = \left(\frac{GM}{\Omega_S^2}\right)^{1/3} = 1.5\times 10^6 M_1 P_{spin}^{2/3} m \tag{3.3.7}$$

where P_{spin} is the spin period and $M_1 = \frac{M}{M_\odot}$.

Substituting Eq. (3.3.3) and Eq. (3.3.6) into Eq. (2.2.45) gives

$$B_R B_\phi = B_R\varepsilon\left(\frac{3\mu_0\gamma_{dyn}\Omega}{4H}\right)^{1/2} y^{1/2} + \frac{3B_R^2}{\alpha_{ss}}\left(\frac{3}{2}\beta_K - \left(\frac{R}{R_c}\right)^{3/2}\right), \tag{3.3.8}$$

which when inserted in to Eq. (3.3.2) delivers

$$\begin{aligned} y' = \frac{\dot{M}}{6\pi R} - \frac{y}{2R} + 2\varepsilon B_R\left(\frac{3\gamma_{dyn}}{\mu_0\Omega_K}\right)^{1/2}\left(\frac{Hy}{\beta_K}\right)^{1/2} \\ + \frac{12HB_R^2}{\alpha_{ss}\mu_0\Omega_K}\left(\frac{3}{2} - \frac{1}{\beta_K}\left(\frac{R}{R_c}\right)^{3/2}\right). \end{aligned} \tag{3.3.9}$$

or

Substituting Eq. (3.3.4) and Eq. (3.3.6) into Eq. (2.2.45) gives

$$\begin{aligned} B_R B_\phi = {} & \varepsilon(\mu_0 C_p)^{1/2}\gamma_{dyn}^{1/2}\alpha_{ss}^{1/20}\beta_K^{2/5}M^{7/16}R^{-21/16}(\Sigma\nu)^{17/40}B_R \\ & + \frac{3B_R^2}{\alpha_{ss}}\left(\frac{3}{2}\beta_K - \left(\frac{R}{R_c}\right)^{3/2}\right) \end{aligned} \tag{3.3.10}$$

which when inserted in to Eq. (3.3.2) delivers

$$\begin{aligned} y' = {} & \frac{\dot{M}}{6\pi R} - \frac{y}{2R} \\ & + \frac{4H}{\mu_0\beta_K\Omega_K}\varepsilon\mu_q(\mu_0 C_p)^{1/2}\gamma_{dyn}^{1/2}\alpha_{ss}^{1/20}\beta_K^{2/5}M^{7/16}R^{-85/16}(\Sigma\nu)^{17/40} \\ & + \frac{12HB_R^2}{\alpha_{ss}\mu_0\beta_K\Omega_K}\left(\frac{3}{2}\beta_K - \left(\frac{R}{R_c}\right)^{3/2}\right) \end{aligned} \tag{3.3.11}$$

Further introducing the necessary relations we can re write this as

$$\begin{aligned} y' = {} & \frac{\dot{M}}{6\pi R} - \frac{y}{2R} + 2\varepsilon\mu_q\left(\frac{3\gamma_{dyn}}{\mu_0\sqrt{GM}}\right)^{1/2}\left(\frac{Hy}{\beta_K}\right)^{1/2}R^{-13/4} \\ & + \frac{12\mu_q^2}{\alpha_{ss}\mu_0\sqrt{GM}}\left(\frac{3}{2} - \frac{1}{\beta_K}\left(\frac{R}{R_c}\right)^{3/2}\right)HR^{-13/2}\,. \end{aligned} \tag{3.3.12}$$

or

$$
\begin{aligned}
y' = \frac{\dot{M}}{6\pi R} - \frac{y}{2R} \\
+4\varepsilon\mu_q \left(\frac{\gamma_{dyn} C_p}{\mu_0 G}\right)^{1/2} \alpha_{ss}^{1/20} M^{-1/16} \beta_K^{-3/5} H R^{-61/16} (\Sigma\nu)^{17/40} \\
+\frac{12\mu_q^2}{\alpha_{ss}\mu_0\sqrt{GM}} \left(\frac{3}{2} - \frac{1}{\beta_K}\left(\frac{R}{R_c}\right)^{3/2}\right) H R^{-13/2}
\end{aligned}
\tag{3.3.13}
$$

If we introduce a dimensionless variable Λ through $y = \Lambda\dot{M}$, and another dimensionless radial coordinate r through $R = rR_M$, where R_M is the Magnetospheric radius, the ODE takes the form:

$$
\begin{aligned}
\frac{d\Lambda}{dr} = \frac{1}{6\pi r} - \frac{\Lambda}{2r} + 2\varepsilon\mu_q \left(\frac{3\gamma_{dyn}}{\mu_0\sqrt{GM}\dot{M}}\right)^{1/2} R_{in}^{-9/4} \beta_K^{-1/2} (H\Lambda)^{1/2} r^{-13/4} \\
+\frac{12\mu_q^2}{\alpha_{ss}\mu_0\sqrt{GM}\dot{M}} R_M^{-11/2} H r^{-13/2} \left(\frac{3}{2} - \frac{\omega_s}{\beta_K} r^{3/2}\right),
\end{aligned}
\tag{3.3.14}
$$

or

$$
\begin{aligned}
\frac{d\Lambda}{dr} = \frac{1}{6\pi r} - \frac{\Lambda}{2r} \\
+4\varepsilon\mu_q \left(\frac{\gamma_{dyn} C_p}{\mu_0 G}\right)^{1/2} \alpha_{ss}^{1/20} M^{-1/16} R_M^{-45/16} \dot{M}^{-23/40} \beta_K^{-3/5} H r^{-61/16} \Lambda^{17/40} \\
+\frac{12\mu_q^2 R_M^{-11/2}}{\alpha_{ss}\mu_0\sqrt{GM}\dot{M}} H r^{-13/2} \left(\frac{3}{2} - \frac{\omega_s}{\beta_K} r^{3/2}\right).
\end{aligned}
\tag{3.3.15}
$$

ω_s is the fastness parameter defined by

$$
\omega_s = \left(\frac{R_{in}}{R_{co}}\right)^{3/2} = 0.21 \dot{M}_{13}^{-3/11} M_1^{-5/11} \mu_{q24}^{6/11} P_{spin}^{-1},
\tag{3.3.16}
$$

and

$$R_M = \left(\frac{2\pi^2 \mu_q^2}{GM\dot{M}^2 \mu_0^2} \right)^{1/11} = 5.3 \times 10^5 \dot{M}_{13}^{-2/11} M_1^{-1/11} \mu_{q24}^{4/11} \,. \tag{3.3.17}$$

We can now rewrite the ODE in its final form as The final version of our ODE can be of the form

$$\frac{d\Lambda}{dr} = \frac{1}{6\pi r} - \frac{\Lambda}{2r} + C_1 \beta_K^{-1/2} (H\Lambda)^{1/2} r^{-13/4} + C_2 H r^{-13/2} \left(\frac{3}{2} - \frac{\omega_s}{\beta_K} r^{3/2} \right), \tag{3.3.18}$$

where $C_1 = 2\varepsilon\mu_q \left(\frac{3\gamma_{dyn}}{\mu_0 \sqrt{GM\dot{M}}} \right)^{1/2} R_{in}^{-9/4}$ and $C_2 = \frac{12\mu_q^2}{\alpha_{ss}\mu_0\sqrt{GM\dot{M}}} R_{in}^{-11/2}$ or

$$\frac{d\Lambda}{dr} = \frac{1}{6\pi r} - \frac{\Lambda}{2r} + C_1 \beta_K^{-3/5} H r^{-61/16} \Lambda^{17/40} + C_2 \left(\frac{3}{2} - \frac{\omega_s}{\beta_K} r^{3/2} \right) H r^{-13/2} \,. \tag{3.3.19}$$

where $C_1 = 2\varepsilon\mu_q \left(\frac{\gamma_{dyn} C_p}{\mu_0 G} \right)^{1/2} \alpha_{ss}^{1/20} M^{-1/16} R_M^{-45/16} \dot{M}^{-23/40}$ and $C_2 = \frac{12\mu_q^2 R_M^{-11/2}}{\alpha_{ss}\mu_0\sqrt{GM\dot{M}}}$

We can further transform our equation by defining the unit less parameter ξ as $r = 1/\xi$, and rewrite it as If we further transform our equation through unit less variable ξ as $x = 1/\xi$, Eq. (3.3.18) and (3.3.19) respectively take the form

$$\frac{d\Lambda}{d\xi} = -\frac{1}{6\pi\xi} - \frac{\Lambda}{2\xi} - C_1 \beta_K^{-1/2} H^{1/2} \Lambda^{1/2} \xi^{5/4} - C_2 H \left(\frac{3}{2} - \frac{\omega_s}{\beta_K} \xi^{-3/2} \right) \xi^{9/2}, \tag{3.3.20}$$

where $C_1 = 2\varepsilon\mu_q \left(\frac{3\gamma_{dyn}}{\mu_0 \sqrt{GM\dot{M}}} \right)^{1/2} R_{in}^{-9/4}$ and $C_2 = \frac{12\mu_q^2}{\alpha_{ss}\mu_0\sqrt{GM\dot{M}}} R_M^{-11/2}$ or

$$\frac{d\Lambda}{d\xi} = -\frac{1}{6\pi\xi} + \frac{\Lambda}{2\xi} - C_1 \beta_K^{-3/5} H \Lambda^{17/40} \xi^{19/16} - C_2 H \left(\frac{3}{2} - \frac{\omega_s}{\beta_K} \xi^{-3/2} \right) \xi^{9/2}, \tag{3.3.21}$$

where $C_1 = 2\varepsilon\mu_q \left(\frac{\gamma_{dyn} C_p}{\mu_0 G} \right)^{1/2} \alpha_{ss}^{1/20} M^{-1/16} R_M^{-45/16} \dot{M}^{-23/40}$ and $C_2 = \frac{12\mu_q^2 R_M^{-11/2}}{\alpha_{ss}\mu_0\sqrt{GM\dot{M}}}$

3.4 Result and Discussion

3.4.1 Analytic Solution - disk structure equations

The physical structure of an accretion disk can be found analytically, and some of the results are given below. The following approximations (thin disk approximations) are made in solving structure equations. $\beta_K^2 \cong 1$, and as well all other related higher order term approximations similarly follow. In most cases we can assume the gas pressure is dominant (see Shapiro & Teukolsky 1983), and then we can write

$$H = \frac{1}{\Omega_K}\left(\frac{K_B T_c}{\bar{\mu} m_p}\right)^{\frac{1}{2}} = \left(\frac{K_B}{m_p G}\right)^{\frac{1}{2}} \bar{\mu}^{-1/2} M^{-1/2} T_c^{1/2} R^{3/2}\,. \tag{3.4.1}$$

Solving for density we get

$$\rho = \frac{3}{4}\left(\frac{m_p}{K_B}\right)^{3/2} G \beta_K \alpha_{ss}^{-1} \Sigma\nu \bar{\mu}^{3/2} M R^{-3} T_c^{-3/2}\,. \tag{3.4.2}$$

The gas pressure is then similarly given by

$$P_g = \frac{3}{4}\alpha_{ss}^{-1}\left(\frac{m_p \bar{\mu}}{K_B}\right)^{1/2} \beta_K \Sigma\nu G M R^{-3} T_c^{-1/2}, \tag{3.4.3}$$

When gas pressure is dominant, for the combined opacity the temperature is

$$T_c = C_1(\kappa_K + \kappa_{es})^{1/5} \beta_K^{3/5} \alpha_{ss}^{-1/5} (\Sigma\nu)^{2/5} \bar{\mu}^{1/5} R^{-9/10} M^{3/10}, \tag{3.4.4}$$

where

$$C_1 = \left(\frac{81 m_p}{128 \sigma K_B}\right)^{1/5} G^{3/10} \tag{3.4.5}$$

Then the plasma density for combined opacity is

$$\rho = C_{c1}(\kappa_K + \kappa_{es})^{-3/10}\beta_K^{1/10}\alpha_{ss}^{-7/10}(\Sigma\nu)^{2/5}\bar{\mu}^{6/5}M^{11/20}R^{-33/10}, \tag{3.4.6}$$

where

$$C_{c1} = G^{11/20}\frac{3}{4}\left(\frac{81}{128\sigma}\right)^{-3/10}\left(\frac{m_p}{K_B}\right)^{6/5}, \tag{3.4.7}$$

The part of the disk inside the radius at which electron scattering opacity is dominant includes, the region in which the magnetic perturbation of the disk becomes strong. Then the plasma density for electron scattering opacity is

$$\rho = C_{e1}\beta_K^{1/10}\alpha_{ss}^{-7/10}(\Sigma\nu)^{2/5}\bar{\mu}^{6/5}M^{11/20}R^{-33/10}, \tag{3.4.8}$$

where

$$C_{c1} = G^{11/20}\frac{3}{4}\left(\frac{81\kappa_{es}}{128\sigma}\right)^{-3/10}\left(\frac{m_p}{K_B}\right)^{6/5}, \tag{3.4.9}$$

$$T_c = C_{e2}\beta_K^{3/5}\alpha_{ss}^{-1/5}(\Sigma\nu)^{2/5}\bar{\mu}^{1/5}M^{3/10}R^{-9/10}, \tag{3.4.10}$$

where

$$C_{e2} = G^{3/10}\left(\frac{81\kappa_{es}m_p}{128\sigma K_B}\right)^{1/5}, \tag{3.4.11}$$

The scale height for this case is

$$H = C_{e3}\beta_K^{3/10}\alpha_{ss}^{-1/10}(\Sigma\nu)^{1/5}\bar{\mu}^{-2/5}M^{-7/20}R^{21/20}, \tag{3.4.12}$$

where

$$C_{e3} = G^{-7/20}\left(\frac{81\kappa_{es}}{128\sigma}\right)^{1/10}\left(\frac{K_B}{m_p}\right)^{\frac{2}{5}}, \tag{3.4.13}$$

and

$$P_g = C_{e4}\beta_K^{7/10}\alpha_{ss}^{-9/10}G^{17/20}M^{17/20}(\Sigma\nu)^{4/5}R^{-51/20}, \tag{3.4.14}$$

$$C_{e4} = \frac{3}{4}\left(\frac{81\kappa_{es}}{128\sigma}\right)^{-1/10}\left(\frac{m_p\bar{\mu}}{K_B}\right)^{2/5}, \tag{3.4.15}$$

For gas pressure and electron scattering opacity, when electron scattering is dominant the scale height is

$$H = \left(\frac{81\beta_K^3\kappa_{es}}{128\sigma\alpha_{ss}}\right)^{1/10}\left(\frac{K_B}{m_p\bar{\mu}}\right)^{\frac{2}{5}}\left(\frac{GM}{R^3}\right)^{\frac{-7}{20}}(\Sigma\nu)^{1/5} \tag{3.4.16}$$

$$B_{\phi,dyn} = C_{d1}\varepsilon(\mu_0\gamma_{dyn})^{1/2}\beta_K^{1/2}(GM)^{13/40}R^{-39/40},, \tag{3.4.17}$$

where

$$C_{d1} = \left(\frac{3}{4}\right)^{1/2} \left(\frac{81\beta_K^3 \kappa_{es}}{128\sigma\alpha_{ss}}\right)^{1/20} \left(\frac{K_B}{m_p\bar{\mu}}\right)^{\frac{1}{5}}, \tag{3.4.18}$$

$$B_{\phi,shear} = 3\alpha_{SS}^{-1}\mu_q R_{in}^{-4} r^{-4} \left(\frac{3}{2}\beta_K - \omega_s r^{3/2}\right) \tag{3.4.19}$$

When the Kramer’s opacity is greater than electron scattering ($\kappa_K >> \kappa_{es}$):

The optical depth for Kramer’s opacity is

$$\tau_{c,K} = \frac{9}{16} G^{3/2} \left(\frac{m_p}{K_B}\right)^{5/2} \kappa_0 \beta_K^2 \alpha_{ss}^{-2} (\Sigma\nu)^2 \bar{\mu}^{5/2} T_c^{-6} M^{3/2} R^{-9/2}, \tag{3.4.20}$$

and

$$\tau_c = 2.28 \times 10^4 \alpha_{SS}^{-4/5} \bar{\mu} \dot{M}_{13}^{1/5} \Lambda^{1/5}, \tag{3.4.21}$$

(i.e., The optical depth of quadrupolar accretion is independent of radial distance R, mass of the NS, and the magnetic moment of the NS).

Temperature of an Accretion Disk

$$T_c = C_{t2} \beta_K^{2/5} \alpha_{ss}^{-1/5} \bar{\mu}^{1/4} M^{1/4} (\Sigma\nu)^{3/10} R^{-3/4}, \tag{3.4.22}$$

where

$$C_{t2} = \left(\frac{243\kappa_0}{512\sigma}\right)^{1/10} \left(\frac{G m_p}{K_B}\right)^{1/4} \tag{3.4.23}$$

and

$$T_c = 2.63 \times 10^6 \beta_K^{2/5} \alpha_{SS}^{-1/5} \bar{\mu}^{-1/4} \dot{M}_{13}^{24/55} M_1^{14/44} \mu_{q24}^{-3/11} \Lambda^{3/10} r^{-3/4}, \tag{3.4.24}$$

Density of an Accretion Disk

$$\rho = C_{d2} \beta_K^{-3/5} \alpha_{ss}^{-7/10} (\Sigma\nu)^{11/20} \bar{\mu}^{9/8} M^{5/8} R^{-15/8}, \tag{3.4.25}$$

where

$$C_{d2} = \frac{3}{4} \left(\frac{243\kappa_0}{512\sigma}\right)^{-3/20} G^{5/8} \left(\frac{m_p}{K_B}\right)^{9/8}, \tag{3.4.26}$$

and

$$\rho = 1.570843 \beta_K^{-3/5} \alpha_{SS}^{-7/10} \bar{\mu}^{9/8} \dot{M}_{13}^{49/55} M_1^{35/44} \mu_{q24}^{-15/22} \Lambda^{11/20} r^{-15/8}, \tag{3.4.27}$$

Height of an Accretion Disk

$$H = C_{h2} \beta_K^{1/5} \alpha_{ss}^{-1/10} \bar{\mu}^{-3/8} (\Sigma\nu)^{3/20} M^{-3/8} R^{9/8}, \tag{3.4.28}$$

where

$$C_{h2} = \left(\frac{243\kappa_0}{512\sigma}\right)^{1/20} \left(\frac{K_B}{m_p G}\right)^{\frac{3}{8}}, \tag{3.4.29}$$

and

$$H = 4.73993 \times 10^3 \beta_K^{1/5} \alpha_{SS}^{-1/10} \bar{\mu}^{-3/8} \dot{M}_{13}^{-3/55} M_1^{-21/44} \mu_{q24}^{9/22} \Lambda^{3/20} r^{9/8}, \tag{3.4.30}$$

Aspect ratio of an Accretion Disk

$$\frac{H}{R} = 0.008934\beta_K^{1/5}\alpha_{SS}^{-1/10}\bar{\mu}^{-3/8}\dot{M}_{13}^{7/55}M_1^{-17/44}\mu_{q24}^{1/22}\Lambda^{3/20}r^{1/8}, \tag{3.4.31}$$

This also shows that the disk proposed here is thinner than the standard disks of $H/R \sim 0.05$(e.g. Frank, King & Raine 2002)

Surface Density of the Accretion Disk

$$\Sigma = C_{\Sigma 1}\beta_K^{-2/5}\alpha_{ss}^{-4/5}(\Sigma\nu)^{7/10}\bar{\mu}^{3/4}M^{1/4}R^{-3/4}, \tag{3.4.32}$$

where

$$C_{\Sigma 1} = \frac{3}{2}G^{1/4}\left(\frac{243\kappa_0}{512\sigma}\right)^{-1/10}\left(\frac{m_p}{K_B}\right)^{3/4}, \tag{3.4.33}$$

and

$$\Sigma = 1.4891373 \times 10^4\beta_K^{-2/5}\alpha_{SS}^{-7/10}\bar{\mu}^{9/8}\dot{M}_{13}^{46/55}M_1^{7/22}\mu_{q24}^{-3/11}\Lambda^{7/10}r^{-3/4}, \tag{3.4.34}$$

This result shows that the surface density increases as the disk comes closer to the NS due to increased gravitational effect.

pressure of an accretion disk

$$P_g = C_{p4}\left(\frac{GM}{R^3}\right)^{7/8}\alpha_{ss}^{-9/10}\beta_K^{4/5}(\Sigma\nu)^{17/20}, \tag{3.4.35}$$

where

$$C_{p4} = \frac{3}{4}\left(\frac{243\kappa_0}{512\sigma}\right)^{-1/20}\left(\frac{\bar{\mu} m_p}{K_B}\right)^{3/8}, \tag{3.4.36}$$

and

$$P = 0.003153\beta_K^{4/5}\alpha_{ss}^{-9/10}\bar{\mu}^{-1/2}\dot{M}_{13}^{73/55}M_1^{49/44}\mu_{q24}^{-21/22}\Lambda^{17/20}r^{-21/8}, \tag{3.4.37}$$

The radial velocity of accretion

$$V_R = C_{\Sigma 2}\beta_K^{2/5}\alpha_{ss}^{4/5}(\Sigma\nu)^{-7/10}\bar{\mu}^{-3/4}M^{-1/4}\dot{M}R^{-1/4}, \tag{3.4.38}$$

where

$$C_{\Sigma 2} = \frac{1}{3\pi}G^{-1/4}\left(\frac{243\kappa_0}{512\sigma}\right)^{1/10}\left(\frac{m_p}{K_B}\right)^{-3/4}, \tag{3.4.39}$$

and

$$V_R = 201.558\beta_K^{2/5}\alpha_{SS}^{4/5}\bar{\mu}^{-3/4}\dot{M}_{13}^{19/55}M_1^{-5/22}\mu_{q24}^{1/11}\Lambda^{-7/10}r^{-1/4}, \tag{3.4.40}$$

For gas pressure and Kramer's opacity, when Kramer's opacity is dominant the scale height is

$$H = \beta_K^{1/5}\left(\frac{243\kappa_0}{512\sigma}\right)^{1/20}\left(\frac{K_B R^3}{m_p\bar{\mu} GM}\right)^{\frac{3}{8}}\alpha_{ss}^{-1/10}(\Sigma\nu)^{3/20}, \tag{3.4.41}$$

The Dynamo component Magnetic Field

$$B_{\phi,dyn} = C_{m4}\varepsilon(\mu_0\gamma_{dyn})^{1/2}\left(\frac{GM}{R^3}\right)^{7/16}\alpha_{ss}^{1/20}\beta_K^{2/5}(\Sigma\nu)^{17/40}, \tag{3.4.42}$$

where

$$C_{m4} = \left(\frac{3}{4}\right)^{1/2} \left(\frac{243\kappa_0}{512\sigma}\right)^{-1/40} \left(\frac{\bar{\mu} m_p}{K_B}\right)^{3/16}, \tag{3.4.43}$$

and

$$B_{\phi,dyn} = 0.05615\varepsilon\beta_K^{2/5}\mu_0^{1/2}\bar{\mu}^{3/16}\alpha_{SS}^{1/20}\gamma_{dyn}^{1/2}\dot{M}_{13}^{73/110}M_1^{49/88}\mu_{q24}^{-21/44}\Lambda^{17/40}r^{-21/16} \tag{3.4.44}$$

The shear magnetic field component

$$B_{\phi,shear} = -\alpha_{SS}^{-1}\mu_q R_{in}^{-4} r^{-4}\left(\frac{9}{2}\beta_K - \omega_s r^{3/2}\right) \tag{3.4.45}$$

$$B_{\phi,shear} = -12.6515\alpha_{SS}^{-1}\bar{\mu}^{-1/4}\dot{M}_{13}^{8/11}M_1^{4/11}\mu_{q24}^{-5/11}\left(\frac{9}{2}\beta_K - \omega_s r^{3/2}\right) r^{-4}, \tag{3.4.46}$$

Both dynamo and shear components of toroidal magnetic fields are relatively higher as compared to dipolar field. This may be due to the very nature of quadrupole field short range activity and the very position of quadrupolar disk to central star.

When the radiation pressure is dominant

$$H = \beta_K^2\left(\frac{9\kappa_{es}}{8c}\right)(\Sigma\nu), \tag{3.4.47}$$

which is independent of R. In the region where the radiation pressure is dominant and this is due due to the electron scattering, the depth of the layer is very thin.

$$\rho = \frac{3}{4}\left(\frac{8c}{9\kappa_{es}}\right)^3\left(\frac{R^3}{GM}\right)^{1/2}\beta_K^{-5}\alpha_{ss}^{-1}(\Sigma\nu)^{-2}. \tag{3.4.48}$$

Temperature of an Accretion DisK

$$T_c = \left(\frac{81\kappa_{es}}{128\sigma}\right)^{1/4}\left(\frac{8c}{9\kappa_{es}}\right)^{1/2}\beta_K^{-1/4}\alpha_{ss}^{-1/4}(GM)^{1/8}R^{-3/8}, \tag{3.4.49}$$

and

$$T_c = 2.43\times10^6\alpha_{SS}^{-1/5}\overline{\mu}^{-1/4}\dot{M}_{13}^{24/55}M_1^{14/44}\mu_{q24}^{-3/11}\Lambda^{3/10}r^{-3/4}, \tag{3.4.50}$$

The optical depth of Accretion Disk

$$\tau_c = 261.832\alpha_{SS}^{-4/5}\overline{\mu}\dot{M}_{13}^{1/5}\Lambda^{1/5}, \tag{3.4.51}$$

(i.e., The optical depth of quadrupolar (also dipolar) accretion is independent of radial distance, mass of the NS, and the magnetic moment of the NS).

3.4.2 Numerical Solutions

For this thin disk, we take a neutron star of of mass ~ 1.4 $M_\odot$ and a magnetic moment of 10^{24} Tm^4, which is accreting at the rate 10^{13} kg s^{-1}. The dimensionless parameter γ_{dyn} is 10 in our model, while $\alpha_{ss} = 0.01$. In addition we vary a newly introduced variable β_K and parameter ε to find the disk solutions.

The thin disc solution of the density of an accretion disc is shown in Figures 3.1 - 3.6. In Figure 3.1 results corresponding to ε = 0.1, 0.05 and 0, from top to the bottom respectively are given. To get a good picture of this we can take the points of maxima (peaks) as references and consider the left and right panels of this plot for discussion.

The deviation from Keplerian rotation is in general a second-order correction with little influence on the steady disk structure, specially for a thin disk. It is possible to physically rewrite the pressure gradient as $\frac{dP}{dR} \sim \frac{dP}{d\rho}\left(\frac{d\rho}{dR}\right)$ in which the first term on the right hand side is always positive, whereas the quantity in the bracket can be positive or negative. We have introduced this fact in defining β_K in relation to Eq. (2.2.28)

The densities corresponding to the three peaks in Figure 3.1 are 18.18 kg/m^3, 16.64 kg/m^3, &14.81 kg/m^3 respectively and these occur at approximately 1.467, 1.537 and 1.685 R$_M$. On the other hand, since R$_A$=1.134 R$_M$, this gives the peak corresponding to $\varepsilon = 0$, to be at r$_{peak,\varepsilon=0}$= 1.467 R$_M$=1.29 R$_A$ $\sim$ R$_A$. This shows that the internal dynamo has a peak lowering and shifting effect, which in absence of it is of the order of R$_A$.

Fortunately in the density plots the sign of density gradient, is positive ($\frac{\partial\rho}{\partial R} > 0$), for the inner most part of accretion disk on the left side, and negative ($\frac{\partial\rho}{\partial R} < 0$), at relatively larger radius on the right side of the peaks. The effect of the internal dynamo is to redistribute the central density according to $\rho_{\varepsilon=0.1} < \rho_{\varepsilon=0.05} < \rho_{\varepsilon=0}$ for $r < r_a$ and $\rho_{\varepsilon=0} < \rho_{\varepsilon=0.05} < \rho_{\varepsilon=0.1}$ for $r > r_c$ (refer to Fig. 3.1). The region between r_a and r_c ($r_c - r_a << R_A$) is a density transition region with no significant interest. Consequently, Ω or V_ϕ assumes the Keplerian value Ω_K=(GM/R^3)$^{(1/2)}$ or V$_\phi$=(GM/R)$^{(1/2)}$, in this transition layer.

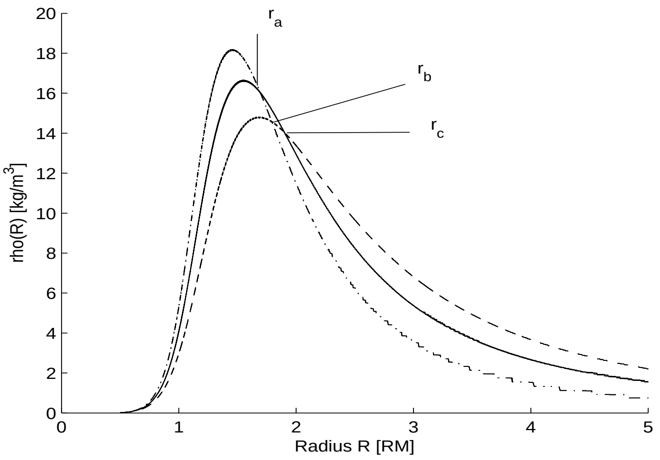

Figure 3.1: The Variation of density of an accretion disk around magnetic star with r, where the curves correspond to $\varepsilon = 0$,the dash dot line $\varepsilon = 0.05$,the solid line, and $\varepsilon = 0.1$,dashed line from top to the bottom respectively (i. e. taking peaks).

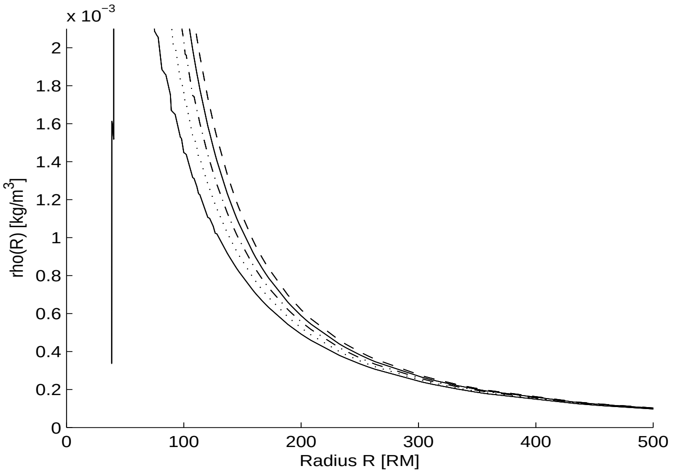

Figure 3.2: The Variation of density of an accretion disk around magnetic star with r, where the curves correspond to $\varepsilon = 0$,the dash dot line $\varepsilon = 0.05$,the solid line, and $\varepsilon = 0.1$,dashed line from top to the bottom respectively (i. e. taking peaks).

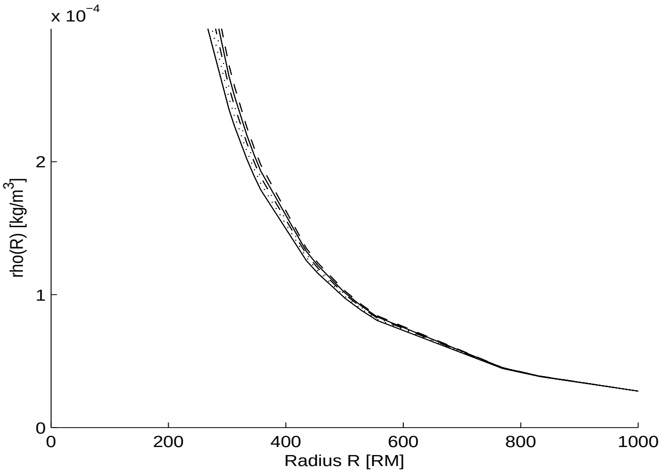

Figure 3.3: The Variation of density of an accretion disk around magnetic star with r, where the curves correspond to $\varepsilon = 0$,the dash dot line $\varepsilon = 0.05$,the solid line, and $\varepsilon = 0.1$,dashed line from top to the bottom respectively (i. e. taking peaks).

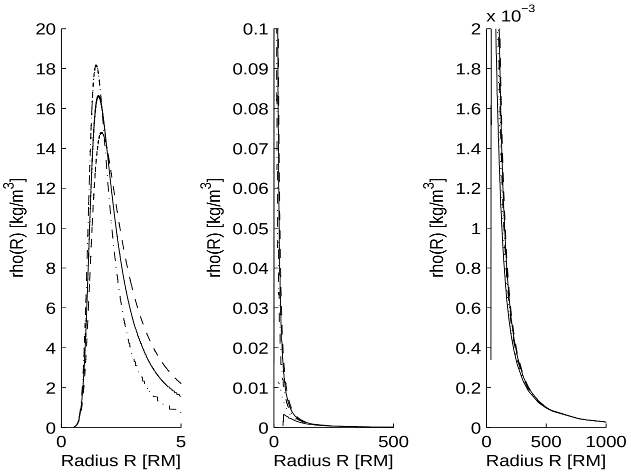

Figure 3.4: The Variation of density of an accretion disk around magnetic star with r, where the curves correspond to $\varepsilon = 0$,the dash dot line $\varepsilon = 0.05$,the solid line, and $\varepsilon = 0.1$,dashed line from top to the bottom respectively (i. e. taking peaks).

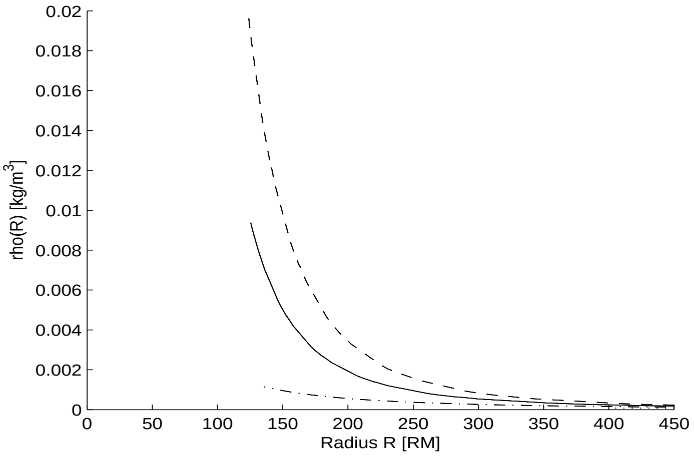

Figure 3.5: The Variation of density of an accretion disk around magnetic star with r, in the mid region of the disk where the curves correspond to $\varepsilon = 0.1$,dashed line, to $\varepsilon = 0.05$,the solid line,to $\varepsilon = 0$,the dash dot line.

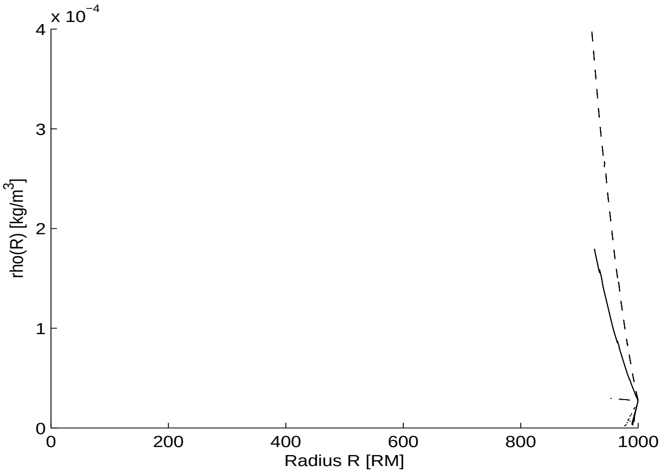

Figure 3.6: The Variation of density of an accretion disk around magnetic star with r, in the outer region where gas pressure and Kramer's opacity is dominant - where the curves correspond to $\varepsilon = 0.1$,dashed line, to $\varepsilon = 0.05$,the solid line,to $\varepsilon = 0$,the dash dot line.

From Figure 3.1 it is obvious that for the region to the left of the peaks it is super-Keplerian in nature, while that to the right sub-Keplerian. This agrees with paper by Campbell (2011)

The solution of the disk central temperature for ε= 0.1, 0.05, and 0, are shown in Fig. 3.7 from top to the bottom respectively. At the inner boundary the value of temperature is of the order of 10^7 K (i.e., 2.1×10^7 K). Here no significant effect of dynamo component is observed for r$\leq$ R_A. However, the dynamo effect is clearly observed in the middle part beyond R_A (see Figs. 3.7 & 3.11).

Since the gas pressure varies directly with the plasma density, we can predict its variation from density variation. The gas pressure at the inner radius is minimum. To the left of the peak as we approach the central star gas pressure decreases as magnetic pressure increases. On the other hand the radiation pressure near the inner radius is high, corresponding to the maximum value of temperature as shown in Figure 3.7.

The variation of Lambda as a function of r for a thin accretion disk, are shown in Figure 3.13 (combined Lambda plot) The plot on the left side (Fig 3.13 (a)), corresponds to the region around the inner radius for positive values of $\varepsilon = 0.1, 0.05$ and 0, from top to bottom respectively. The value of Lambda at the inner radius is the maximum possible and it is of the order of ~ 350. This may be basically due to the MRI that is expected to be a source

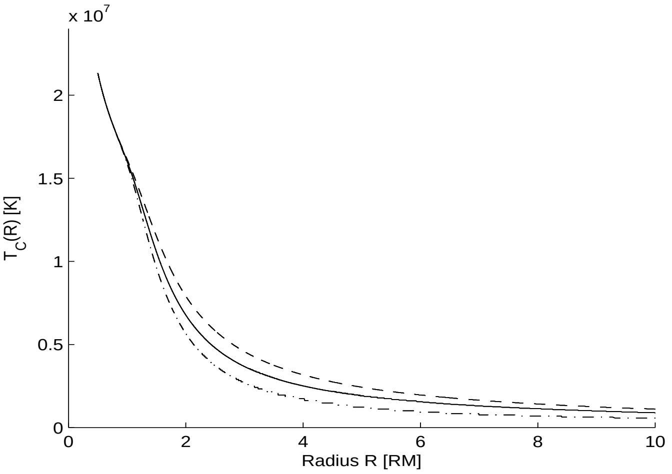

Figure 3.7: The Variation of Central Temperature of an accretion disk around magnetic star with r, where the curves correspond to $\varepsilon = 0$,the dash dot line $\varepsilon = 0.05$,the solid line, and $\varepsilon = 0.1$,dashed line from top to the bottom respectively.

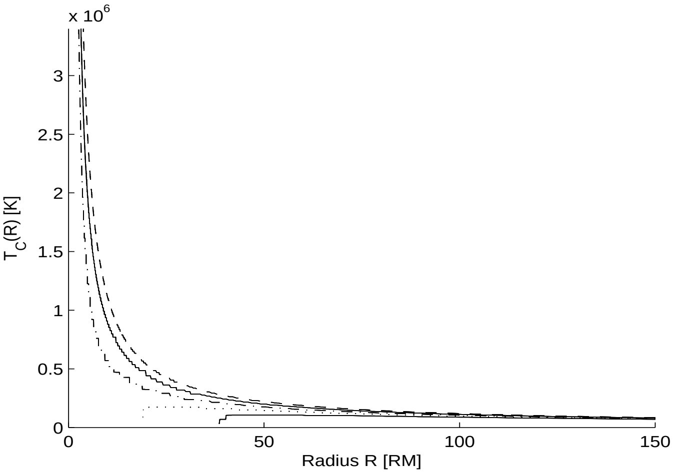

Figure 3.8: The Variation of Central Temperature of an accretion disk around magnetic star with r, where the curves correspond to $\varepsilon = 0$,the dash dot line $\varepsilon = 0.05$,the solid line, and $\varepsilon = 0.1$,dashed line from top to the bottom respectively.

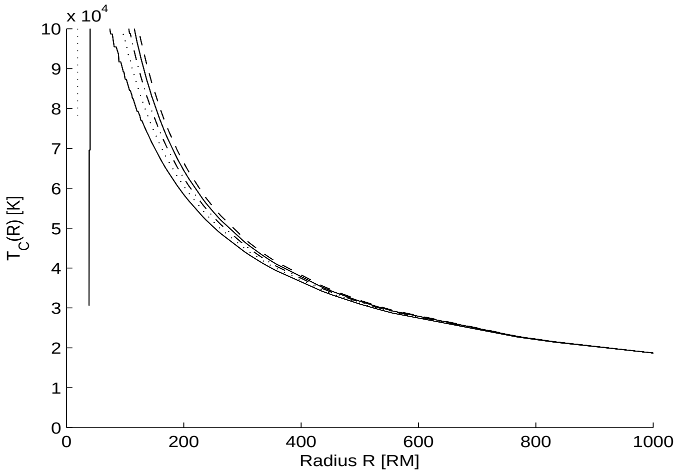

Figure 3.9: The Variation of Central Temperature of an accretion disk around magnetic star with r, where the curves correspond to $\varepsilon = 0$,the dash dot line $\varepsilon = 0.05$,the solid line, and $\varepsilon = 0.1$,dashed line from top to the bottom respectively.

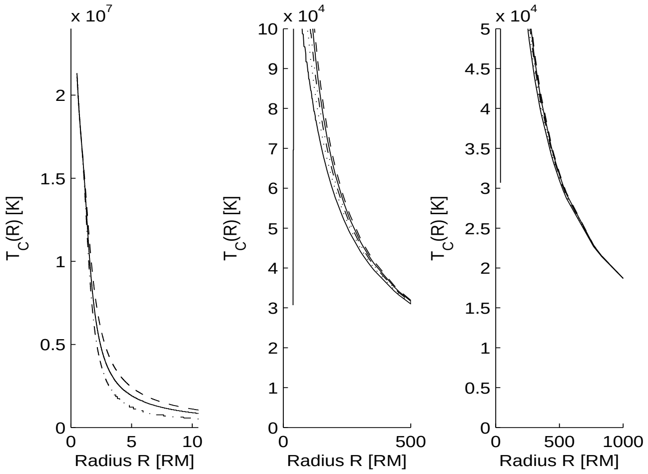

Figure 3.10: The Variation of Central Temperature of an accretion disk around magnetic star with r, where the curves correspond to $\varepsilon = 0$,the dash dot line $\varepsilon = 0.05$,the solid line, and $\varepsilon = 0.1$,dashed line from top to the bottom respectively.

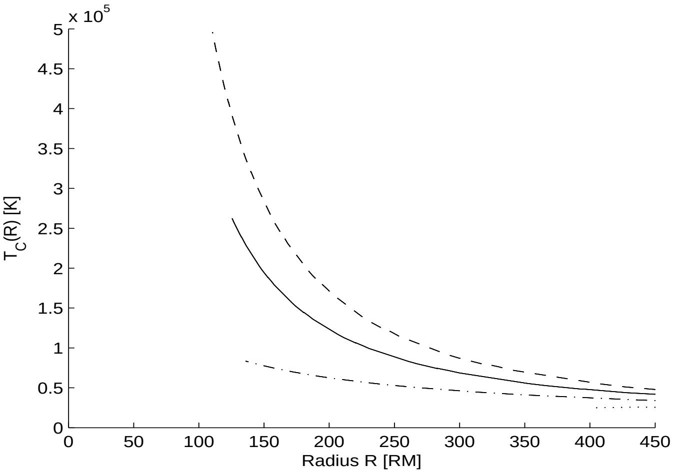

Figure 3.11: The Variation of central temperature of an accretion disk around magnetic star with r, in the mid region of the disk where the curves correspond to ε = 0.1,dashed line, to ε = 0.05,the solid line,to ε = 0,the dash dot line.

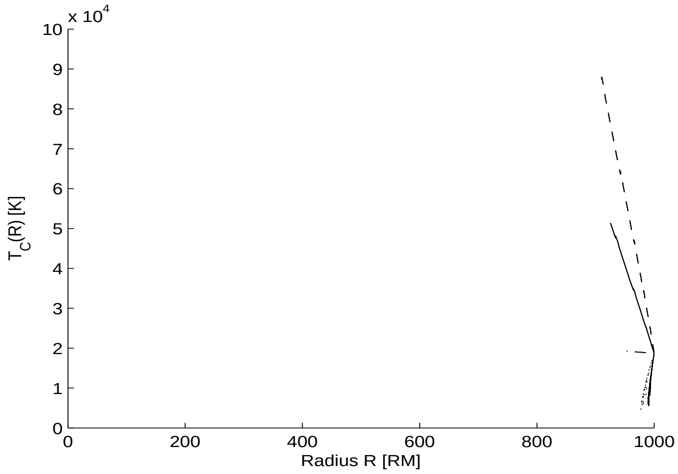

Figure 3.12: The Variation of central temperature of an accretion disk around magnetic star with r, in the outer region where gas pressure and Kramer's opacity is dominant - where the curves correspond to ε = 0.1,dashed line, to ε = 0.05,the solid line,to ε = 0,the dash dot line.

of effective viscosity (Balbus and Hawley 1991), since molecular viscosity is almost the same everywhere. In absence of the internal dynamo the value of Lambda approaches the Shakura-Sunyaev value very rapidly. The contribution of the internal dynamo at the inner boundary is not significant. From the middle plot (Fig. 3.13 (b)), it can clearly be seen that it is enough to consider the positive values of ε due to the symmetric nature of dynamo contribution. The effect of the internal dynamo is clearly observed for the mid-section of the disk as shown in Figure 3.14 and middle plots in Figure 3.13 (a) combined plot. From Fig. 3.13 (c) we notice that for radii ≥ 1000, Lambda approaches the Shakura-Sunyaev value.

Due to the symmetric nature of dynamo contribution results, it is enough to consider the positive values of ε for both density and central temperature, as it is clearly observed in the Lambda case shown in Figure 3.14.

Due to the interaction between the magnetospheric boundary and inner boundary of accretion disk the value of Lambda is maximum in this layer so formed.

In the region between the accretion disk (AD) and the NS, the quadrupolar magnetic field will have an effect of channeling the plasma to the surface of the NS (funnel flow). At the magnetospheric boundary shock waves are formed giving rise to accelerated particles. These particles that bounce back deep into the accretion disk, transfer energy and angular

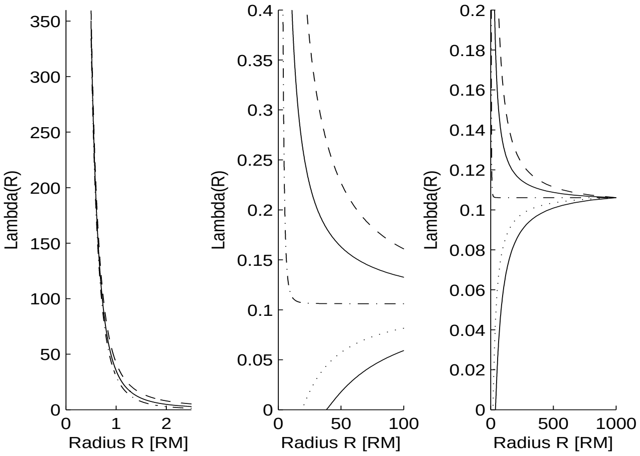

Figure 3.13: The combined plot for Variation of Lambda of an accretion disk around magnetic star with r,where the top, dashed curve corresponds to $\varepsilon = 0.1, 0.05, \mathit{and}\ 0$,the middle, solid curve corresponds to $\varepsilon = 0.05$ and the lower, dashdot curve corresponds to $\varepsilon = 0$,the dotted curve corresponds to $\varepsilon = -0.05$ and the solid curve corresponds to $\varepsilon = -0.1$

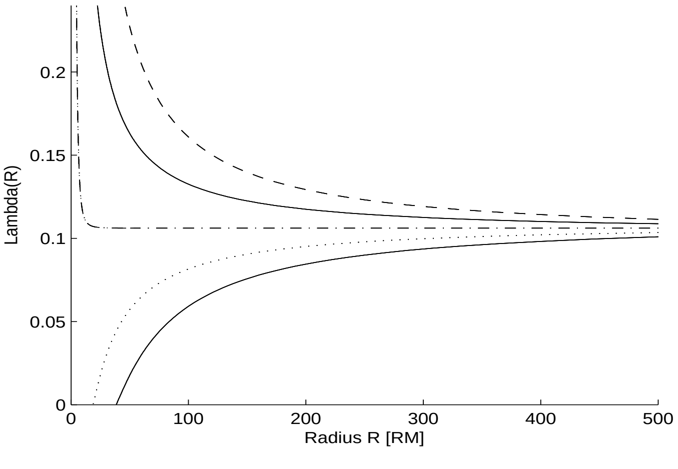

Figure 3.14: The Variation of Lambda of an accretion disk around magnetic star with r,where the top, dashed curve corresponds to $\varepsilon = 0.1$,dashed line, to $\varepsilon = 0.05$,the solid line,to $\varepsilon = 0$,the dash dot line, the dotted curve corresponds to $\varepsilon = -0.05$ and the lower solid curve corresponds to $\varepsilon = -0.1$

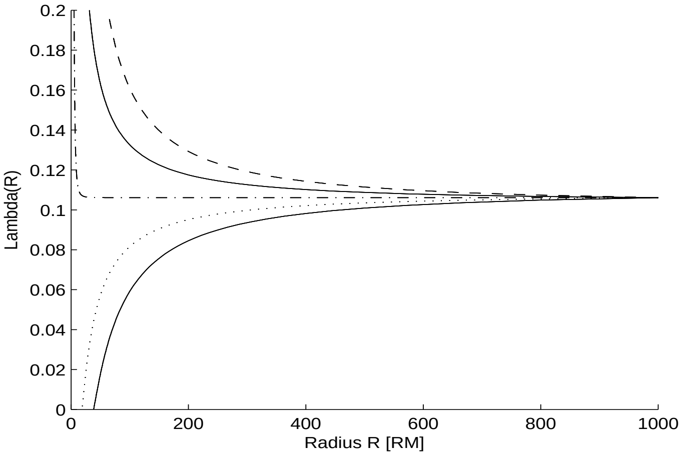

Figure 3.15: The Variation of Lambda of an accretion disk around magnetic star with r,where the top, dashed curve corresponds to $\varepsilon = 0.1$,dashed line, to $\varepsilon = 0.05$,the solid line,to $\varepsilon = 0$,the dash dot line, the dotted curve corresponds to $\varepsilon = -0.05$ and the lower solid curve corresponds to $\varepsilon = -0.1$

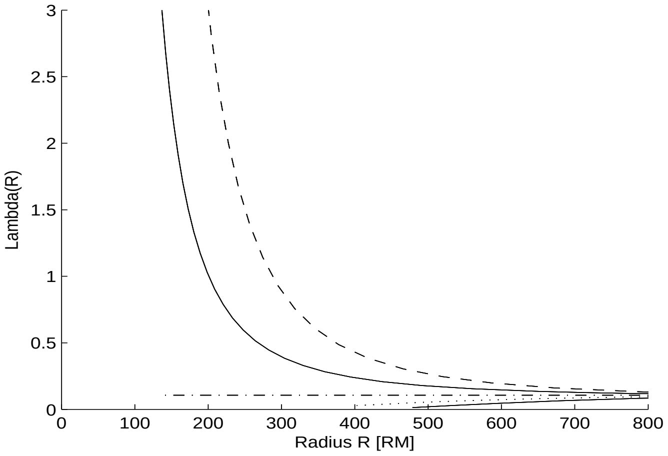

Figure 3.16: The Variation of Lambda of an accretion disk around magnetic star with r, in the mid region of the disk where the curves correspond to $\varepsilon = 0.1$,dashed line, to $\varepsilon = 0.05$,the solid line,to $\varepsilon = 0$,the dash dot line.

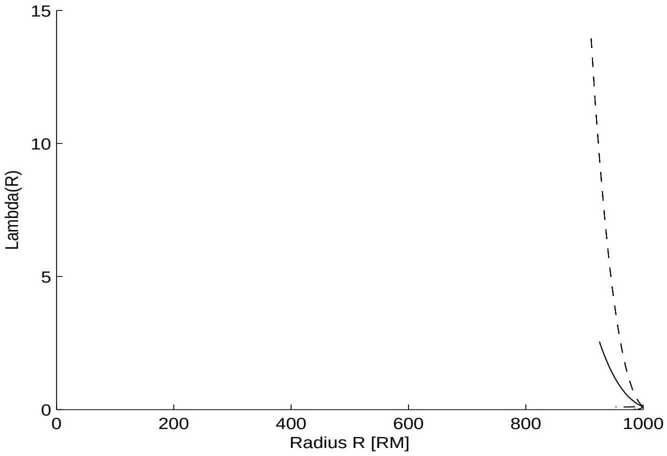

Figure 3.17: The Variation of Lambda of an accretion disk around magnetic star with r, in the outer region where gas pressure and Kramer's opacity is dominant - where the curves correspond to $\varepsilon = 0.1$,dashed line, to $\varepsilon = 0.05$,the solid line,to $\varepsilon = 0$,the dash dot line.

momentum outwards. In the mean time the particles subject to the forward shock will be forced to move against the magnetospheric particles till they lose all their radially directed kinetic energy. Our result shows that this distance is only 0.5 R_M, the inner radius of accretion disk. This is in a good agreement with the results obtained by Gosh and Lamb (Gosh & Lamb) for thin accretion disks.

The problem of sub-Keplerian accretion has long been known, that material falling in an elliptic orbit onto the surface of the disk has sub- Keplerian angular momentum, even in the case of infinitely flat disks. When mixing with the disk material, which is in Keplerian rotation, a torque is exerted that pushes the disk material in towards the star Cassen &

Moosman (1981). The cummulative effect is that the plasma content of the inner AD will be forced to execute super-Keplerian rotation something that extends upto the density peak point (Fig. 3.1). Based on this result we can describe the motion of thin AD as Keplerian-like having distinct super and sub-Keplerian features on either sides of the density peak point. The transition boundary layers in both cases are expected to be thin. The case of similar super-Keplerian outfow from BHs has also been discussed by Marek, et. al (1998) [2] and Mao, et. al. (2009).

3.4.3 Comparison with observation

Observations from X-ray transients, some active galactic nuclei, and the Galactic Centre show that the inner part of an accretion disk can be well described by hot optically thin advection dominated accretion flows. This region rotates with an orbital speed faster than the Keplerian one (super-Keplerian). On the other hand the next outer layer can be described by standard Shakura-Sunyaev accretion disc (SSD). These observations clearly indicate that the SSDADAF transition does occur in accretion discs. However, there is no theoretical ground to bridge this result. Our result agrees very well with this fact since it shows that the inner part of accretion disk is super - Keplerian.

3.5 Conclusion

The contribution of the internal dynamo on the variation of density and temperature at the inner boundary is not significant. Rather its contribution is clearly observed for the middle part of the disk in both cases. On the other hand the opposite is true, when we consider its contribution on variation of Lambda. (i.e., it has observable effect at the inner part). Near outer radius, at relatively large radius (i.e., R=500) the value of Lambda approaches the usual value, as expected in agreement with the Shakura-Sunyaev value.

Near the NS/BH the motion is super-Keplerian though it is over relatively narrower region as compared to sub-Keplerian case, that covers most of the accretion region. It means that the accretion process is dominated by sub-Keplerian accretion. On the other hand, comparison of the non Keplerian and Keplerian rotations of the disk implies that this basically cannot change the basic pattern of the result. Generally the disk appears to be drawn closer to the central star in Keplerian case.

In this work we have tried to study the non-Keplerian behaviour of disk formation around magnetized stellar object. We have identified that, the accretion process shows complexity, since it has mixed nature of super-Keplerian and sub-Keplerian behaviour respectively during its formation around magnetized central star, extending out from inner part to further out. Our result also agrees with the simulation by Mao et al. (2009) that proved the existence of high amplitude, super-Keplerian traveling modes in the inner regions of accretion flow.

We summarize the main results of our study on non-Keplerian-disk in this chapter as follows:

1. Using alpha prescription we are able to find self-similar disk structure solution for non-Keplerian disk, for different disk regions as given in sec. 3.4.1.

2. Our numerical solution in section 3.4.2 gives the variation of density, temperature and viscosity for non-Keplerian disk around magnetic star. The spectrum of emitted radiation is shown in TC plot (Fig. 3.7).

3. The process of accretion disk formation shows complex and mixed behaviour, that it is super-Keplerian in the inner part and sub-Keplerian in the broader outer part.

4. Quadrupolar accretion also shows that there is funnel flow from accretion disk to the central star.along magnetic field lines. The layer between central star and inner boundary of AD is the region of radiation of thermal and non-thermal origin.

- The relatively high viscosity in the inner part of AD can cause magnetic heating that leads to thermal radiation.

-The electric field parallel to the open magnetic field lines near the light cylinder accelerates particles out so that there will be non thermal emission from the magnetospheric boundary and inner AD.

5. The density plot (Fig. 3.1), indirectly demonstrates the nature of disk rotation which is Kepler-like, is a direct implication of the possible energy and angular momentum transport.

6. Our Lambda result shows relatively larger viscosity specially at the inner region of AD where the magnetic field is strong (e.g. Fig. 3.13).

Chapter 4

Accretion Disk around Magnetized Stars III - Slim disk

4.1 Introduction

In this chapter we study the structure of an accretion disc in a quadrupole magnetic field. The fact that there is a hole in the magnetic field at the equatorial plane means that the stellar magnetic field can drive the accretion flow onto the stellar equator from inside the co-rotation radius all the way to the stellar surface. This is different from the situation in a dipolar magnetosphere, in which case the magnetic field forms a barrier in the equatorial plane.

4.2 The mathematical description of a slim disk

The structure of an accretion disc is determined by the basic equations of viscous fluid dynamics: the continuity equation, Navier-Stoke's equation and the equation of conservation of energy, to which we add the effect of the magnetic field through the Lorentz force. For a slim axisymmetric accretion disk we will integrate the equations along the vertical coordinate.

4.2.1 Conservation of Mass

The mass continuity equation of a fluid can be written as

$$\dot{M} = -2\pi R\Sigma\left(R\right) v_R\left(R\right) = 4\pi R\rho\left(R\right) H\left(R\right) v_R\left(R\right), \tag{4.2.1}$$

where v_R is the radial component of the velocity, $\dot{M}$ is the constant mass accretion rate and Σ is the column density obtained from the vertical integral of the density ρ

$$\Sigma(R) = \int_{-H}^{H} \rho(R,z)dz = 2\rho(R)H, \tag{4.2.2}$$

Where $\rho(R)$ denotes the vertically averaged density.

4.2.2 Conservation of momentum (Navier - Stoke's equation)

.

The radial component of the Navier-Stoke's equation takes the form

$$v_R \frac{\partial v_R}{\partial r} + v_z \frac{\partial v_R}{\partial z} - \frac{v_\phi^2}{R} + \left(\frac{\partial \psi}{\partial R}\right) + \frac{1}{\rho}\frac{\partial P}{\partial R} - \frac{1}{\rho}\frac{\partial}{\partial R}\left(\frac{B_\phi^2}{2\mu_0}\right) - \frac{1}{\rho} B_z J_\phi = 0$$

where the toroidal current density $J_\phi = \frac{1}{\mu_0}\left(\frac{\partial B_r}{\partial z} - \frac{\partial B_z}{\partial R}\right)$. We can ignore the last term since in the quadrupolar field $B_z \approx 0$ in the equatorial plane. The pressure, P, is the sum of gas and radiation pressures,

$$P = \frac{\rho k_B T_c}{\bar{\mu} m_p} + \frac{4\sigma T_c^4}{3c}, \tag{4.2.3}$$

where T_c is the central plane temperature, $\mu = 0.62$ is the mean molecular weight for a fully ionised gas of cosmic composition, 0.62, σ_B is the Stefan-Boltzmann constant and c is the speed of light. The vertically integrated form of the radial equation of motion can be rewritten as

$$v_R \frac{\mathrm{d}v_R}{\mathrm{d}R} = \frac{1}{\Sigma}\frac{\mathrm{d}}{\mathrm{d}R}\left(W + \frac{B_\phi^2}{2\mu_0}\right) + \frac{(\ell^2 - \ell_K^2)}{R^3} + \frac{W}{\Sigma}\frac{\mathrm{d}\ln\Omega_K}{\mathrm{d}R} \tag{4.2.4}$$

where $\ell = R v_\phi$ is the specific angular momentum of the gas and ($\ell_K = R^2 \Omega_K$), respectively. The last term in the equation is the correction for the decrease of the radial component of gravitational force $\left(\frac{\partial \psi}{\partial R}\right)$ away from the equator (Honma et al. 1991). This term must be included as it is of the same order as the pressure gradient term. In Eq. (4.2.4) we have a vertically integrated pressure

$$W = \int_{-H}^{H} P_{tot} dz = \int_{-H}^{H} \rho(R,z)\left(c_s^2 + \frac{1}{2} v_A^2\right) dz = \Sigma(R)\left(c_s^2 + \frac{1}{2} v_A^2\right), \tag{4.2.5}$$

Where $P_{tot} = P + P_{mag}$ and c_s is average sound speed. The radial momentum conservation equation, Eq. (4.2.3) implies that a cold non self-gravitating disk in this potential will be geometrically thin and rotate locally with Keplerian velocity, though for slim disks the rotation can be non-Keplerian at some points because of the radial pressure gradient.

4.2.3 Vertical structure: hydrostatic equilibrium

Based on our assumptions the vertical component of the momentum conservation equation is given by

$$\left(\frac{\partial \psi}{\partial z}\right) - \frac{1}{\rho}\frac{\partial}{\partial z}\left(P + \frac{B_\phi^2}{2\mu_0}\right) + \frac{1}{\rho}B_R J_\phi = 0, \tag{4.2.6}$$

For a weak magnetic field the half thickness, H, can be written as

$$P = \rho\frac{GM}{R^3}H^2 = \frac{1}{2}H\Sigma\frac{GM}{R^3}, \tag{4.2.7}$$

where P is the pressure at the midplane. Solving for H

$$H = \frac{c_s}{\Omega_K} = \frac{1}{\Omega_K}\left(\frac{K_B T_c}{\bar{\mu} m_p} + \frac{4\sigma T_c^4}{3c\rho}\right)^{\frac{1}{2}}, \tag{4.2.8}$$

4.2.4 Angular momentum conservation

The viscous term plays an important role in the azimuthal component of the Navier-Stokes equation

$$\rho v_R \frac{\partial \ell}{\partial R} = \frac{1}{R}\frac{\partial}{\partial R}\left(R^3 \nu \Sigma \frac{\partial}{\partial R}\left(\frac{\ell}{R^2}\right)\right) + \left[\frac{1}{R}\frac{\partial}{\partial R}\left(R^2\frac{B_R B_\phi}{\mu_0}\right) + \frac{\partial}{\partial R}\left(R^2\frac{B_z B_\phi}{\mu_0}\right)\right], \tag{4.2.9}$$

where $\ell = Rv_\phi = R^2\Omega$. The vertically integrated form is

$$\Sigma v_R \frac{\partial \ell}{\partial R} = \frac{1}{R}\frac{\partial}{\partial R}\left(R^3 \nu \Sigma \frac{\partial}{\partial R}\left(\frac{\ell}{R^2}\right)\right) + \frac{1}{R}\int_{-H}^{H} \frac{\partial}{\partial R}\left(R^2 \frac{B_R B_\phi}{\mu_0}\right) dz. \tag{4.2.10}$$

Here we have ignored the $B_z B_\phi$ term, since $B_z = 0$ for a quadrupole field. This equation relates the radial advection of angular momentum to the viscous and magnetic torques. Multiplying both sides with R we can get a constant factor in front of the derivative on the LHS

$$-\frac{\dot{M}}{2\pi}\frac{\partial (Rv_\phi)}{\partial R} = \frac{\partial}{\partial R}\left(R^3 \nu \Sigma \frac{\partial}{\partial R}\left(\frac{v_\phi}{R}\right)\right) + 2H(R)\frac{\partial}{\partial R}\left(R^2 \frac{B_R B_\phi}{\mu_0}\right). \tag{4.2.11}$$

4.2.5 Viscosity

The molecular viscosity is too small to drive the accretion flow, rather the source of the viscosity is likely to be small scale turbulence in the disc. Based on mixing length theory the turbulent viscosity can be written as,

$$\nu = \ell_t v_t, \tag{4.2.12}$$

where ℓ_t is a typical turbulent length scale and v_t a typical turbulent velocity. The length scale of the turbulence cannot be larger than the scale height of the disc, H, and the turbulence should be subsonic. Thus we write the viscosity as

$$\nu = \alpha_{SS} c_s H, \tag{4.2.13}$$

where α_{SS} is a parameter that is ≤ 1.

4.2.6 The Magnetic Field

The accretor is taken to have a magnetic quadrupole moment μ_q parallel to the rotational axes of the accretor and the accretion disc. In the plane of the disc the quadrupole field has only a radial component

$$B_R = \frac{\mu_q}{R^4} = B_0 \left(\frac{R_0}{R} \right)^4 , \tag{4.2.14}$$

where B_0 is the field strength at the poles of the star, and R_0 its radius. The structure of the magnetic field in the accretion disc is determined by the induction equation.

$$\frac{\partial B}{\partial t} = \nabla \times (v \times B - \eta \nabla \times B)) , \tag{4.2.15}$$

where η is the magnetic diffusivity of the plasma. The dominant terms are the shear between the disc and the star, the shear due to the differential rotation of the disc, and the vertical diffusion through the disc. The azimuthal component of Eq. (2.2.35) reduces then to

$$\frac{\partial B_\phi}{\partial t} = \frac{\partial}{\partial z} \left(\eta \frac{\partial B_\phi}{\partial z} \right) + \frac{\partial}{\partial R} \left(v_\phi B_R \right) . \tag{4.2.16}$$

Since we look for a stationary solution we ignore the time derivative

$$\frac{\partial}{\partial z} \left(\eta \frac{\partial B_\phi}{\partial z} \right) = - \frac{\partial}{\partial R} (v_\phi B_R). \tag{4.2.17}$$

Assuming that the star is rotating at the angular velocity Ω_* and that the angular velocity of the disc is $\Omega(R)$ we can write

$$v_\phi = R(\Omega - \Omega_*), \tag{4.2.18}$$

Finally solving Eq. (2.2.37) we get the vertical distribution of the toroidal magnetic field

$$B_{\phi,shear}(R,z) = -\frac{z^2 - H^2}{2\eta}\frac{\partial}{\partial R}[(\Omega - \Omega_{star})RB_R]. \tag{4.2.19}$$

The magnetic diffusivity, like the viscosity, is due to the turbulence. For simplicity we will assume that $\eta \sim \eta_T \approx \nu$. (e.g. Campbell 1992; Cameron & Campbell 1993; Yi 1995). With Eq. (4.2.13) we can write as

$$B_{\phi,shear} = -\frac{1}{\alpha_{SS}\Omega_K}\frac{\partial}{\partial R}[(\Omega - \Omega_*)RB_R] \tag{4.2.20}$$

The local turbulence in the accretion disc can also generate a toroidal magnetic field through a dynamo action, $B_{\phi,dyn}$. We model this dynamo as Tessema & Torkelsson (2010). Assuming that the viscous stress in the accretion disk is due to the internal magnetic stress, we can estimate the size of $B_{\phi,dyn}$ from the α-prescription. The turbulent magnetic stress is

$$f_{R\phi} = \frac{B_{r,t}B_{\phi,t}}{\mu_0}. \tag{4.2.21}$$

These are the small-scale, turbulent magnetic fields, which are not related to the large-scale fields $B_{\phi,shear}$ and B_R. Based on the results of the numerical simulations of magnetohydrodynamic turbulence in accretion discs (e.g. Brandenburg et al. (1995)) Torkelsson (1998) has argued that

$$\gamma_{dyn} = \frac{B_{\phi,t}}{B_{R,t}}, \tag{4.2.22}$$

where $\gamma_{dyn} \sim 10$. Furthermore in order to account for that the large-scale field generated by the dynamo can be significantly weaker than the turbulent field and directed in either the positive or the negative direction they introduce a parameter $|\varepsilon| \leq 1$, such that $B_{\phi,dyn} = \varepsilon B_{\phi,t}$. This gives us

$$B_{\phi,dyn} = \varepsilon(\mu_0 \alpha_{ss} \gamma_{dyn} P)^{1/2}. \tag{4.2.23}$$

Now combining the two large-scale toroidal fields, the magnetic stress $B_r B_\phi$ takes the form

$$B_R B_\phi = B_R \left(B_{\phi,shear} + B_{\phi,dyn} \right) \tag{4.2.24}$$

4.2.7 Conservation of Energy

The energy balance requires that the rate at which energy is deposited by viscous, Q^+_{visc}, and magnetic, Q^+_{mag}, dissipation at each radius is equal to the energy losses due to radiation, Q^-_{rad} and advection, Q^-_{adv} at the same radius

$$Q^+_{visc} = Q^-_{rad} + Q^-_{adv}. \tag{4.2.25}$$

The viscous heating rate per unit area is given by

$$Q^+_{visc} = \nu \Sigma \left(R \frac{\partial \Omega}{\partial R} \right)^2 = \frac{\alpha_{SS} c_s^2}{\Omega_K} \Sigma \left(R \frac{\partial \Omega}{\partial R} \right)^2. \tag{4.2.26}$$

We ignore the magnetic heating since Tessema & Torkelsson (2010) argued that it is much smaller than the viscous heating. The advective cooling rate can be written

$$Q^{-}_{adv} = \frac{1}{R}\frac{\partial}{\partial R}\left(R\Sigma v_R h\right) = \Sigma v_R \frac{\partial h}{\partial R}, \tag{4.2.27}$$

where h is specific enthalpy and

$$\frac{\partial h}{\partial R} = \frac{1}{\rho}\left(4 - \frac{3}{2}\beta\right)\left(\frac{\partial P}{\partial R} - \frac{P}{\rho}\frac{\partial \rho}{\partial R}\right), \tag{4.2.28}$$

and $\beta = \frac{P_g}{P}$ is the ratio of the gas pressure to the total pressure. The vertically integrated form of the advection term is then,

$$Q^{-}_{adv} = \left(4 - \frac{3}{2}\beta\right)\Sigma v_R \frac{1}{\Sigma R}\left(\frac{\partial W}{\partial R} - \frac{W}{\Sigma}\frac{\partial \Sigma}{\partial R}\right), \tag{4.2.29}$$

This can be also written as

$$Q^{-}_{adv} = \left(4 - \frac{3}{2}\beta\right)\Sigma v_R \frac{W}{\Sigma R}\left(\frac{dlnT}{dlnR} - \frac{W}{\Sigma}\frac{dln\Sigma}{dlnR}\right), \tag{4.2.30}$$

Assuming that the disc is optically thick the energy loss rate in the vertical direction due to radiative cooling can be expressed as

$$Q^{-}_{rad} = \frac{4\sigma_B T_c^4}{3\tau_c}, \tag{4.2.31}$$

The optical depth to the mid-plane of the disk is

$$\tau_c = \rho_c H \kappa_c = \rho_c H(\kappa_K + \kappa_{es}), \tag{4.2.32}$$

where ρ_c is the density at the central plane, κ_c is the opacity in the central plane, κ_K is the Kramer's opacity $\kappa_K = \rho_c H \kappa_0 T_c^{-7/2}$, $\kappa_0 = 5 \times 10^{20}\,\mathrm{m}^5\,\mathrm{kg}^{-2}\,\mathrm{K}^{-7/2}$ and the electron scattering opacity, $\kappa_{es} = 0.04\,\mathrm{m}^2\,\mathrm{kg}^{-1}$. Introducing the above results into energy conservation equation gives

$$\nu\Sigma \left(R \frac{\partial \Omega}{\partial R} \right)^2 = \frac{4\sigma_B T_c^4}{3(\kappa_{ff} + \kappa_{es})\Sigma} + \left(4 - \frac{3}{2}\beta \right) \Sigma v_R \frac{1}{\Sigma R} \left(\frac{dlnT}{dlnR} - \frac{W}{\Sigma} \frac{dln\Sigma}{dlnR} \right), \quad (4.2.33)$$

4.3 The Governing Equations

4.3.1 Differential Equation-I

In this section we derive the equation describing slim accretion disk ignoring the dynamo component magnetic field. If we define a function y related to the viscous stress through

$$y = \nu\Sigma, \quad (4.3.1)$$

we can rewrite Eq. (2.2.28) as

$$y' = \frac{\dot{M}}{6\pi R} - \frac{y}{2R} + \frac{4H}{\Omega} \left(\frac{B_R B_\phi}{\mu_0} \right) \quad (4.3.2)$$

On the other hand Eq. (4.2.20), can be rewritten as

$$B_{\phi,shear} = \frac{3B_R}{\alpha_{ss}} \left(\frac{3}{2}\beta_K - \left(\frac{R}{R_c} \right)^{3/2} \right) ., \quad (4.3.3)$$

and R_c is the corotation radius at which the disc angular velocity equals the stellar angular velocity. It is defined by

$$R_c = \left(\frac{GM}{\Omega_s^2}\right)^{1/3} = 1.5\times 10^6 M_1 P_{spin}^{2/3} m \tag{4.3.4}$$

where P_{spin} is the spin period and $M_1 = \frac{M}{M_\odot}$.

Substituting Eq. (4.3.3) in to Eq. (4.2.24), ignoring the dynamo contribution in this treatment gives

$$B_R B_\phi = \frac{3B_R^2}{\alpha_{ss}}\left(\frac{3}{2}\beta_K - \left(\frac{R}{R_c}\right)^{3/2}\right), \tag{4.3.5}$$

This (Eq. (4.3.5)) when inserted in to Eq. (4.3.2) delivers

$$y' = \frac{\dot{M}}{6\pi R} - \frac{y}{2R} + \frac{12HB_R^2}{\alpha_{ss}\mu_0\Omega_K}\left(\frac{3}{2}\beta_K - \left(\frac{R}{R_c}\right)^{3/2}\right). \tag{4.3.6}$$

Further introducing the necessary relations we can re write Eq. (4.3.6) as

$$y' = \frac{\dot{M}}{6\pi R} - \frac{y}{2R} + \frac{12\mu_q^2}{\alpha_{ss}\mu_0\sqrt{GM}}\left(\frac{3}{2} - \frac{1}{\beta_K}\left(\frac{R}{R_c}\right)^{3/2}\right)HR^{-13/2}. \tag{4.3.7}$$

If we introduce a dimensionless variable Λ through $y = \Lambda\dot{M}$, and another dimensionless radial coordinate r through $R = rR_M$, where R_M is the Magnetospheric radius, the ODEs Eq. (4.3.7) take the form

$$\frac{d\Lambda}{dr} = \frac{1}{6\pi r} - \frac{\Lambda}{2r} + \mu_q^2 \alpha_{ss} \mu_0 \sqrt{GM\dot{M}} R_M^{-11/2} r^{-13/2} \left(\frac{3}{2} - \frac{\omega_s}{\beta_K} r^{3/2} \right), \tag{4.3.8}$$

where ω_s is the fastness parameter defined by

$$\omega_s = \left(\frac{R_{in}}{R_{co}} \right)^{3/2} = 0.87 \dot{M}_{13}^{-3/11} M_1^{-5/11} \mu_{q20}^{6/11} P_{spin}^{-1}, \tag{4.3.9}$$

and

$$R_M = \left(\frac{2\pi^2 \mu_q^2}{GM\dot{M}^2 \mu_0^2} \right)^{1/11} = 1.86 \times 10^5 \dot{M}_{13}^{-2/11} M_1^{-1/11} \mu_{q20}^{4/11}. \tag{4.3.10}$$

We can now rewrite the ODEs, Eq. (4.3.8) in final form as

$$\frac{d\Lambda}{dr} = \frac{1}{6\pi r} - \frac{\Lambda}{2r} + C_2 r^{-13/2} \left(\frac{3}{2} - \frac{\omega_s}{\beta_K} r^{3/2} \right), \tag{4.3.11}$$

where $C_1 = 2\varepsilon\mu_q \left(\frac{3\gamma_{dyn}}{\mu_0 \sqrt{GM\dot{M}}} \right)^{1/2} R_{in}^{-9/4}$ and $C_2 = \frac{12\mu_q^2}{\alpha_{ss}\mu_0\sqrt{GM\dot{M}}} R_{in}^{-11/2}$ We can further transform Eq. (4.3.11) by defining the unit less parameter ξ as $r = 1/\xi$, and rewrite as

$$\frac{d\Lambda}{d\xi} = -\frac{1}{6\pi\xi} - \frac{\Lambda}{2\xi} - C_2 \left(\frac{3}{2} - \frac{\omega_s}{\beta_K} \xi^{-3/2} \right) \xi^{9/2}, \tag{4.3.12}$$

where $C_2 = \frac{12\mu_q^2}{\alpha_{ss}\mu_0\sqrt{GM\dot{M}}} R_M^{-11/2}$

4.3.2 Numerical Solution

The density profiles are shown in Figs. (4.1) - (4.3). In general the result shows that density decreases with radius in different fashion at different points. The curves are not smooth and

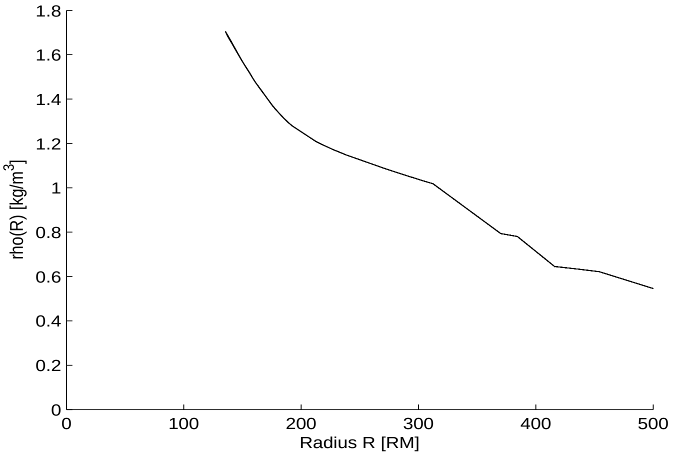

Figure 4.1: The density profile of slim accretion disk around magnetic star - where the stellar magnetic field is $B_0 = 10^4$ T.

abrupt changes are observed at different points. Zigzagish behavior is clearly observed in all cases. The complex behavior observed from the respective plots can be mainly due to the large accretion rate.

The accretion disk temperature profiles are shown in Figs. (4.4) - (4.6). Again the result shows that temperature decreases with radius though the type of decrease is different at different points. The curves still are not smooth and abrupt changes are observed at different points. Here rather successive constancy and linear behavior is clearly observed. The complex behavior observed from the respective plots can be mainly due to the large accretion rate. This can be because of advective behavior of slim disks unlike radiatively efficient Shakura Sunyaev disks.

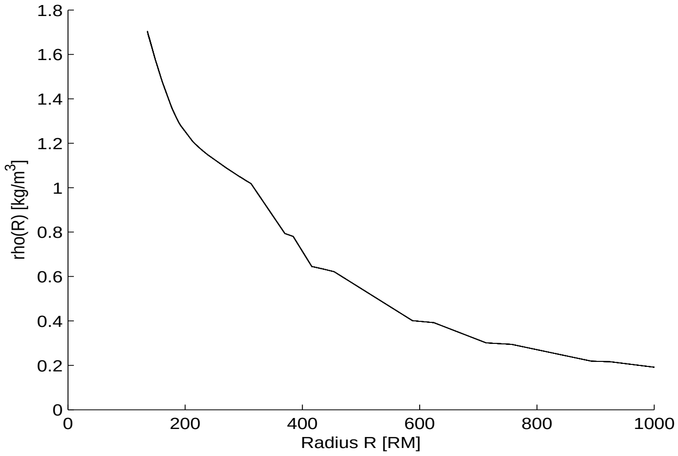

Figure 4.2: The density profile of slim accretion disk around magnetic star - where the stellar magnetic field is $B_0 = 10^4$ T.

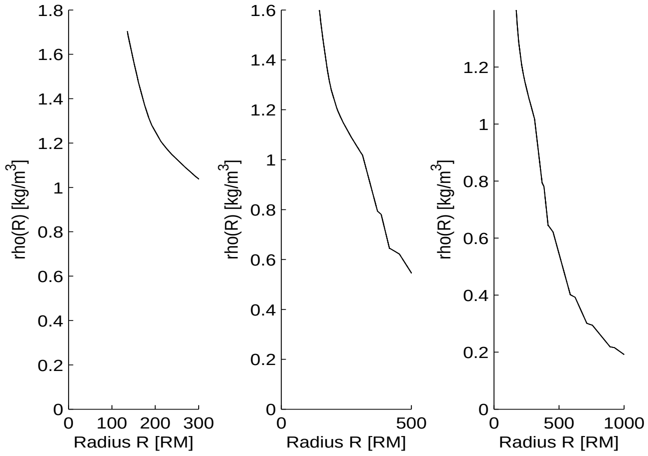

Figure 4.3: Combined plot for the variation of density of slim accretion disk around magnetic star with r - where the stellar magnetic field is $B_0 = 10^4$ T.

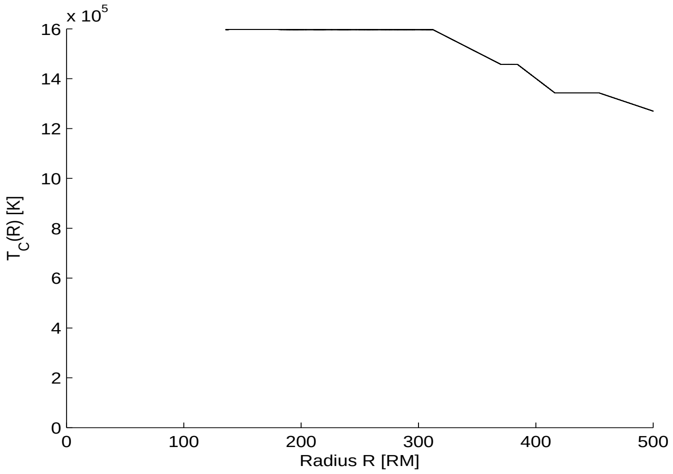

Figure 4.4: The temperature profile of slim accretion disk around magnetic star - where the stellar magnetic field is $B_0 = 10^4$ T.

The accretion disk Lambda profiles are shown in Figs. (4.7) - (4.9). The result shows that Lambda increases with radius smoothly. Here the maximum viscosity occurs at the outer raius of the disk. However, even the maximum vlue here is by far less than that of our previous result. This may show that the disk is non viscous. The complex behavior observed from the respective plots can be mainly due to the large accretion rate and non viscous or advective nature of the disk. This can also confim slim disks are radiatively in-efficient.

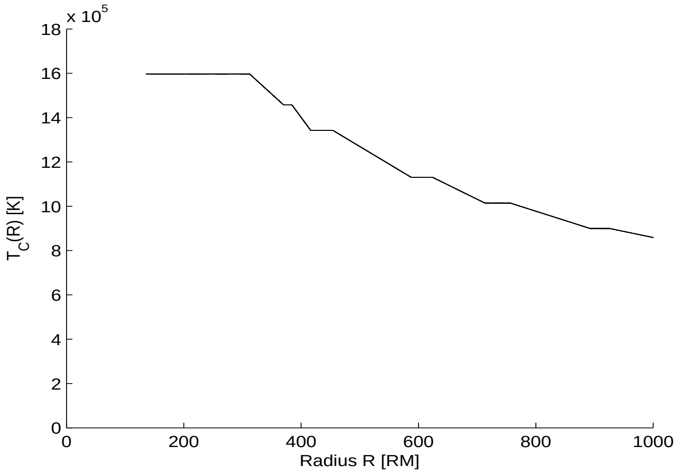

Figure 4.5: The temperature profile of slim accretion disk around magnetic star - where the stellar magnetic field is $B_0 = 10^4$ T.

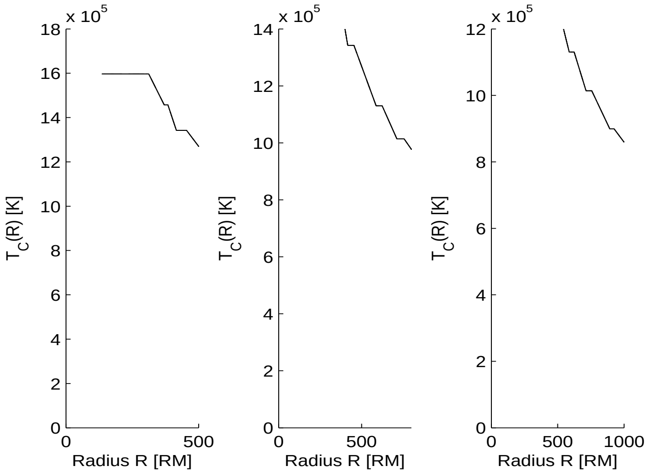

Figure 4.6: Combined plot for the variation of temperature of slim accretion disk around magnetic star with r - where the stellar magnetic field is $B_0 = 10^4$ T.

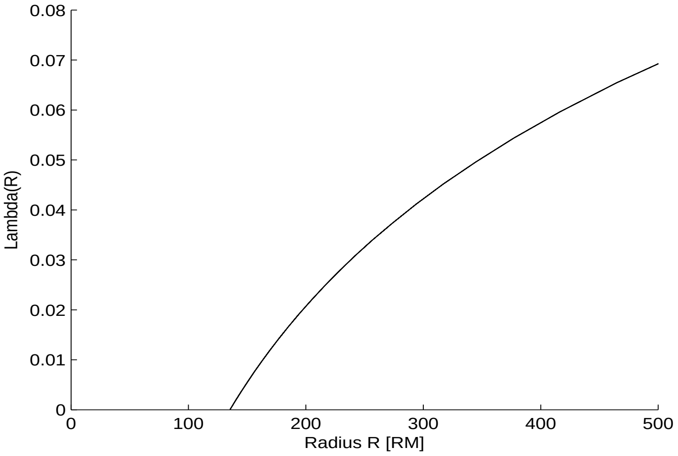

Figure 4.7: The viscosity (Lambda) profile of slim accretion disk around magnetic star - where the stellar magnetic field is $B_0 = 10^4$ T.

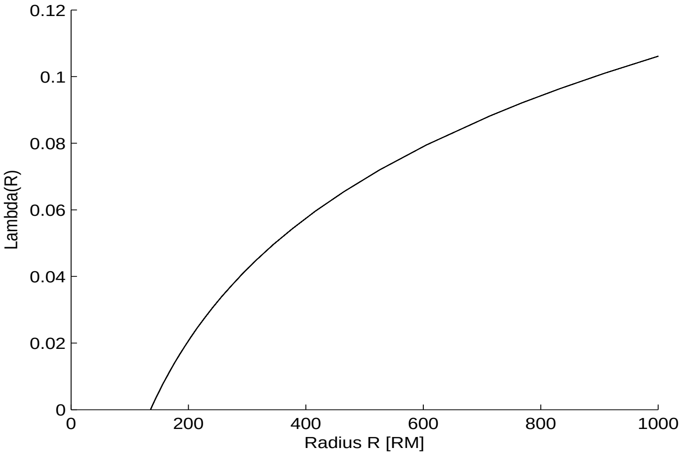

Figure 4.8: The viscosity (Lambda) profile of slim accretion disk around magnetic star - where the stellar magnetic field is $B_0 = 10^4$ T.

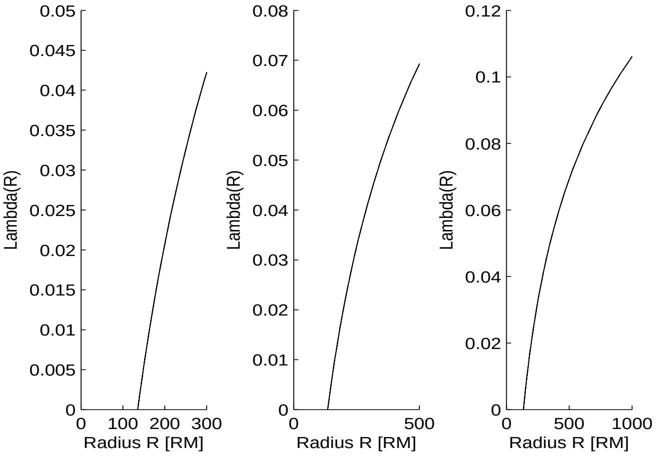

Figure 4.9: Combined plot for the variation of Lambda of slim accretion disk around magnetic star with r - where the stellar magnetic field is $B_0 = 10^4$ T.

4.3.3 The Differential Equations II

The second option is to include the dynamo component. We will solve two differential equations along with coupled equations to study slim disk in this work. Introducing $\ell = R^2\Omega$, and $\dot{M} = 2\pi R v_R \Sigma$ and and defining $y = \nu\Sigma$, we can derive ODE in terms of viscosity function and rewrite Eq. (2.2.28) as

$$y' = \frac{\dot{M}}{6\pi R} - \frac{y}{2R} + \frac{4}{\Omega}\frac{B_R B_\phi}{\mu_0}, \tag{4.3.13}$$

From the energy equation we can solve coupled equation for column density and temperature as

$$\frac{d\Sigma}{dR} + \frac{9\pi\alpha_{ss}\beta_K^2}{2(4-\frac{3}{2}\beta)\dot{M}}\left(\frac{GM}{R}\right)^{1/2}\Sigma^2 = \frac{\Sigma}{R}C_\Sigma, \tag{4.3.14}$$

and

$$\frac{dT_c}{dR}+\frac{c(1-\beta)\pi T_c}{\kappa(4-\frac{3}{2}\beta)\dot{M}}\left(\frac{GM}{R}\right)^{1/2}P^{-1/2}=\frac{T_c}{R}C_T, \tag{4.3.15}$$

The radial equation can be rewritten using the energy relation as

$$\begin{aligned}\frac{\partial}{\partial R}(\Sigma\nu)&=\frac{3}{2R}\Sigma\nu+\frac{R\Sigma\alpha_{ss}}{\Omega_K}(\Omega^2-\Omega_K^2)\\ &+\frac{R\Sigma v_R\alpha_{ss}}{\Omega_K}\frac{v_R}{R^3}\left[C_\Sigma-\frac{9\pi\alpha_{ss}\beta_K^2}{2(4-\frac{3}{2}\beta)\dot{M}}\left(\frac{GM}{R}\right)^{1/2}R\Sigma+1\right],\end{aligned} \tag{4.3.16}$$

Finally the combined radial and azimuthal equation is

$$\frac{\partial\Sigma}{\partial R}=\left[\frac{\Omega_K}{\alpha_{ss}}\left(\frac{\dot{M}}{6\pi R}-\frac{\Sigma\nu}{2R}+\frac{4H}{\Omega}\frac{B_RB_\phi}{\mu_0}\right)\right]-\frac{\Sigma R^2}{v_R^2}(\Omega^2-\Omega_K^2)-\frac{\Sigma}{R}, \tag{4.3.17}$$

Using the relation given by Eq. (2.2.18) into Eq. (4.2.23 gives

$$B_{\phi,dyn}=\varepsilon\left(\frac{1}{2}\mu_0\alpha_{SS}\gamma_{dyn}H\Sigma\Omega_K^2\right)^{1/2}=\varepsilon\left(\mu_0\gamma_{dyn}\left(\frac{\Sigma\nu}{2H}\right)\Omega_K\right)^{1/2}, \tag{4.3.18}$$

Eq. (4.3.3) can be also written in a simplified form as

$$B_{\phi,shear}=B_R\left[\frac{\Omega}{\Omega_K}-\left(\frac{R}{R_{co}}\right)^{3/2}\right], \tag{4.3.19}$$

where R_c is the corotation radius at which the Keplerian angular velocity equals the stellar angular velocity. It is defined by

$$R_{co}=\left(\frac{GM}{\Omega_s^2}\right)^{1/3}=1.5\times10^6M_1P_{spin}^{2/3}m, \tag{4.3.20}$$

Here $T_{spin} = \frac{2\pi}{\Omega_s}$ is the spin period of the star, and $M_1 = \frac{M}{M_\odot}$, where$M_\odot$ is the solar mass. Substituting Eq. (4.3.18) and (2.2.41) into Eq. (4.2.24) gives

$$\begin{aligned} B_R B_\phi &= B_R \Big(B_{\phi,shear} + B_{\phi,dyn} \Big) \\ &= B_R \varepsilon \Big(\mu_0 \gamma_{dyn} \Big(\frac{\Sigma\nu}{2H} \Big) \Big)^{1/2} \Big(\frac{GM}{R^3} \Big)^{1/4} - \frac{B_R^2}{\alpha} \Big(\frac{\Omega - \Omega_{star}}{\Omega_K} \Big), \end{aligned} \tag{4.3.21}$$

Further introducing Eq. (2.2.34) we can write Eq. (4.2.24) again as

$$\begin{aligned} B_R B_\phi = \varepsilon \left(\gamma_{dyn} \mu_0 \mu_q^2 \frac{\Sigma\nu}{2H} \right)^{1/2} (GM)^{1/4} R^{-19/4} \\ - \frac{\mu_q^2}{\alpha} R^{-16/2} \left(\frac{\Omega}{\Omega_K} - \left(\frac{R}{R_{co}} \right)^{3/2} \right), \end{aligned} \tag{4.3.22}$$

Substituting Eq. (4.3.22) into Eq. (4.3.13) we can then write

$$\begin{aligned} y' = \frac{\dot{M}}{6\pi R} - \frac{y}{2R} - \frac{4}{\mu_0 \Omega} \Big(\varepsilon \Big(\gamma_{dyn} \mu_0 \mu_q^2 \frac{\Sigma\nu}{2H} \Big)^{1/2} (GM)^{1/4} R^{-19/4} \\ - \frac{\mu_q^2}{\alpha} R^{-16/2} \Big[\frac{\Omega}{\Omega_K} - \Big(\frac{R}{R_{co}} \Big)^{3/2} \Big] \Big) \end{aligned} \tag{4.3.23}$$

or equivalently

$$\begin{aligned} y' = \frac{\dot{M}}{6\pi R} - \frac{y}{2R} + \frac{4\varepsilon}{\mu_0 \beta_K} \Big(\gamma_{dyn} \mu_0 \mu_q^2 \frac{\Sigma\nu}{2H} \Big)^{1/2} (GM)^{-1/4} R^{-13/4} \\ - \frac{4}{\mu_0 \beta_d} \frac{\mu_q^2}{\alpha \sqrt{GM}} R^{-13/2} \Big[\beta_K - \Big(\frac{R}{R_{co}} \Big)^{3/2} \Big] \end{aligned} \tag{4.3.24}$$

To parametrize our equations we introduce dimensionless variables, Λ and x through, $y = \Lambda \dot{M}$, and a dimensionless radial coordinate through $R = rR_{in}$, where R_{in} is the Magnetospheric radius. We can then write Eq. (4.3.23) and (4.3.24) as

$$\begin{aligned}\frac{d\Lambda}{dR} = \frac{1}{6\pi R} - \frac{\Lambda}{2R} - \frac{4\varepsilon\mu_q}{\beta_K}\left(\frac{\gamma_{dyn}\Lambda}{2\mu_0\dot{M}H}\right)^{1/2}(GM)^{-1/4}R_{in}^{-9/4}r^{-13/4} \\ - \frac{4}{\mu_0\beta_K\alpha}\frac{\mu_q^2}{\sqrt{GM}\dot{M}}R_{in}^{-11/2}r^{-13/2}(\beta_K - \omega_s r^{3/2}),\end{aligned} \tag{4.3.25}$$

or

$$\begin{aligned}\frac{d\Lambda}{dR} = \frac{1}{6\pi R} - \frac{\Lambda}{2R} - \frac{4\varepsilon\mu_q}{\beta_K}\left(\frac{\gamma_{dyn}\Lambda}{2\mu_0\dot{M}H}\right)^{1/2}(GM)^{-1/4}R_{in}^{-9/4}r^{-13/4} \\ - \frac{4}{\mu_0\alpha}\frac{\mu_q^2}{\sqrt{GM}\dot{M}}R_{in}^{-11/2}r^{-13/2}\left(1 - \frac{\omega_s}{\beta_K}r^{3/2}\right),\end{aligned} \tag{4.3.26}$$

where R_{in} is the Magnetospheric/inner radius of an accretion disk given by

$$R_{in} = \left(\frac{2\pi^2\mu^2}{GM\dot{M}^2\mu_0^2}\right)^{1/11} = 5.3 \times 10^5 \dot{M}_{13}^{-2/11} M_1^{-1/11} \mu_{q24}^{4/11}, \tag{4.3.27}$$

and ω_s is the fastness parameter

$$\omega_s = \left(\frac{R_{in}}{R_{co}}\right)^{3/2}, \tag{4.3.28}$$

We can simplify Eq. (4.3.14) for column density as

$$\frac{d\Sigma}{dR} + \frac{9\pi\alpha_{ss}\beta_K^2}{2(4 - \frac{3}{2}\beta)}\left(\frac{GMR_{in}}{\dot{M}^2}\right)R^{-1/2}\Sigma^2 = \Sigma C_\Sigma R^{-1}, \tag{4.3.29}$$

We can rewrite Eq. (4.3.15) for the inner most part assuming maximum radiation

$$\frac{dT_c}{dR} + \frac{c(1-\beta)\pi T_c}{\kappa(4-\frac{3}{2}\beta)} \left(\frac{GMR_{in}}{\dot{M}^2}\right)^{1/2} R^{-1/2} T_c^{1/2} = T_c C_T R^{-1}, \tag{4.3.30}$$

The radial equation, Eq. (4.3.16) can be rewritten similarly as

$$\frac{d\Lambda}{dR} = \frac{3\Lambda}{2R} + \frac{\alpha_{ss} v_K}{2\pi v_R} \sqrt{\frac{r}{R_{in}}} (\beta_K^2 - 1) + \frac{\alpha_{ss}}{2\pi R_{in}} \frac{v_R}{v_K} \left[C_\Sigma - \frac{9\alpha_{ss}\beta_K^2}{2(4-\frac{3}{2}\beta)} \frac{v_K}{v_R} + 1\right], \tag{4.3.31}$$

Finally the combined radial and azimuthal equation is

$$\frac{\partial\Sigma}{\partial R} = \left[\frac{\Omega_K}{\alpha_{ss}} \left(\frac{\dot{M}}{6\pi R} - \frac{\Sigma\nu}{2R} + \frac{4H}{\Omega} \frac{B_R B_\phi}{\mu_0}\right)\right] - \frac{\Sigma R^2}{v_R^2} (\Omega^2 - \Omega_K^2) - \frac{\Sigma}{R}, \tag{4.3.32}$$

The final version of our ODE can be of the form

$$\frac{d\Lambda}{dR} = \frac{1}{6\pi R} - C_1 \Lambda^{1/2} R^{-13/4} - C_2 R^{-13/2} \left(1 - \frac{\omega_s}{\beta_K} R^{3/2}\right) R^{-13/2}, \tag{4.3.33}$$

where

$$C_1 = (25.2)\varepsilon\beta_K^{-1} \gamma_{dyn}^{1/2} \alpha_{SS}^{1/20} \overline{\mu}^{3/16} \dot{M}_{13}^{3/110} M_1^{21/88} \mu_{q24}^{3/16}, \tag{4.3.34}$$

and

$$C_1 = (-0.9)\alpha_{SS}^{-1}, \tag{4.3.35}$$

We can further transform our equations through unit less variable ξ as $r = 1/\xi$. Eq. (4.3.33) then takes the form

$$\frac{d\Lambda}{d\xi} = -\frac{1}{6\pi\xi} + C_1 \Lambda^{1/2} \xi^{5/4} + C_2 \left(1 - \frac{\omega_s}{\beta_K} \xi^{-3/2}\right) \xi^{9/2}, \tag{4.3.36}$$

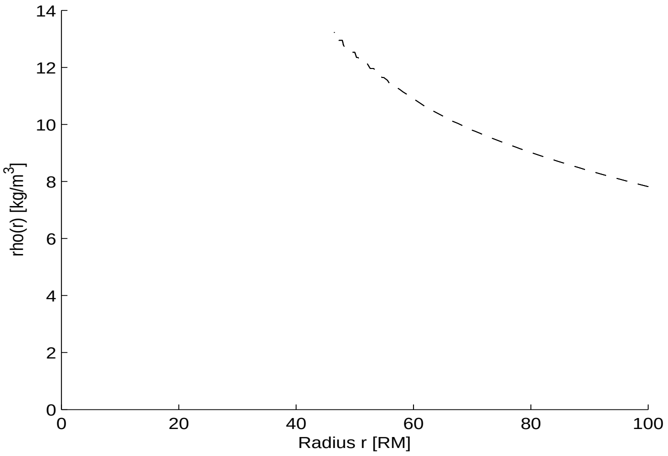

Figure 4.10: The density profile of slim accretion disk around magnetic star - where the stellar magnetic field is $B_0 = 10^4$ T.

4.3.4 Numerical solution

The density profiles when the internal dynamo component is included are shown in Figs. (4.10) - (4.12). In general the results show that density decreases with radius in different fashions at different points. The curves are not smooth and abrupt changes are observed at different points. Comparison with previous section shows direct similarity. Zigzagish behavior is clearly observed here as well in all cases. The complex behavior observed from the respective plots can be mainly due to the large accretion rate.

The accretion disk temperature profile with the inclusion of dynamo component are shown in Figs. (4.13) - (4.15). Again the results show that temperature decreases with radius

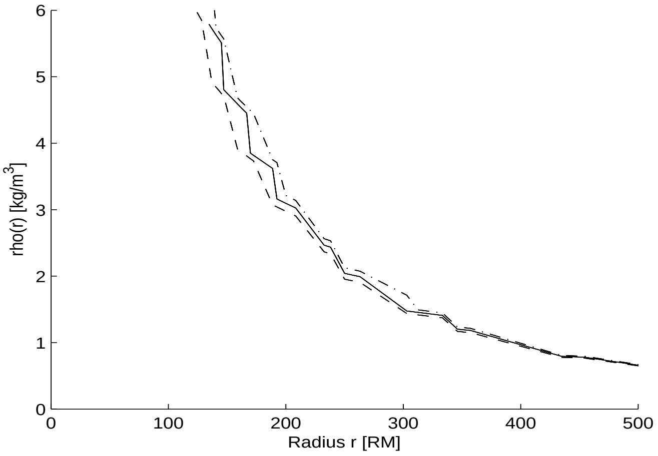

Figure 4.11: The Variation of density of an accretion disk around magnetic star with r, in the outer region where gas pressure and Kramer’s opacity is dominant - where the curves correspond to $\varepsilon = 0.1$,dashed line, to $\varepsilon = 0.05$,the solid line,to $\varepsilon = 0$,the dash dot line.

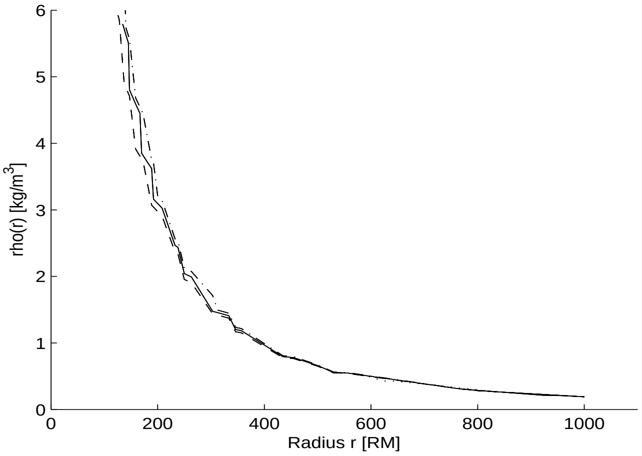

Figure 4.12: The Variation of density of an accretion disk around magnetic star with r, in the outer region where gas pressure and Kramer’s opacity is dominant - where the curves correspond to $\varepsilon = 0.1$,dashed line, to $\varepsilon = 0.05$,the solid line,to $\varepsilon = 0$,the dash dot line.

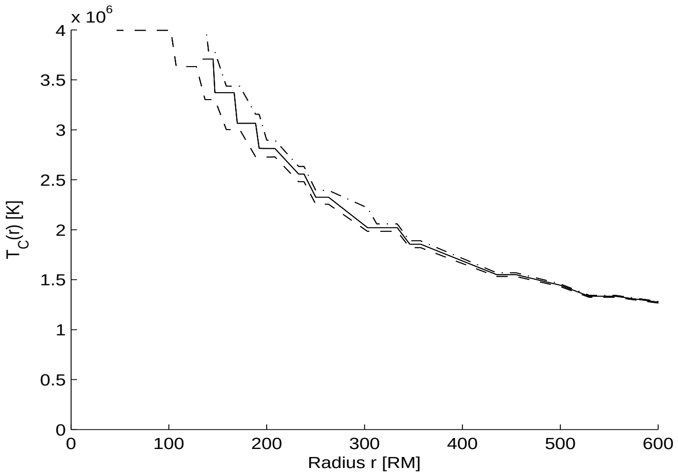

Figure 4.13: The Variation of Central Temperature of an accretion disk around magnetic star with r, where the curves correspond to $\varepsilon = 0$,the dash dot line $\varepsilon = 0.05$,the solid line, and $\varepsilon = 0.1$,dashed line from top to the bottom respectively.

though the type of decrease is different at different points. The curves still are not smooth and abrupt changes are observed at different points. Here rather successive constancy and linear behavior is clearly observed. The complex behavior observed from the respective plots can be mainly due to the large accretion rate. This can be because of advective behavior of slim disks unlike radiatively efficient Shakura Sunyaev disks.

The accretion disk Lambda profiles when dynamo component is included are shown in Figs. (4.16) - (4.18). The results show that Lambda increases with radius smoothly. Here the maximum viscosity occurs at the outer radius of the disk. However, even the maximum value here is by far less than that of our previous result. This may show that the disk is

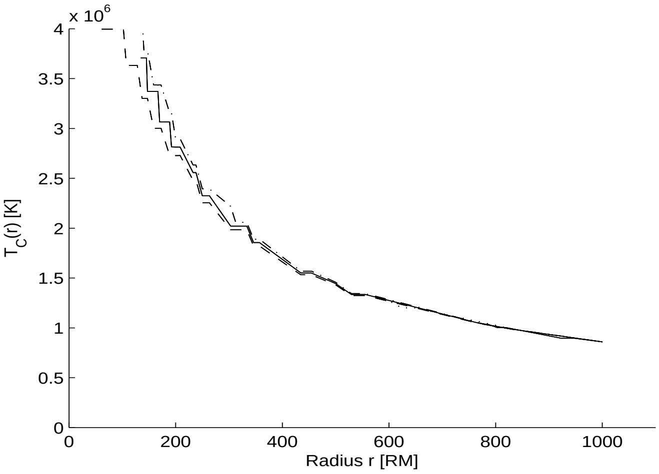

Figure 4.14: The Variation of Central Temperature of an accretion disk around magnetic star with r, where the curves correspond to $\varepsilon = 0$,the dash dot line $\varepsilon = 0.05$,the solid line, and $\varepsilon = 0.1$,dashed line from top to the bottom respectively.

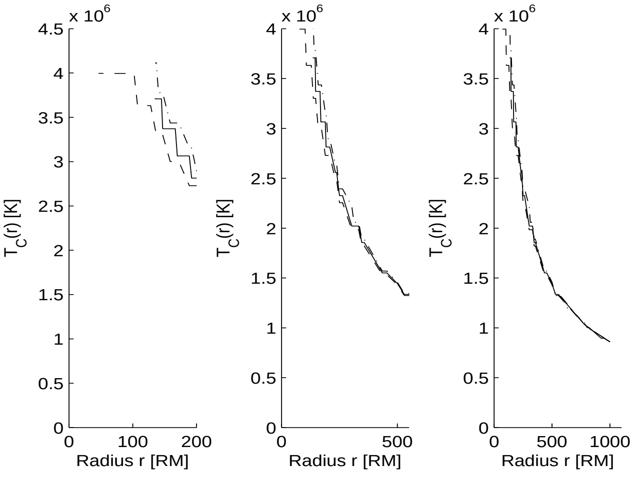

Figure 4.15: The Variation of Central Temperature of an accretion disk around magnetic star with r, where the curves correspond to $\varepsilon = 0$,the dash dot line $\varepsilon = 0.05$,the solid line, and $\varepsilon = 0.1$,dashed line from top to the bottom respectively.

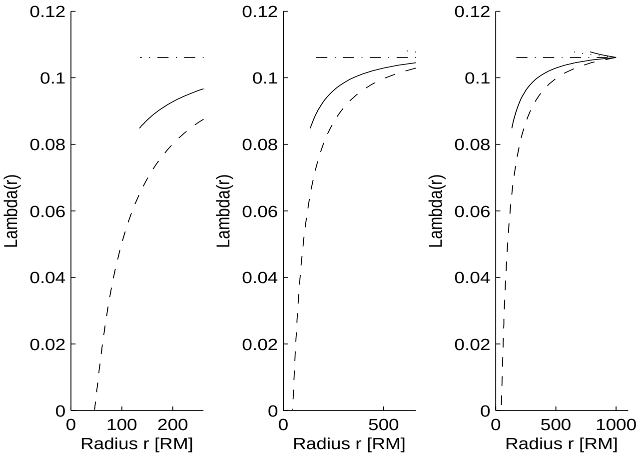

Figure 4.16: The combined plot for Variation of Lambda of an accretion disk around magnetic star with r, where the curves correspond to: $\varepsilon = 0.1$, dashed line, $\varepsilon = 0.05$,the upper solid line, $\varepsilon = 0$,the dash dot line

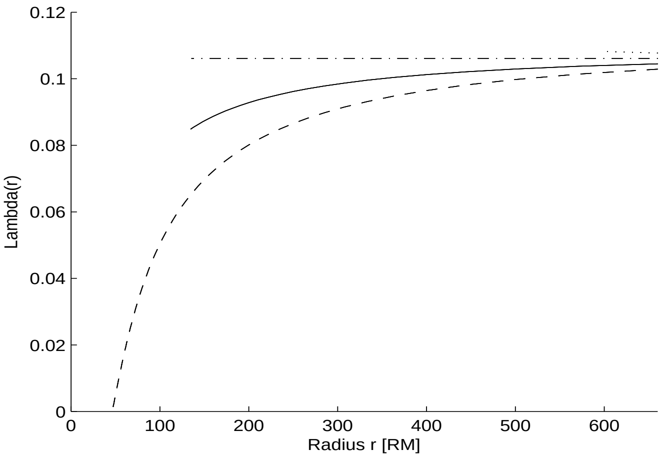

Figure 4.17: The Variation of Lambda of an accretion disk around magnetic star with r,where the top, dashed curve corresponds to $\varepsilon = 0.1, 0.05, and$ 0,the middle, solid curve corresponds to $\varepsilon = 0.05$ and the lower, dashdot curve corresponds to $\varepsilon = 0$,the dotted curve corresponds to $\varepsilon = -0.05$ and the solid curve corresponds to $\varepsilon = -0.1$

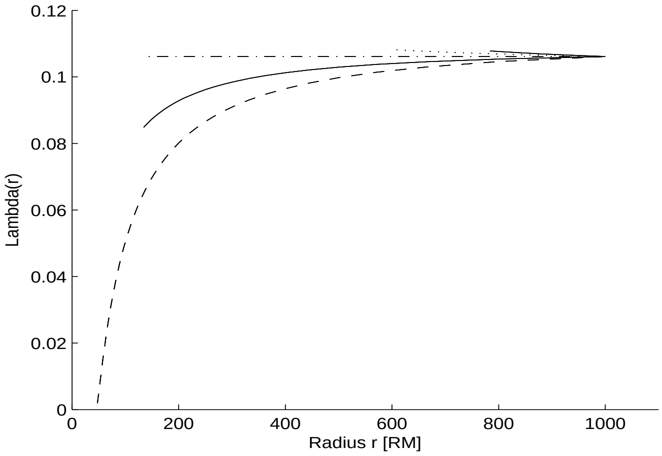

Figure 4.18: The Variation of Lambda of an accretion disk around magnetic star with r,where the top, dashed curve corresponds to $\varepsilon = 0.1, 0.05$, and 0,the middle, solid curve corresponds to $\varepsilon = 0.05$ and the lower, dashdot curve corresponds to $\varepsilon = 0$

non viscous. The complex behavior observed from the respective plots can be mainly due to the large accretion rate and non viscous or advective nature of the disk. This can also confirm slim disks are radiatively in-efficient. The minimum value of Lambda is mainly due to relatively weak magnetic field (10^4 T) applied.

4.4 Coclusions

Slim disks are new branches which are different from standard thin disks. We solved two different cases for this. The first one is including the dynamo component and the second without. In both cases we have obtained plots describing the slim disk solution which are different from our previous results.

The results show variation with radius in different fashions-zigzagish at different points. This complex behavior slim disk may be mainly due to the large accretion rate and non viscous or advective nature of such a disk. This can also confirm slim disks are radiatively in-efficient unlike Shakura Sunyaev disks.

4.5 Summary

We summarize the main results of our study on Keplerian and non-Keplerian-disk as follows:

1. Using alpha prescription we are able to find self-similar disk structure solution for Keplerian and non-Keplerian disk, for different disk regions (local solution).

2. Our numerical solution in section 2.4.3, and 3.4.2 gives the variation of density, temperature and viscosity for Keplerian and non-Keplerian disk around magnetic star.

3. The process of accretion disk formation shows complex and mixed behaviour, that it is super-Keplerian in the inner part and sub-Keplerian in the broader outer part.

4. Quadrupolar accretion also shows that there is funnel flow from accretion disk to the central star.along magnetic field lines. The layer between central star and inner boundary of AD is the region of radiation of thermal and non-thermal origin. - The relatively high

viscosity in the inner part of AD can cause magnetic heating that leads to thermal radiation -The electric field parallel to the open magnetic field lines near the light cylinder accelerates particles out so that there will be non thermal emission from the magnetospheric boundary and inner AD.

5. The density plot , indirectly demonstrates the nature of disk rotation which is Kepler-like, is a direct implication of the possible energy and angular momentum transport.

6. As indicator for the direction of the future work introductory work on slim disk as a new branch is introduced.

Bibliography

[1] Abramowicz M. A., Cheny B., Lasota J. P., and Szuszkiewicz E., *Slim Accretion Disks*, APJ **332** (1988), 646–658.

[2] Abramowicz M. A., Igor V. Igumenshchev, and Jean-Pierre Lasota, *A note on the conditions for SSDADAF transitions*, MNRAS **293** (1998), 443–446.

[3] Potekhin A. Y., *The Physics of neutron stars*, (2011), 1–28.

[4] Harding Alice K., *The neutron star zoo*, Astrophysics Science Division (2013).

[5] Von B., Rekowski and Brandenburg A., *Stellar dynamo driven wind braking versus disc coupling*, AN **327** (2006), 53V.

[6] Warner B., AP & SS **231** (1995), 281G.

[7] Johns-Krull Christopher M., Valenti Jeff, A., and Koresko Christopher, *Measuring the Magnetic Field on the Classical T Tauri Star BP Tauri*, APJ **516** (1999), 900J.

[8] Basri G. and Bertout C., *Accretion disks around T Tauri stars. II - Balmer emission*, APJ **341** (1989), 340B.

[9] Panchenko I. E. and Postnov K. A., *Hercules X-1 pulse profile simulation*, A&A **286** (1994), 497P.

[10] Bouvier J., Alencar S. H. P., and Boutelier T., *Magnetospheric accretion-ejection processes in the classical T Tauri star AA tauri*, A&A **463** (2007), 1017B.

[11] Donati J. F., Howarth I. D., Jardine M. M., Petit P., and Catala C., *The surprising magnetic topology of sco: fossil remnant or dynamo output*, MNRAS **370** (2006), 629–644D.

[12] Hawley J. F., Gammie C. F., and Balbus S. A., APJ **440** (1995), 742.

[13] Bildsten L., Chakrabarty D., and Chiu J., *Observations of Accreting Pulsars*, APJS **113** (1997), 367B.

[14] Jardine M., Collier Cameron, A., Donati J. F., Gregory S. G., and Wood K., *X-ray emission from T Tauri stars*.

[15] Long M., Romanova M. M., and Lovelace R. V. E., *Accretion to stars with non-dipole magnec fields*, MNRAS **374** (2007), 436–444.

[16] Abramowicz M. A. and Fragile P. C., *Foundations of Black Hole Accretion Disk Theory*, APJ **341** (2012), 340M.

[17] Armijo M. M., *Review: Accretion Disk Theory*, APJ (2012), 1–21.

[18] Shakura N. I., Postnov K. A., and Prokhorov M. E., *Presence of a Quadrupole Component of the Magnetic Field Near the Surface of the Neutron Star in HERCULES-X-1*, SvA **17** (1973), 339S.

[19] Ghosh P. and Lamb F. K., *Accretion by rotating magnetic neutron stars. III - Accretion torques and period changes in pulsating X-ray sources*, APJ **234** (1979), 296G.

[20] Cameron P. B., R. E. Rutledge, F. Camilo, Bildsten L., S. M. Ransom, and S. R. , Kulkarni, *Review: Accretion Disk Theory*, APJ **660** (2007), 587–594.

[21] Joss P. C. and Rappaport S. A., *Neutron Stars in Interacting Binary Systems*, ARA&A **22** (1984), 537J.

[22] Safier P. N., *A critique of Current Magnetic-Accretion Models for Classical T Tauri Stars*, APJ **494** (1998), 336S.

[23] Fowler R. H., *Dense matter*, MNRAS **87** (1926), 114.

[24] Lovelace R. V. E., Romanova M. M., and Bisnovatyi-Kogan G. S., *SCREENING OF THE MAGNETIC FIELD OF DISK ACCRETING STARS*, APJ **625** (2005), 957–965.

[25] Balbus S. A. and Hawley J. F., APJ **376** (1991), 214.

[26] ______, Rev. Mod. Phys. **70** (1998), 1.

[27] Tessema Solomon Belay and U. Torkelsson.

[28] ______, *The structure of thin accretion discs around magnetised stars*, A& A **509** (2010), 45T.

[29] Torkelsson U., *Magnetic torques between accretion discs and stars*, MNRAS **298** (1998), L55.

[30] Lipunov V. M., *Magnetospheres of accreting Compact stars Possessing mulipole magnetic fields*, Astron. Zh **55** (1978), 1233–1240.

[31] Jayant V. Narlikar, *Rotation and Accretion Powered Pulsars*, World Scientific Publishing Co. Pte. Ltd., 2007.

[32] Becker W., *Neutron stars and Pulsars*, Springer, 2009.